ELECTRON BEAM MEASUREMENTS OF THE SHOCK WAVE STRUCTURE

PART I

THE INFERENCE OF INTERMOLECULAR POTENTIALS FROM SHOCK STRUCTURE EXPERIMENTS

PART II

THE INFLUENCE OF ACCOMMODATION ON REFLECTING SHOCK WAVES

Thesis by

Eric A. Steinhilper

In Partial Fulfillment of the Requirements

For the Degree of

Doctor of Philosophy

California Institute of Technology

Pasadena, California

1971

(Submitted October 15, 1971)

Acknowledgments

The author wishes to express his appreciation to his advisor, Professor Bradford Sturtevant, for his guidance during the present research and for his suggested improvements to the original manuscript. In addition, the timely advice of Professors Coles, Liepmann, and Roshko is gratefully acknowledged.

Special thanks go to Professor G. A. Bird and to F. W. Vogenitz whose Monte Carlo computer programs for shock structure were modified for different types of intermolecular potentials. B. T. Barcelo is to be thanked for his cooperation and assistance during the joint effort on the shock structure experiments. The author also wishes to thank G. S. Deiwert for the use of his Monte Carlo results prior to publication.

It is a pleasure to thank Mrs. Jacquelyn Beard for typing the manuscript.

The author is indebted to the California Institute of Technology, the National Aeronautics and Space Administration, and the National Science Foundation for their financial assistance. The research in the GALCIT 17-inch shock tube was supported by the National Aeronautics and Space Administration and the Air Force Office of Scientific Research.

ABSTRACT

A technique has been developed in which accurate measurements of shock wave structure and an exact molecular theory of shock waves are used to determine intermolecular potentials. Shock wave density profiles in neon, argon, krypton, and xenon are measured in the GALCIT 17-inch diameter shock tube. The theory is a numerical molecular simulation technique (developed by G. Bird of the University of Sidney) in which the only adjustable parameter is the intermolecular potential. Parameters for the exp-6 and Lennard-Jones potentials are determined by matching the experimental shock wave density profiles with those predicted by the Monte Carlo simulation technique. The experimental data are taken at shock Mach number of about 8; consequently, these results fall in an energy range midway between the molecular beam measurements and low temperature transport property results.

After the potentials for neon, argon, krypton, and xenon have been determined, they are tested for conformity to the Law of Corresponding States. Plots of the potentials in corresponding states coordinates, Φ/kT_{cr} vs. $r/(kT_{cr}/p_{cr})^{1/3}$, show that the exp-6 potential model is superior to the Lennard-Jones. This is an important result, because for the first time this statement can be made on the basis of one set of measurements. Previously it had been necessary to adduce molecular beam results in order to

prove that the inverse twelfth-power repulsive part of the Lennard-Jones potential is too strong. Comparisons show that the exp-6, Lennard-Jones, simple repulsive, and hard sphere molecular potentials predict the experimental shock structure with successively decreasing accuracy. However, their accuracy is sufficient that any one of the potentials would predict any flow accurately enough to give an indication of the relative importance of the parameters governing the flow. This point is emphasized by the need for both the most precise experimental measurements and the use of the Law of Corresponding States in order to provide the basis for ranking the potentials. Moreover, changing the potentials has given a better understanding of the mechanisms by which intermolecular forces influence shock structure.

Measurements of density profiles during the reflection of thick shock waves in argon from the end wall of the GALCIT 17-inch diameter shock tube were reported previously. A mass balance using these profiles had revealed that as much as 20% of the gas which should have been between the end wall and the reflected shock was simply not present. Comparison with theory was not possible because no theory incorporated a loss of mass. Currently available theories for the reflection process include a Monte Carlo flow simulation technique for a thermally accommodating wall.

It is found that this technique can correctly predict either the reflected shock trajectory or the thermal layer near the wall, but the inability to duplicate both implies that there is a second important effect which we assume to be adsorption.

Additional experiments are conducted in neon which has a lower thermal accommodation coefficient than argon. If thermal accommodation is the only wall boundary condition, then according to the Monte Carlo calculations the shock should reflect faster in neon, and the thermal layer should be thinner. However, the measured density profiles show that the reflected shock trajectory is nearly the same as in argon but that there is only half as much "missing" mass. Thus, the neon results provide the most significant confirmation of adsorption.

Because this unexpected violation of the continuity equation was observed, a comprehensive review of instrumental effects and the data reduction technique is made. Several hypothetical effects are shown to have no influence on the loss of mass. However, improving the mass balance calculations accounts for approximately 25% of the missing mass. Correcting for multiple scattering of the electron beam accounts for another 10%, but this correction applies only at the highest densities. Therefore, the "missing" mass of the previous experiment is verified but is reduced somewhat in magnitude.

TABLE OF CONTENTS

TABLE OF CONTENTS (cont.)

TABLE OF CONTENTS (cont.)

LIST OF FIGURES

LIST OF FIGURES (cont.)

LIST OF FIGURES (cont.)

PART I

THE INFERENCE OF INTERMOLECULAR POTENTIALS FROM SHOCK STRUCTURE EXPERIMENTS

I.1 Introduction

I.1.1 The Intermolecular Potential and Bulk Properties

Early work on intermolecular forces led to the general recognition that in the interaction between two noble gas atoms repulsive forces dominate at short range (when the electron clouds overlap) and attractive forces (caused by induced-dipole interactions) dominate at long range. The force between two molecules is related to the potential Φ by $\vec{F} = -\nabla\Phi$. A "harder" potential, one with a stronger repulsive force, has by definition a more negative slope. Similarly, a "softer" potential, while still repulsive, has a less negative slope. One common simplification for the potential is the assumption of spherical symmetry making the potential a function of only the radial distance r . Values for this class of potential have been published (see Table I for potential parameters) but these potentials are unreliable, in some cases varying by nearly an order of magnitude. This disagreement indicates that even for simple cases - the monatomic gases - determining intermolecular potentials is difficult.

Because the potential energy is involved in all molecular interactions, Φ is studied in various fields for many different reasons, usually related to the properties of materials. For example, in atomic physics the potential determines scattering cross sections, and in physics of fluids it influences bulk transport properties. In

determining a potential, the most rigorous theory, exact quantum mechanical calculation, is impractical simply because of the sheer number of calculations required. In atomic physics this difficulty is avoided by use of simplifying assumptions, e.g., Thomas-Fermi-Dirac statistics or hydrogenic atoms. In the physics of fluids the requirements on the accuracy of the potential are even less stringent because fluid mechanics deals with bulk properties - the equation of state and transport properties. Because of the averaging processes inherent in the determination of bulk properties from interaction potentials, accurate values for the potential, such as might be required for some applications in atomic physics are unnecessary. Thus, at least for the present, it would seem to be sufficient to deduce analytical representations of the intermolecular potential which accurately reproduce its actual value over a reasonable range of interatomic separation. In the present work this is done by an inverse method; actual flows are used to infer the intermolecular potential. In order to accomplish this, a flow which is simple to analyze in terms of the potential and simple to measure experimentally is required. The shock structure problem is a suitable flow because it is one dimensional and boundary effects are absent.

It should be noted that it is impossible, even in principle, to explicitly determine exact numerical values

of the intermolecular potential from such experiments because the problem of inverting the integral equations of statistical mechanics which express bulk properties in terms of the intermolecular potential is unsolved. Furthermore, there exists the practical impossibility of conducting experiments over a sufficiently large range of energies to precisely define the potential. The standard procedure is to assume an analytic potential function with one or more adjustable parameters, to predict theoretically some measurable property, and to adjust (fit) the parameters for agreement between theoretical and experimental values. It should be noted that this procedure of inferring the potential is common to most experimental determinations of the potential and assumes that solutions of the statistical mechanical integral equations are unique. Unfortunately, it is not certain that unique solutions do exist. For example, the equation for second virial coefficient

$$B(T) = \frac{-2\pi N}{3kT} \int_0^\infty r^3 \frac{\partial \Phi}{\partial r} e^{-\Phi(r)/kT} \, dr \qquad 1.1\text{-}1$$

is not unique[1]. Perhaps judicious use of a procedure similar to that of Dymond and Alder[2], in which many known properties are incorporated into the fit, reduces the likelihood of finding nonunique solutions.

I.1.2 Previous Methods of Determining Potentials

Previous determinations of the intermolecular potential may be divided into two categories, characterized by the magnitude of the energies of the interacting particles in the experiments. The high energy range was investigated by calculating collision cross sections from the scattering of molecular beams with energies much greater than the thermal energy. The potential was inferred from the cross section data. Amdur[3,4] generated a beam of high velocity neutral particles and directed it through a chamber containing the test gas. Some of the particles were scattered out of the beam by collisions with molecules in the scattering chamber. The intensity of the beam leaving the chamber was measured, and the total collision cross section was calculated from the ratio of the intensities of the initial and scattered beam. Then the cross section data were fitted to those predicted by a simple repulsive potential $\Phi = Kr^{-s}$. Kamnev and Leonas[5] measured total collision cross sections with a similar molecular beam apparatus, and their data were also fitted to a simple repulsive potential. The experimental apparatus of Leonas and Sermyagin[6] was capable of measuring differential collision cross sections. From the differential cross section data, the potential parameters for an exponential repulsive potential $\Phi = Ae^{-\alpha r}$ were determined.

The low energy range has been investigated by measuring transport properties, second virial coefficients, or

crystal data. The results were used to approximate the potential in the region of the potential well. For example, Hirshfelder[7] determined potential parameters for the Lennard-Jones potential from viscosity data and also from second virial coefficient data. Whalley and Schneider[8] measured second virial coefficients in the temperature range 175°K to 975°K. Using an isothermal bath, they allowed a gas to expand repeatedly into an empty vessel and measured the equilibrium pressure each time. The second virial coefficient was found from the p, v, and T data according to the virial equation of state. Then they determined the potential parameters for the Lennard-Jones and exp-6 potentials which produce the best agreement between experimental and theoretical second virial coefficients. Mason and Rice[9] calculated the three exp-6 potential parameters from the lattice constant and the heat of sublimation at 0°K. This was sufficient information to calculate only two parameters; the third one was determined from a simultaneous fit to viscosity and second virial coefficient.

I.1.3 Potential Parameters Obtained from Shock Structure

The parameters for the Lennard-Jones

$$\Phi = 4\epsilon \left[\left(\frac{\sigma_o}{r}\right)^{12} - \left(\frac{\sigma_o}{r}\right)^{6} \right] \qquad 1.1\text{-}2$$

and modified Buckingham* (exp-6)

$$\Phi = \frac{\epsilon}{1 - \frac{6}{\alpha}} \left[\frac{6}{\alpha} e^{\alpha\left(1 - \frac{r}{\sigma_m}\right)} - \left(\frac{\sigma_m}{r}\right)^{6} \right] \qquad 1.1\text{-}3$$

potentials which are determined from the present shock structure measurements apply in an intermediate energy range, previously covered by interpolation between high and low energy regions. The low energy experiments which involve molecular interactions in equilibrium gases (e.g., second virial coefficient measurements) do not normally extend up to the intermediate range because of the difficulty of achieving high oven temperatures. The need for higher temperatures (equivalent to higher collision energies) can be satisfied by use of a pressure driven shock tube as described below.

The nonequilibrium processes which determine shock wave structure are dominated by collisions and, hence, by

---

* σ_o is the radius at which the Lennard-Jones potential $\Phi = 0$, and σ_m is the radius of the minimum of the exp-6 potential. In either case the characteristic radius is hereafter referred to as σ.

the intermolecular potential. In the present work, intermolecular potentials are deduced by use of accurate measurements of shock wave structure together with an exact molecular theory of shock waves. Specifically, the potential parameters are determined by matching the density profile of a shock wave measured by an electron beam densitometer[10] with the profile predicted by a Monte Carlo direct simulation technique[11-15] in which the only free parameter is the intermolecular potential. The present experimental method stems from that of Russell[16], Schultz-Grunow and Frohn[17], and Schmidt[10]. This method gives precise measurements of the density throughout the shock wave. The Monte Carlo method has been used to predict successfully flow past bodies (flat plates, cylinders, and spheres) with heat transfer[18-21] and to predict shock structure in gases with hard-sphere and simple repulsive potentials[11-14, 22].

Because different forms for the potential can in principle predict the same experimental data, an additional criterion is needed to determine which of the analytical forms is the best. The Law of Corresponding States is a suitable criterion since it is valid both for the gases used in the experiments and for the form of the potentials used in the Monte Carlo calculations. In order to perform this test, Schmidt's measurement of shock wave structure

is repeated in neon, krypton, and xenon. (Helium is not used in the shock structure technique because the best results are obtained near a shock Mach number of 8 which is difficult to obtain for gases with a low molecular weight.)

I.2 The Law of Corresponding States

I.2.1 Derivation of the Law of Corresponding States

The Law of Corresponding States, which says that all substances satisfy the same equation of state when expressed in terms of suitably normalized thermodynamic variables, stems from the equation of state proposed by Van der Waals. Pitzer[23], by using a partition function and by making certain assumptions best satisfied by the rare gases, has proved the Law of Corresponding States for materials having a potential of the form:

$$\Phi = \epsilon \; f\left(\frac{r}{r_o}\right) . \qquad 1.2\text{-}1$$

More recently Liepmann[24] using dimensional analysis has argued that for a monatomic real substance the free energy per unit mass must have the form:

$$f = \frac{\epsilon}{m} \psi\left(\frac{vm}{r_o^3} , \frac{kT}{\epsilon}\right). \qquad 1.2\text{-}2$$

By requiring f to include the perfect gas case in which f is only a function of m, he deduced that the correct form must be:

$$f = \frac{\epsilon}{m} \psi\left(\frac{vm}{r_o^3} , \frac{kT}{\epsilon} , \frac{\hbar}{r_o\sqrt{\epsilon m}}\right) . \qquad 1.2\text{-}3$$

Since 1.2-3 is an equation of state (even though it is not in the more usual variables p, v, and T), the noble gases should obey a Law of Corresponding States.

The usefulness of this law is the capability of deducing unmeasured values of properties of one substance from the known values of a second material. On the other hand, if several substances are known to obey the Law of Corresponding States and if some property has been measured experimentally, the degree of conformity to the law indicates the accuracy of the measurement.

The application of the Law of Corresponding States to the shock structure measurements requires a form of the law governing potentials. Classical statistical mechanics provides the link between Liepmann's version, equation 1.2-3, and the same law expressed in terms of the intermolecular potential. For N identical, structureless molecules (again a condition best satisfied by the rare gases) the free energy is:

$$F = Nm\mathcal{f} = - kT \log Z_N =$$

$$- kT \log \left\{ \frac{1}{N!\, h^{3N}} \iint e^{-H(\vec{r}^N, \vec{p}^N)/kT} \, d\vec{r}^N \, d\vec{p}^N \right\} \qquad 1.2\text{-}4$$

where:

$$H\left(\vec{r}^N, \vec{p}^N\right) = \sum_{i=1}^{N} \frac{p_i^2}{2m} + \Phi\left(\vec{r}^N\right) \qquad 1.2\text{-}5$$

is the Hamiltonian and the superscript N on the vectors includes the coordinates of all N molecules. Substituting for $\mathcal{H}$ from equation 1.2-3 and evaluating the momenta integrals yields:

$$\psi\left(\frac{vm}{r_o^3}, \frac{kT}{\epsilon}, \frac{\hbar}{r_o\sqrt{\epsilon m}}\right) = \frac{kT}{N\epsilon} \log\left\{\frac{1}{N!}\left(\frac{kT}{\epsilon}\right)^{\frac{3N}{2}}\left(\frac{r_o\sqrt{\epsilon m}}{\sqrt{2\pi}\,\hbar}\right)^{3N}\int e^{-\Phi(\vec{r}^N)/kT}\, d\left(\frac{\vec{r}^N}{r_o}\right)\right\}. \qquad 1.2\text{-}6$$

Now this equation must hold, whatever the form of Φ. The integration over the spatial coordinates must be a function only of the limits of integration which are expressible in terms of the volume; other variables, e.g., kT/ϵ and $\hbar/r_o\sqrt{\epsilon m}$, are unchanged by this integration. Since the left hand side is a function of three variables, the right hand side of equation 1.2-6 can be at most a function of the same three variables. Therefore, the most general form the potential can have is

$$\Phi = \epsilon f\left(\frac{mv}{r_o^3}, \frac{kT}{\epsilon}, \frac{\hbar}{r_o\sqrt{\epsilon m}}\right) . \qquad 1.2\text{-}7$$

Without assuming a shape for the volume, mv/r_o^3 may be replaced by r^3/r_o^3. Thus, the most general form for a potential which satisfies corresponding states is:

$$\Phi = \epsilon f\left(\frac{r}{r_o}, \frac{kT}{\epsilon}, \frac{\hbar}{r_o\sqrt{\epsilon m}}\right) . \qquad 1.2\text{-}8$$

It cannot be inferred from this derivation that all potentials of the most general form will satisfy corresponding states, nor can it be inferred that only the one true potential will satisfy corresponding states.

I.2.2 Application of the Law of Corresponding States

The use of the Law of Corresponding States provides a way to rate the effectiveness of potentials since they must satisfy the law and predict the experimental measurements. First the parameters of the potential model are adjusted to give the best fit of the experimental data; then the potentials are rated by how well they satisfy the Law of Corresponding States. It is, of course, assumed that the experiments are free of errors. Furthermore, the functional form of f in equation 1.2-8 is assumed to be independent of $\hbar/r_o\sqrt{\epsilon m}$ and kT/ϵ. The assumption that f is independent of $\hbar/r_o\sqrt{\epsilon m}$, in addition to being made explicitly above, is also made implicitly whenever the Monte Carlo method is used because the method is a classical calculation (effectively $\hbar = 0$). The assumption that f is independent of kT/ϵ is made in order to give f the simplest dependence of kT/ϵ.

Curves of

$$\frac{\Phi}{kT_{cr}} = \frac{\epsilon}{kT_{cr}} f\left(\frac{r}{r_{cr}}; \frac{r_{cr}}{r_o}\right) \qquad 1.2\text{-}9$$

vs. r/r_{cr} are plotted for each gas. T_{cr} is the critical temperature, and r_{cr} is the critical radius defined as

$$r_{cr} \equiv \left(kT_{cr}/p_{cr}\right)^{1/3} . \qquad 1.2\text{-}10$$

According to the Law of Corresponding States the curves 1.2-9 for each gas should be identical; if they do not coincide, the potential does not obey the Law of Corresponding States. Thus, the dispersion of curves on the corresponding states plot indicates either that the assumed potential has the improper radial dependence or that the constant r_{cr}/r_o varies from gas to gas thereby contradicting the Law of Corresponding States.

The Law of Corresponding States is one of two ways to rate the suitability of the potential models. Previously[2,8] the best potential was indicated by the minimum scatter between some experimentally measured property and the one predicted from the potential. Checking for conformity to the Law of Corresponding States may not be an improvement over the previous method of rating of the potentials, but a comparison of the rating techniques shows that the use of the law has one significant advantage - it has a unifying effect on the results. Corresponding states says that the monatomic gases are somehow interrelated. On the other hand, the weakness of the earlier technique is a lack of interrelationship. This weakness allows a different potential form to be best for each gas - a conclusion known to be wrong. Moreover, there are weaknesses common to both methods; for example, it is impossible to remove the effects of experimental uncertainty or scatter. In principal, two

equally good potentials might be rated differently because the existence of a larger experimental uncertainty for one of them has been neglected. Thus, any conclusions about the appropriateness of potential forms based on corresponding states should be accepted cautiously.

I.3 Shock Structure Experiment

The shock structure measurements are performed in the GALCIT 17-inch diameter shock tube[25] which is capable of producing a nearly planar shock wave approximately one centimeter thick. Figure 1 is a schematic diagram of the present shock tube configuration. An enlarged view, figure 2, of the electron beam densitometer[10] used for the density measurements shows its location inside the test section. Electrons, forming a beam 12 cm. long and approximately 0.05 cm. in diameter, travel perpendicular to the shock tube centerline from the cone shaped injector needle to the Faraday cage. The cage and needle are attached to a 12 inch diameter "cookie cutter", which isolates the flow from the wall boundary layer. The large diameter insures that the shock wave is planar between the needle and cage.

The experimental procedure is described in detail by Schmidt[10]; recent modifications to his procedure are discussed by Barcelo[22]. The basic procedure, however, is fairly simple. The pressure in the driver section is increased until the diaphragm bursts causing a shock wave to propagate into the test section. The speed of the wave is measured using thin film gauges placed along the side wall of the shock tube. As the shock wave passes between the needle and cage, the increasing density causes more electron-atom collisions which deflect electrons out of the

beam thus decreasing the current reaching the cage. The cage current is recorded as a function of time, and later, density as a function of position is calculated from the exponential attenuation law $\rho \propto \log(I/I_o)$ and a Galilean velocity transformation. The experimental density profiles are tabulated in Table II.

I.4 Monte Carlo Molecular Simulation Method

Shock structure may be predicted by approximate equations with varying degrees of success. For example, according to Liepmann[26] the Navier-Stokes equations inaccurately predict shock structure upstream of the point of maximum stress because the value of the ratio of compressive stress to pressure becomes too large for accurate predictions. Since the absence of a solid boundary in the shock structure problem removes any possible geometric reference length, the mean free path λ is the only reference length. This situation defines a transition region in which the flow may be considered neither free molecular flow nor continuum flow, and in such a case the Boltzmann equation is appropriate. This equation is impossible to solve exactly for flows with highly nonequilibrium regions. The Monte Carlo method developed by G. A. Bird[11-15] simulates the actual physical processes in these flows and thereby produces approximate solutions to the Boltzmann equation.

Consider the Boltzmann equation when only binary collisions occur:

$$\frac{\partial f}{\partial t} + v_i \frac{\partial f}{\partial x_i} + R_i \frac{\partial f}{\partial v_i} = \left(\frac{\partial f}{\partial t}\right)_{coll} = \iint (\tilde{f}\tilde{f}' - ff')\, g\, dQ\, dc' \quad . \tag{1.4-1}$$

Once the distribution function $f = f(x_i, v_i, t)$ is known, all interesting quantities, ρ, p, v, T, and the fluxes at boundaries, can be calculated. The change of the distribution function expressed by the left hand side of equation 1.4-1 is due to local variations, to the flux of molecules across the boundaries of a volume element, and to external forces acting on the molecules. Bird[15] and Vogenitz[21] have stated that in the absence of collisions the left hand side of the Boltzmann equation may be satisfied by simply following the molecules as they move in phase space. Similarly the right hand side may be represented by the proper collision calculations. Bird's Monte Carlo technique[11-15] computes collisions by statistical sampling in a way that assures the correct loss term for each region of velocity space[15] and obeys the dynamics of binary collisions. Thus, by accurately simulating the Boltzmann equation, the Monte Carlo method predicts flow properties (or f) with an accuracy limited only by statistical sampling.

In the application of the technique two simplifying approximations are made. First, the movement of molecules and their collisions are uncoupled. The calculation proceeds in increments of Δt, a time small compared to the mean collision time τ, to large flow time by alternately moving the molecules and then "computing" an appropriate number of collisions. Second, when these collision

calculations are made, the flow field is divided into cells of increment Δx . The width Δx is chosen to be so small that the flow properties in a cell are nearly constant; consequently, any two molecules in a cell may be considered as possible collision partners irrespective of distance between them. These two approximations may be made arbitrarily accurate by decreasing the size of Δx and Δt . Both Bird[15] and Vogenitz[21] have reported that if the parameters $\frac{\Delta t}{\tau} \lesssim \frac{1}{M_\infty}$ and $\frac{\Delta x}{\lambda} \lesssim \frac{1}{2}$ a further decrease in Δx or Δt does not noticeably change the flow.

As a consequence of simulating the movements of only a fraction of the actual molecules, essentially no collisions would normally occur between the representative molecules. The necessity of forcing collisions to occur in order to reduce the large effective mean free path λ (and hence τ) in the simulated flow requires the neglect of the particle's location in the cell during the collision calculation. What amounts to a much larger density of particles is forced by generating an azimuthal angle and an impact parameter randomly; the actual stored molecular velocities, however, are used for the precollision velocities.

The proper number of collisions and hence the appropriate relations for mean velocity, mean free path, and mean collision time result if the correct collision frequency is simulated. Whenever a collision takes place, a time counter for the cell is incremented by:

$$\Delta t = \frac{1}{n\ A\ V_r} \left(\frac{2}{N_c}\right) \qquad 1.4\text{-}2$$

where n is the number density, A is the collision cross section, V_r is the relative velocity, and N_c is the number of molecules in the cell. Bird[15] has shown that calculating collisions until the time counter for each cell is greater than the current flow time, $\sum\Delta t$, insures the correct collision frequency when the sample size and number of collisions is large.

For the collision calculation itself, pairs of molecules are selected randomly from a cell and are either rejected or accepted for a collision with a probability proportional to their collision cross section, which depends upon their relative velocity and potential model. If they are accepted, the conservation of energy and angular momentum are used to determine the deflection angle and postcollision velocities, which are then stored for subsequent use.

For some flow geometries, e.g., a one dimensional flow, it is possible to omit one or more of the spatial coordinates from the calculation. In a two dimensional case the velocity component normal to the plane containing the molecules is retained for use in the collision calculations. This velocity component is not used in the movement calculations - the molecules are kept in their original plane.

I.4.1 Boundary Conditions

The boundary conditions used for the Monte Carlo calculation are those which would produce the desired physical flow. For the shock structure problem the flow is generated by the one dimensional piston problem.[27] A specularly reflecting boundary moves at the velocity of the fluid behind a normal shock wave of a preselected Mach number. As the calculation proceeds from some initial condition, it is observed that a shock wave forms and propagates away from the piston at a relative speed $u_s - u_p$. Bird[11] found that after a time t_s the shock wave has developed and that it subsequently propagates without changing its structure. Furthermore, Bird found that the duration, t_s, of the starting process is the time taken by an ideal shock to move about eight mean free paths ahead of the piston. The boundary conditions for the piston problem are equally applicable in shock fixed coordinates or in laboratory coordinates.

I.4.1a The Coordinate Systems

The x-t diagram for the piston problem formulated in laboratory coordinates[11] (the "unsteady" case) is shown in figure 3. The boundary conditions are that the two walls reflect molecules specularly. Initially molecules are in a stationary flow field. During the calculation one wall remains fixed; the other, the piston, is started at time $t = 0$. No assumption of equilibrium is needed anywhere in

the flow field. It should be noted that the assumption of a steady state sampling region does not change the calculation itself (neither the movement nor the collisions).

The x-t diagram for the shock fixed coordinates (Bird's "steady" state case[12]) is shown in figure 4. Initially the molecules are in a flow with a mean velocity $-u_s$. The piston starts at $t = 0$ and moves with velocity $u_p - u_s$. The upstream boundary is the edge of the sampling region; it remains stationary in shock fixed coordinates. The downstream boundary, a piston which reflects molecules specularly, moves discontinuously relative to the upstream boundary. Both boundary conditions depend on the additional assumption that equilibrium conditions exist at the right and left edges of the flow field. Molecules having a Maxwell-Boltzmann velocity distribution about the mean velocity, $-u_s$, are inserted in the flow at the upstream edge at a rate given by the mass flux. Downstream molecules are removed at the proper rate by instantaneously moving the piston upstream a distance $(u_s - u_p)\,\Delta t$ at the beginning of each time interval Δt and deleting all molecules remaining downstream of the piston. This always produces the correct rate of removal because the piston may be placed anywhere in an equilibrium flow without affecting the flow.

I.4.1b Comparison of Monte Carlo Technique in the Two Coordinate Systems

A comparison of the two versions of the boundary conditions shows some similarities. In both systems there is a starting process, an assumption that a steady shock wave develops, and an assumption that successive samples of the instantaneous flow properties are independent. This latter assumption is a crucial part of either method and, of course, has been verified[15]. Moreover, Bird noted that it seemed to make little difference "whether this (the flow property) is obtained from, for example, 100 samples with an average of 10 molecules per cell or 10 samples with 100 molecules per cell."[15]

The more significant part of the comparison is the differences in the boundary conditions used in the two coordinate systems: 1) the location of the boundaries and 2) the assumption of equilibrium at the edge of the "steady" state region containing the shock wave. Presumably, Bird[11,12] verified that these differences are unimportant. Nevertheless, according to the present results, the flow at the edges of the sampling region for both cases is indistinguishable from equilibrium conditions, and thus, the differences in the boundary conditions are probably inconsequential.

Another matter - efficiency - must be discussed because of its deceptive nature. Both methods may be made equally

efficient by eliminating additional starting processes. In the laboratory coordinate case, the calculation may be restarted at any time, for example at time t_s, using the positions and velocities for all molecules at that time. Using a different sequence of random numbers, the statistical sampling of the collision calculation of course produces different postcollision velocities, different movement, and therefore, slightly different flow properties in each cell at the end of the first and hence all subsequent uncoupling intervals. This meets the requirement that in order to combine two distribution functions and thus obtain a better approximation, the second distribution function must be uncorrelative to the original one.

I.4.2 The Potential

Conservation of energy requires that during a collision between two molecules the sum of their kinetic energy and potential energy remains constant. Thus, an expression for the potential energy is a prerequisite for a collision calculation. Furthermore, the conservation relations can be used to relate such things as collision cross section and collision frequency to the potential. Since the Monte Carlo collision calculation is supposed to simulate actual collisions as accurately as possible, the model for the intermolecular potential 1) determines the deflection angle, χ , 2) governs the probability that two molecules collide, and 3) is used to produce the correct collision rate, ν .

Hirshfelder[7] gives an analysis of binary collisions in center of mass coordinates which applies for a general intermolecular potential $\Phi(r)$:

$$\chi = \pi - 2b \int_{r_m}^{\infty} \frac{1}{r^2} \frac{1}{\sqrt{1 - \frac{b^2}{r^2} - \frac{\Phi(r)}{\frac{1}{2}\mu g^2}}} dr \quad . \qquad 1.4\text{-}3$$

Here g is the relative velocity of the collision partners; b , the impact parameter, is distance of closest approach in the absence of the potential; r_m , the largest root of $\sqrt{1 - \frac{b^2}{r^2} - \Phi(r)/\frac{1}{2}\mu g^2} = 0$, is the actual distance of closest approach; and χ is the deflection angle.

Let

$$r^* = \frac{r}{b} \qquad 1.4\text{-}3a$$

and

$$\Phi = \epsilon \; f\left(\frac{r}{\sigma}\right) = \epsilon \; f(r^*) \quad . \qquad 1.4\text{-}3b$$

The parameters describing the collision are also normalized

$$\frac{1}{2}\frac{\mu g^2}{\epsilon} = g^{*2} = \frac{T^*}{2}\frac{g^2}{c_m^{\,2}} \; , \qquad 1.4\text{-}3c$$

$$b^* = \frac{b}{\sigma} \; , \qquad 1.4\text{-}3d$$

and

$$r_m^* = \frac{r_m}{\sigma} \quad . \qquad 1.4\text{-}3e$$

Substituting 1.4-3a through 1.4-3e in equation 1.4-3 yields a formula for the deflection angle:

$$\chi\left(g^{*2},\, b^*;\, \Phi(r^*)\right) =$$

$$\pi - 2b^* \int_{r_m^*}^{\infty} \frac{1}{r^{*2}} \frac{1}{\sqrt{1 - \frac{b^{*2}}{r^{*2}} - \frac{f(r^*)}{g^{*2}}}}\, dr \quad . \qquad 1.4\text{-}4$$

Values of $\chi\,(g^{*2},\, b^*)$ are tabulated for the Lennard-Jones[7] and exp-6[28] potentials.

The probability of two molecules colliding is proportional to gQ where Q is the total collision cross section. In classical mechanics Q for a general

potential is infinite and hence must be truncated in order to be useful.

$$Q = \int_0^{2\pi} \int_0^{b_{max}} b \, db \, d\epsilon = 2\pi \int_0^{b_{max}} b \, db \qquad 1.4\text{-}5$$

Frequently, this integral is expressed in terms of χ since χ as well as Q depends on the impact parameter b. Whichever form for Q is used, the Monte Carlo calculations should be independent of the choice of cutoff value b_{max} in the equation for Q. On physical grounds collisions with a deflection angle smaller than about 10^o may be neglected[29] because they do not contribute to transport properties. Haviland[29], Bird, and others take advantage of the dependence of both Q and χ on impact parameter by truncating Q with an impact parameter large enough to include all deflection angles greater than about 10^o, $|\chi| \gtrsim 10^o$. Now, increasing b_{max}, i.e., Q, does not add collisions large enough to affect the flow, and thus the requirement on the choice of cutoff value for Q is satisfied.

Once $\chi(g^{*2}, b^*)$ and $g\,Q(b^*_{max})$ are determinable, the Monte Carlo collision calculation is reduced to applying the physics contained in the conservation equations. Only the postcollision velocities need be retained. All intermediate results may be discarded. For example, χ, r_m, and even the precollision velocities are never needed again.

I.4.2a Normalization of Potential Parameters

In order to make a given Monte Carlo calculation valid for as many different cases as possible, the parameters used to normalize movement and collision calculations should be related. The movement calculations are conveniently normalized by the most probable speed, c_m, and the mean free path, λ, which are both set equal to 1.0 for equilibrium conditions. A relationship between σ, the characteristic length of the potential, and λ can be obtained using the Chapman-Enskog solution[7] of the Boltzmann equation. This solution applies near equilibrium so that σ is related to the equilibrium mean free path λ_1. The Chapman-Enskog solution gives a relationship between σ and the viscosity μ in terms of a collision integral, $\Omega^{(2,2)*}$, which is defined while obtaining the solution:

$$\mu = \frac{5}{16} \frac{\sqrt{\pi\ mkT}}{\pi\ \sigma^2\ \Omega^{(2,2)*}} \quad . \qquad 1.4\text{-}6$$

In addition

$$\lambda_1 = \frac{1}{\sqrt{2}\ An_1} = \frac{16}{5}\sqrt{\frac{\gamma}{2\pi}}\ \frac{\mu_1}{\rho_1 a_1} \quad . \qquad 1.4\text{-}7$$

Substituting for viscosity yields

$$\sigma^2 = \frac{\sqrt{\gamma mkT_1}}{\sqrt{2}\ \pi a_1 \rho_1 \lambda_1\ \Omega^{(2,2)*}} = \frac{1}{\sqrt{2}\ \pi n_1 \lambda_1\ \Omega^{(2,2)*}} \quad , \qquad 1.4\text{-}8$$

the relationship between σ and λ_1.

The other adjustable parameter in the potential, ϵ, is determined by matching experimental and Monte Carlo density profiles. In the special case of the exp-6 potential, the third parameter, α, is chosen as the same constant ($\alpha = 13.5$) for all gases in order to satisfy the Law of Corresponding States.

I.4.2b Implementation of the Monte Carlo Method

This section describes how the physics are incorporated efficiently into the actual computer program. The computer spends much more of its time on the collision calculations than it spends on the movement calculations. Thus, the efficiency of the Monte Carlo method is optimized by 1) minimizing the number of collision calculations and 2) simplifying an individual collision calculation.

The number of collisions is minimized by eliminating nonessential collisions, for example, those with $|\chi| < \chi_{min}$. Curves of constant χ for the collision parameters g^{*2} and b^* are shown on figure 5. On this figure it is obvious that nonessential collisions could be eliminated by picking the proper cutoff parameter $b^*_{max} = b^*_{max}(g^{*2})$, cf. equation 1.4-5. This is accomplished by devising a transformation to a new impact parameter W such that the transformation eliminates many small angle collisions without the necessity of first calculating χ.

For the Lennard-Jones and exp-6 potentials the choice of

$$W \equiv (g^{*2}/2D)^{1/D}\, b^{*2} \qquad 1.4\text{-}9$$

is prompted by the transformation used in the simple repulsive case[7]. The difference between this and the transformation used for a simple repulsive potential is that D is arbitrary.

Naturally the arbitrariness of D affects the collisions (through both χ and gQ), but a judicious choice of D minimizes the number of collision calculations without affecting the flow properties. The value of D is chosen so that at any expected g^{*2} all W's such that

$$W \leq W_{max} = (g^{*2}/2D)^{1/D}\, b^{*}{}_{max}^{2} \qquad 1.4\text{-}10$$

include all collision angles, χ, with absolute value greater than $\chi_{min} \sim 10^{o}$. Figure 6 shows curves of constant χ for g^{*2} and the transformed impact parameter W with $D = 3.20$ which is suitable for shock structure calculations. The range of g^{*2}, used for selecting D, is estimated from the flow the Monte Carlo technique will calculate.

The calculation of χ by numerical integration as each collision occurs is inefficient. According to

equation 1.4-4

$$\chi = \chi\ (g^{*2},\ b^*) = \chi\ (g^{*2},\ W) \qquad 1.4\text{-}11$$

where g^{*2} is known once the collision pair has been selected and where W is generated randomly and uniformly in the interval between 0 and W_{max}. In order to improve the efficiency, χ is calculated for the expected ranges of g^{*2} and W and then is approximated by a two dimensional polynomial. The method of bicubic splines[30] is chosen because it is more accurate than a two dimensional least squares polynomial. Bicubic splines have the additional advantage that they are continuous and have continuous first and second derivatives. However, the continuity conditions on the deflection angle are relaxed at the singularity, $\chi = -\infty$. The D-transformation changes the singularity from the curved line shown on figure 5 to the nearly straight line shown on figure 6, and hence for the spline fit the singularity is idealized as a straight line and is given a finite value.

I.4.2c Radius of Closest Approach Histograms

Keeping histograms of some collision parameters will reveal things about the potential. The most useful parameter is the radius of closest approach defined in section I.4.2. According to equation 1.4-1, r_m determines which

parts of the potential influence the collision and therefore over which range of separations the potential is in effect measured.

The radius of closest approach is a nonessential part of the Monte Carlo calculation. The use of bicubic splines eliminates the need to calculate r_m^* for each collision. Nevertheless, a spline fit is made for r_m^* just as for the deflection angle. During the steady state part of the calculation a histogram of r_m^* is made for each cell. As each collision is calculated, the minimum separation, $r_m^* = r_m^*(g^{*2}, W)$, between the collision partners is computed from the spline fit, and the occurrence of the value of r_m^* is indicated in the appropriate range on the histogram.

I.5 Determination of Potential Parameters

The experiments give density profiles through shock waves propagating in the monatomic gases neon, argon, krypton, and xenon. Independently, the Monte Carlo method calculates the density profiles for monatomic real gases with different normalized intermolecular potential well depths $T^* = kT/\epsilon$. The experimental and theoretical profiles are compared. The T^* for each gas is determined when the Monte Carlo profile matches the experimental one.

The statistical nature of the Monte Carlo method causes two problems because the matching procedure must resolve differences of the order of the statistical scatter. First, no way is known to remove the expected statistical scatter and thus find the true density. Second, scatter in the shock wave location

$$x_o = X_o/\lambda_1 \quad , \tag{1.5-1}$$

defined as the location where the normalized density

$$\tilde{\rho} \equiv \frac{\rho - \rho_2}{\rho_2 - \rho_1} = \frac{1}{2} \quad , \tag{1.5-2}$$

results from the starting process (see figure 3). This scatter in location is significant when comparing Monte Carlo results, and hence the x axis must be shifted as well as

the density profile smoothed. In either of the two coordinate systems used for the Monte Carlo calculation an arbitrary number of molecules may be in the sampling region at any instant because molecules are free to cross the boundaries. The origin, $x = 0$, in the center of the shock wave is relocated for each profile so that equal amounts of mass are in a region of specified size bounded on each side by nearly equilibrium flow conditions. The new origin is taken to be such that the average of the individual shifts along the x axis equals 0; the densities in this new shifted coordinate system are computed from the original data by linear interpolation. The largest deviation found in x_o is the same order as that estimated by

$$\Delta x = \left(1 / \left(\frac{\Delta \tilde{\rho}}{\Delta x} \right)_{max} \right) \Delta \tilde{\rho} \qquad 1.5\text{-}3$$

where $\Delta \tilde{\rho}$ is taken as the square root of the sample size. Estimating scatter as the square root of the sample size is the usual convention because, though the correct value is unknown, it is known to vary inversely with the square root of sample size (see section I.6.4).

The next step is to smooth the density curves. The procedure is shown graphically in figure 7. Plots of shock wave density profiles with different T^* show thinner shock waves for higher T^* (shallower potential wells). The same effect is observed for both the Lennard-Jones and exp-6

potential, but the change in thickness is less noticeable in the latter case. The method of least squares is used for each cell, location x_i, to smooth the density with respect to the T*'s of several Monte Carlo calculations:

$$\tilde{\rho}\ (T^*,\ x_i) = A_i\ T^* + B_i \qquad 1.5\text{-}4$$

In figure 7 the Monte Carlo densities for four T*'s are indicated by a different symbol for each cell, and the nearly horizontal line indicates the smoothed density for that cell. If T* did not affect shock thickness, random scatter in density would produce random signs for the A_i's as happens far upstream and downstream in the nearly equilibrium flow regimes. Since the standard deviation for the fit in equation 1.5-4, $\sum_\rho = 0.025$, is less than the statistical scatter in density estimated as $\sum_{cy} = (N_{cy})^{-\frac{1}{2}} = 0.032$, where $N_{cy} \simeq 1000$ is the size of the sample at each T*, it is concluded that the fitting procedure yields a significant result.

Inspection of figure 7 suggests that the error in determining T* from the experimental $\tilde{\rho}$'s is smaller in the region of the profiles where the magnitude of the slope, A_i, is large. Hence, the fit is made using densities from the region $\frac{1}{2} \leq |\ x\ | \leq 2$. After the fitting procedure has been completed, a r.m.s. deviation

for the T*'s is computed. However, the experimental profiles, just like the Monte Carlo profiles, have no absolute coordinate. Previously, the Monte Carlo profiles were shifted to make them consistent with each other; now, the experimental profile is shifted to match the Monte Carlo profiles. The proper shift is determined by minimizing the r.m.s. deviation in T*. Figure 8 shows an experimental curve and two smoothed profiles from the Monte Carlo calculation.

From T_1, the temperature of the experimental data; μ, the viscosity at T_1; M, the molecular weight; and T*, the values for σ and ϵ are calculated according to

$$\epsilon = \frac{kT_1}{T^*} \qquad 1.5\text{-}5$$

and

$$\sigma = \frac{266.93\ MT_1 \times 10^{-7}}{\mu\ \Omega^{(2,2)^*}_{(T^*)}} \ . \qquad 1.5\text{-}6$$

In summary, the procedure used for determining T* and σ from the shock wave experiments is as follows:

1) the Monte Carlo profiles are shifted relative to each other so that they have a common origin,

2) the Monte Carlo profiles are smoothed, and

3) the experimental results are shifted relative to the Monte Carlo results until the T* (calculated from experimental densities according to equation 1.5-4) has a minimum amount of scatter.

The potential parameters determined from shock structure are tabulated in Table I along with those determined from other data. Table III gives ϵ/kT_{cr} , r_o/r_{cr} , and $\hbar/\sigma\sqrt{\epsilon m}$. Both ϵ/kT_{cr} and r_o/r_{cr} should be constant according to the Law of Corresponding States. The third parameter, $\hbar/\sigma\sqrt{\epsilon m}$, was assumed to be zero.

I.6 Discussion

I.6.1 Corresponding States Plots of Shock Structure Results

After the potential parameters have been determined, they are tested for conformity to the Law of Corresponding States. According to the results of section I.2.2 the potentials for the noble gases should coincide when plotted as ϕ/kT_{cr} vs. r/r_{cr}. Graphs of the potential plotted in this normalized form are called corresponding states plots. If for different gases the curves for some particular model of the potential do not coincide on these plots, then the lack of coincidence must be caused by the failure not of the gases, nor of the potential, but of the gases as characterized by this potential model to satisfy corresponding states. Thus, the separation of the curves provides a simple way to evaluate the effectiveness of a potential in the sense of corresponding states theory. The disagreement between the potentials of any two gases can be caused by one of three errors in potential form: 1) the assumption that the potential is independent of $\hbar/\sigma\sqrt{\epsilon m}$; 2) the assumption that the potential is independent of kT_{cr}/ϵ; or 3) the improper assumed radial dependence of the potential, $f(r/\sigma)$. The first two assumptions are made in the analysis of binary collisions for the Monte Carlo technique and cannot be easily changed. Thus, failure to satisfy corresponding states indicates an incorrect radial dependence for the potential.

The corresponding states plot for the exp-6 potential with $\alpha = 13.5$ is shown in figure 9. The possibility that for a different α the curves might fall closer together was not explored in the present work. The corresponding states plot for the Lennard-Jones potential is shown in figure 10. Figures 11a and 11b are the same as figures 9 and 10 except for the error bars which indicate values of the potential which would result from a change of plus or minus one standard deviation in T^*. The standard deviation in T^* is obtained from the fit between the smoothed Monte Carlo profiles and the experimental profile and naturally would be increased if the effects of the statistical scatter in the Monte Carlo results, or the experimental scatter in density were included. Comparison of figures 11a and 11b shows that the four curves of the exp-6 case more nearly coincide than the curves of the Lennard-Jones case. This means that the exp-6 potential more nearly satisfies the Law of Corresponding States. A comparison of the error bars on these figures shows that the error bars on the exp-6 curves are shorter than the ones on the Lennard-Jones case. This means that for the exp-6 potential the scatter in T^* is smaller, the result of better agreement between the Monte Carlo and experimental density profiles. Thus, there are two reasons, better conformity to corresponding states and better agreement

with the actual shock structure, for preferring the exp-6 to the Lennard-Jones potential.

The distinguishing feature of the present work is that for the first time this conclusion, which is in agreement with the findings of other authors[31-33], is based on a single set of data. Previously, without the use of corresponding states theory, it has been necessary to compare results from more than one laboratory. For example, a comparison (cf. figures 10, 12, and 13) between the Lennard-Jones potential, determined from shock wave structure and extrapolated to high energies, and molecular beam results[4,5] shows that both the Lennard-Jones potential and its slope are greater than the molecular beam results would suggest, but a similar comparison (cf. figures 9, 12, and 13) using our exp-6 potential shows good agreement.

I.6.2 Limitations on Determining Potentials from Shock Structure

The shock structure method of determining intermolecular potentials has three weaknesses similar to those encountered in the low temperature results[7-9]. First and most important is that the technique seems to be insensitive to the potential. Insensitive means that a significant change in the potential, such as large changes in Φ in the repulsive region or as elimination of the potential well altogether, produces only a small change in the predicted shock structure. It is observed when using the method that even a small error band in the experimental shock structure produces large uncertainty in the potential; for example, the error bars on the krypton curve in figure 11a are caused by a scatter (10% in T^*) which is less than the difference between the Monte Carlo profiles in figure 8. Because of the insensitivity, the intermolecular potentials determined in the present work are considered to be of sufficient validity only for application to engineering problems, i.e., Monte Carlo flow calculations, and not for fundamental atomic properties.

The second weakness of the shock structure method and a weakness that seems to be common to all results[2-9] is the narrow energy range of the experimental data. Ideally, if the data are not at a single particular energy, resulting

in a single point on a corresponding states plot, then the data should cover all energies, but this is a practical impossibility.

The third and least important weakness is the possibility of nonuniqueness - more than one potential may be able to reproduce, say, the viscosity data. This problem could not be eliminated even with the most precise data and the best fitting techniques. Presently, it is felt that the insensitivity to the potentials dominates the results, giving Φ's with large scatter. Nevertheless, the possibility of nonuniqueness has significant implications about experimentally determined potentials. If, indeed, the methods used to determine intermolecular potentials did not produce a unique result, then a potential determined from, say, viscosity data might very well be useless for calculating some other property such as second virial coefficient. This might explain the large scatter in the potentials determined by various authors (see also section I.6.3 and figure 24). In fact, those[33,34,7] who tested their potentials by predicting other bulk properties noticed agreement among the various transport properties but disagreement between second virial coefficients and transport properties. The exception, of course, is Dymond and Alder[2] who required such agreement as a criterion for determining a numerical potential.

I.6.3 Comparisons of Corresponding States Plots

I.6.3a Comparisons with Other Results

In this section the potentials determined by shock structure are compared with those obtained by other experimenters. Only the exp-6 potential is considered. The Lennard-Jones case is less interesting because it neither satisfies corresponding states as well nor predicts shock structure as accurately.

The potentials inferred from molecular beams are valid at higher energies and smaller intermolecular separations than the shock structure results, but nevertheless, the two different sets of results agree moderately well. Kamnev and Leonas[5] obtained the potentials shown in figure 12. The poor agreement between their molecular beam results and potentials obtained from shock structure is probably related to the failure of the molecular beam results to satisfy corresponding states.

Figure 13 shows the potentials obtained by Amdur and Mason[4]. Their potentials satisfy corresponding states and agree with the shock structure potential better than the potentials of Kamnev and Leonas[5]. On figure 13 the neon curves nearly coincide; for xenon the potentials agree well, but their slopes do not. Figure 14 shows the shock structure results compared with those of references 4 and 5. Only for neon do the potentials agree; the xenon results are in serious disagreement. The significance of the

disagreement between the two different beam studies is that because both authors fit total collision cross sections to a simple repulsive potential, the disagreement must be between the experimentally measured cross sections.

Another molecular beam result - that of Leonas and Sermyagin[6] - is shown in figure 15. These curves have been derived from the fit of an exponential repulsive potential to differential cross sections. Interestingly, the argon, krypton, and xenon potentials are in accordance with corresponding states. On the other hand the neon curve agrees remarkably well with the other beam results for neon (and with the extrapolated shock structure potential). Together, however, these two observations cannot be reconciled with the Law of Corresponding States given by equation 1.2-9.

Amdur and Mason[34] have used low temperature crystal data in addition to their own molecular beam data in order to calculate the three parameters α , ϵ , and σ for the exp-6 potential. Their curves are shown in figure 16. The dispersion of their curves for the different gases indicates poor agreement with the Law of Corresponding States. This is caused partly by their molecular beam data; compare figures 13 and 16. Their determination of the potential is important because it is valid for a large range of energies including that covered by the shock structure measurements.

The comparison with the exp-6 shock structure curves shows good agreement at the high energies. Near the large radius limit of the potentials obtained from shock structure, the curves for these potentials start to depart from the band established by the curves of Amdur and Mason. Since crystal data were used to determine the potential of Amdur and Mason, thereby making their results valid near the potential minimum, the disagreement near the ends of the shock structure curves is not surprising.

Second virial coefficient data are used to determine the potentials calculated by Whalley and Schneider[8] and plotted in figure 17. Notice the disagreement between curves for two different potentials using the same data (krypton). Whalley and Schneider found no significant difference in the standard deviation between their experimental data and the second virial coefficients predicted by either the Lennard-Jones or exp-6 potentials. It is, of course, possible that this was a result of nonuniqueness, but it is more likely that the accuracy was limited either by the insensitivity of their method or by the experimental uncertainty. A comparison of the exp-6 curves from shock structure with those obtained by Whalley and Schneider shows agreement, but again, as with the results of Amdur and Mason, the shock structure curves are slightly higher at large separations. This seems to indicate that shock

structure cannot accurately determine the shape of the potential well or equivalently that the details of the potential well have little effect on shock structure.

Some Lennard-Jones potentials which were determined by Hirshfelder, Curtiss, and Bird[7] from viscosity data are shown in figure 18. With the exception of krypton there is remarkable conformity to the Law of Corresponding States. The agreement with the potentials obtained from shock structure is very good. This is not really surprising; it is known[33] that the Lennard-Jones or exp-6 potentials can reproduce accurately either transport coefficients or second virial coefficients but not both, and hence, agreement between potentials determined from viscosity and shock waves, which are transport property phenomena, is expected.

Dymond and Alder[2] have calculated a numerical potential for argon which satisfactorily predicts second virial coefficients, thermal diffusion factors, thermal conductivity, and viscosity. Their potential is compared with the one obtained from shock structure in figure 19. The potentials agree well at small intermolecular separations but disagree at large separations. Dymond and Alder have reported that their potential "has a smaller attractive tail, a wider bowl with a steeper outer wall, and a weaker repulsive regions than previously postulated potentials."[2] In addition to the repulsive region being weaker and the bowl being wider,

$\Phi(r) = 0$ at a lower radius than any of the results discussed above (compare figures 19 and 24). Dymond and Alder did not explain why the range of their potential continues far beyond the mean thermal energy of the highest temperature data used in their fit.

Figure 20 is included for completeness. It is the simple repulsive potential determined by Barcelo[22] using the same shock structure measurements but a more heuristic method for analyzing the data than used in the present work. The simple repulsive potential could not satisfy corresponding states because s is different for different gases. The functional form, i.e., s , must be identical if this potential is to satisfy corresponding states. The effect can be seen on figure 20. Because of the change in s the curves are not parallel, they would not coincide even if they were displaced laterally. However, in spite of its inability to satisfy corresponding states theory, the simple repulsive potential does reproduce shock structure accurately.

In addition to the individual plots already discussed, the potentials have been grouped together according to potential model. Figure 21 shows the exp-6 potentials; figure 22 shows the Lennard-Jones potentials; and figure 23 shows the simple repulsive potentials. Although the dispersion of the curves on each of these three plots is about the same, the conclusion that therefore all three potential

forms are equally good is an improper conclusion because figures 21 - 23 show results from different kinds of data. For example, figure 21 shows potentials based on molecular beam data and solid properties[34] but not on viscosity data; on the other hand, figure 21 shows potentials based on viscosity data[7] but not on molecular beam data. In order to draw a meaningful conclusion, the determination of the potentials should be alike - the same data and the same techniques should be used.

I.6.3b Scatter on Corresponding States Plots

The most striking characteristic of the corresponding states plots, figures 11 through 23 and also figure 47, is the disagreement among the potentials. This disagreement is illustrated in figure 24 by superimposing nine of the plots. The most likely explanation for the large scatter is, of course, the insensitive methods used to deduce the potential from the data. Some other possible explanations are: 1) incorrect critical constants, 2) poor measurements, 3) inadequate potential forms, and 4) nonuniqueness. Because the different kinds of data do not result in the potentials for different gases showing a trend on the corresponding states plots, the inaccuracies in the critical constants are evidently less important than the other causes of scatter. The scatter due to inadequate potential forms and nonuniqueness must somehow be related to the problem

of inverting the statistical mechanical integral equations. Since all techniques have this problem, it is reasonable to assume that these two causes of scatter result in some minimum band of uncertainty for the potential on the corresponding states plot. An estimate of this bandwidth might be taken as the scatter among the Lennard-Jones potentials determined from shock structure. Hence, any scatter larger than this bandwidth is likely to be caused by poor measurements or insensitive methods.

I.6.4 Accuracy of the Monte Carlo Method

Statistical scatter of a sampling process is inversely proportional to the square root of sample size. In the Monte Carlo method the flow variables, i.e., density, are calculated by counting molecules and by forming averages of suitable products of the molecular velocities. Because of the finite number of particles the value for these properties is scattered about the true value. A good approximation to the observed scatter in the normalized density is obtained by equating the r.m.s. deviation to the inverse square root of N_s, where N_s is the product of the average number of molecules in an upstream cell at any instant and the total number of sampling intervals in the Monte Carlo calculation at a single T^*. On an IBM 360/75 an $N_s \simeq 4000$ (involving about 300,000 collisions) can be obtained in about 11 minutes. Because the densities from calculations at four different T^*'s are used to determine the smoothed profiles, the estimated accuracy of these profiles (two are shown in figure 8) is about $(4 \times 4000)^{-\frac{1}{2}} \simeq 0.8\%$ (cf. the r.m.s. deviation of the fitting procedure for T^* is 10% of T^*).

I.6.5 Histograms from the Monte Carlo Calculations

The values of the potential which are most important in determining shock structure are found from histograms of the relative collision velocity and the minimum intermolecular separation occurring during a collision. It is assumed that the distribution of g^{*2} and r_m^* is continuous, and the histograms are smoothed in a manner which does not change the area under the curve in each interval. In addition, the histograms for cells in the nearly equilibrium regions upstream and downstream of the shock wave are combined in order to reduce scatter.

Histograms for g^{*2} in upstream and downstream regions are shown in figure 25 and compared with Maxwell-Boltzmann distributions of relative velocity in the equilibrium regions. These two quantities are not the same; hence, the curves will not in general coincide. The g^{*2} histograms are used for two purposes. First, they show that the range of g^{*2} used in the spline fit includes all g^{*2} actually occurring during the Monte Carlo calculation. Second, the g^{*2} histograms are used to help explain the more important radius of closest approach histograms. Figure 25 shows that the high velocity tail terminates at a lower g^{*2} for the upstream distribution than for the downstream one. It is thought that a few high energy (velocity) molecules from behind the shock wave travel several mean free paths upstream without hitting another molecule. The initial

collision of these "penetrating" molecules with a typical upstream molecule would be a collision with a large g^{*2} and would account for the long tail on the upstream distribution of g^{*2}.

The histogram for radius of closest approach, figure 26, shows a well defined maximum for representative upstream and downstream regions. The sharp peaks occur because so many collisions had this distance of closest approach. Apparently, the range of intermolecular separation over which the potentials determined from shock structure are valid is actually rather limited. In the cells located between $x/\lambda_1 = -3.5$ and $x/\lambda_1 = 2.5$ the most probable distance of closest approach occurred at separations which lie between the maxima on figure 26, as indicated by the thick line. According to equation 1.4-4 the potential near $\Phi(r_m^*)$ is important in characterizing the collision. Hence, the range of separation spanned by the thick line is assumed to be that at which the potential has been measured, and this criterion determines the range of the potential indicated in figure 9.

In addition to the well defined maximum, the upstream histogram in figure 26 also shows a small relative maximum at $r^* \simeq 1.5$ and a plateau at small distances of closest approach. It is thought that the small relative maximum is caused by orbiting. Figure 27 shows the reduced

effective potential $\Phi_e^* = \Phi^* - g^{*2}b^{*2}/r^{*2}$ for a low value of $(g^* b^*)^2$. Orbiting occurs when the relative collision velocity is such that an approaching molecule has exactly the energy required to reach r_2^* with zero radial velocity; during the infinite time the molecule takes to reach r_2^*, it spirals around the center many times apparently orbiting. In a collision with a slightly lower initial velocity, the molecule spends a great deal of time near r_2^*. With a slightly higher initial velocity, the molecule continues inward to r_1^*. Hence, at these relatively low collision energies the possible distances of closest approach for collisions are $r_m^* < r_1^*$ or $r_m^* > r_2^*$. Now, if the independent variable of a histogram has an interval in which the probability is zero and if the interval is bounded by regions in which the probability is finite, the histogram appears to have a bimodal distribution. Because r_1^* and r_2^* are functions of collision energy and because the discontinuity in r_m^* occurs only at the lowest energies, the bimodal distribution for r_m^* tends to be obscured even at low energies. At high $(g^* b^*)^2$ orbiting cannot occur (no relative maximum of $\Phi_e^*(r^*)$ exists), and hence r_m^* is continuous.

On the upstream side of the shock wave the r_m^* histograms have a plateau at separations smaller than the most probable distance of closest approach. This plateau,

which, incidentally, does not appear on similar histograms constructed from Monte Carlo calculations made with a Lennard-Jones potential, reveals that molecules penetrate further into the core of the exp-6 potential than they do for a Lennard-Jones potential. It is thought that the plateau is caused by a combination of two effects, the high velocity collisions indicated by the tail on the velocity histogram, figure 26, and the relative weakness of the repulsive forces for the exp-6 potential. Comparing figures 9 and 10 shows that the low energy collisions which predominate upstream have a larger distance of closest approach during a head-on collision for the exp-6 than for the Lennard-Jones potential. This shifts the maximum on the histogram towards larger radii. On the other hand, the high energy collisions on the tail of the distribution penetrate to smaller separations during a head-on collision for the exp-6 than for the Lennard-Jones potential. This shifts the probabilities near the low radii cutoff towards lower radii. Thus, the two modifications to the histogram combine to form the plateau.

I.7 Conclusions

The purpose of the present and previous investigations of shock wave structure is to develop an understanding of rarefied flows. The advantages of studying shock waves as a prototypical rarefied flow are that it is one dimensional and there are no solid boundaries in the flow field. These two simplifications are desirable because they reduce the number of parameters which must be specified in both experiment and theory.

The application of corresponding states theory is a more exacting test of the capability of a proposed potential to simulate the true one than the previous test of comparing bulk properties. Comparisons of the potentials obtained from shock structure are made in corresponding states coordinates. Figure 11 and 20 show that the exp-6 is superior to the Lennard-Jones potential model and that the Lennard-Jones is superior to the simple repulsive model. This is an important result because for the first time this statement can be made on the basis of one set of measurements. Previously it was necessary to adduce molecular beam results to show that the repulsive twelfth power dependence of the Lennard-Jones potential is too strong and hence the exp-6 is better. Similarly, it was necessary to cite either liquid properties or negative second virial coefficients to prove that the simple repulsive potential needs an attractive term and hence, e.g., that the Lennard-Jones is better.

Thus, finding that the exp-6, Lennard-Jones, simple repulsive, and hard sphere intermolecular potentials predict the experimental shock structure with successively decreasing accuracy is an important result of shock structure measurements.

The accuracy of the shock structure predicted by the Monte Carlo method is even more important than the capability of ranking the potentials. Any one of the above potentials used in the Monte Carlo calculations predicts the flow so accurately that both the most precise experimental measurements and corresponding states theory are required in order to be able to rank the potentials. The consequence of the accurate predictions is that shock structure can, indeed, be used to determine the potential, and although the method turns out to be rather insensitive to the potential, it appears to be as good as any other method based on bulk properties. Moreover, changing the potentials has supplemented the understanding of rarefied flows by giving insight into the mechanisms by which the potential influences the shock structure.

Finally, a conclusion, which applies equally to all rarefied flows, is that the shock structure method is an ineffective way to determine the shape of the potential well (i.e., the attractive forces) because at room temperature and higher a great majority of the intermolecular collisions in a gas depend on the positive portion of the potential.

PART II

THE INFLUENCE OF ACCOMMODATION ON REFLECTING SHOCK WAVES

II.1 Introduction

Difficulty in specifying gas-surface boundary conditions was one of the reasons for the early importance of experimental studies of shock structure. Now, with the shock structure problem solved (see Part I), the precise boundary conditions for rarefied gas dynamic flows about bodies emerge as the most important remaining problem. These boundary conditions comprise at least two interrelated effects - heat transfer and momentum transfer. In some applications these may be incorporated without specifically considering the gas-surface interaction, i.e., by simply specifying an adiabatic wall or allowing for a nonzero heat transfer rate and by requiring that the velocity of the fluid near the wall equals the velocity of the wall. In other cases it might be necessary to specify empirically these quantities based on experimental evidence. However, only recently the introduction of the Monte Carlo method to the study of rarefied gas flows[20,21] has removed the requirement that simple boundary conditions be used in order to make equations solvable. At the present time, the possibility of incorporating a detailed specification of the gas-surface interaction serves to emphasize the lack of understanding in this area.

This field is not new (for many years gas-surface interactions have been studied as they affect thermal accommodation[35-37]), but application of the Monte Carlo

technique is. A gas molecule incident on a solid surface is said to be thermally accommodated if it attains thermal equilibrium with the solid before being reflected. Most previous experimental investigations, because of the nature of the technique used, have involved the ideal case of a clean surface (no absorbed layers) in order to get reproducible results. However, it might be argued that the ultimate reason for studying accommodation is not to get results for an ideal wall but to understand how it affects "dirty" surfaces. With this knowledge, it might be possible, for example, to control accommodation in order to obtain efficient heat transfer at gas-solid interfaces. One of the most important features of the present work is that it seems to be the first case in which measurable effects due to adsorption processes have been observed in a gasdynamic environment at such high densities that the surfaces are unavoidably "dirty", i.e., in an "engineering" environment.

To anyone familiar with kinetic theory it is clear that thermal accommodation implies that momentum accommodation must also occur. On the other hand, until recently there has been little serious consideration of mass accommodation, in spite of the generally accepted fact that the presence of an absorbed layer of gas affects the thermal accommodation coefficient. Clearly, the process of formation of adsorbed layers must be studied by time dependent experiments;

one way to study adsorption is to suddenly change the incident flux to the wall, $\frac{1}{4} \rho \bar{c}$, and to observe the change of mass in the layer. Because a shock wave is the fastest possible change in the variables of state, it is the best way to increase the mass flux to the wall.

Piva and Sturtevant[38] have reported adsorption observed in a transient experiment. They measured density near a wall during the reflection of a shock wave, and their measurements had sufficient resolution that the behavior of incident shock, the dense thermal layer near the wall, and the accelerating reflected shock could be studied. From the continuity equation and their data they calculated a mass balance. They found that mass had "disappeared" from the region behind the reflected shock and concluded that it must have been adsorbed onto the wall. The adsorption is rapid, most of it taking place in a few mean collision times (see figure 28).

The twofold purpose of the present work is first to verify that the previous measurements[38] were correct and second to learn what parameters affect the adsorption. The most important verification of adsorption is the observation that by changing the test gas from argon to neon the amount of missing gas is reduced. This result is supplmented by a careful review of instrumental effects and data reduction techniques, but no errors large enough to account for the

missing mass are discovered. In addition, the experimental density profiles are compared with profiles predicted by a Monte Carlo calculation for a shock wave reflecting from a thermally accommodating, nonadsorbing wall. The disagreement between the experimental and Monte Carlo profiles indicates that the boundary condition used in the calculation is inadequate because the other possibility - an experimental error - has been checked and eliminated.

Repeating Piva's experiment in neon gives density profiles which have the same general characteristics as the profiles in argon but which result in approximately half the amount of missing mass. The reduction in missing mass occurs because in the neon case the thermal layer is slightly denser and the reflected shock location is slightly farther away from the wall. These two effects are not compatible with a change in only thermal accommodation, and hence, they may be used to show the need for a second boundary condition.

It can be argued qualitatively (or demonstrated quantitatively by Monte Carlo calculation in which accommodation and adsorption can be varied independently) that the effect of a decrease of thermal accommodation (with no change of adsorption) on the shock reflection process is to decrease the density of the wall thermal layer and thereby to displace the reflected shock farther from the wall. On the other hand, a decrease of adsorption (with no change of accommodation) tends to increase the density near the wall

and also to cause the reflected shock to be farther from the wall. Thus, the respective gasdynamic effects of accommodation and adsorption are opposite; of course, it is impossible under present circumstances to predict which effect will dominate in any specific physical situation.

However, the above qualitative understanding proves to be sufficient to demonstrate that the present experimental observations are adsorption-dominated. In the neon case both the higher gas density near the wall and the displacement of the shock slightly farther from the wall necessarily means that in neon there is more gas between the wall and the reflected shock; the only source for such an increase in these experiments is the adsorbed layer on the wall. Moreover, the denser gas near the wall indicates more thermal accommodation, and contradictorily, the displacement of the shock wave indicates less thermal accommodation. Hence, the conclusion is that mass does indeed "disappear" not only because the density profiles for the two different gases cannot be explained simply by a change in thermal accommodation but also because these profiles show a significant change in the amount of adsorption by the wall.

In addition to the comparison of experimental results for different gases and the comparison of these experimental results with Monte Carlo calculations, the entire experimental procedure is scrutinized. A comprehensive review of instrumental effects and data reduction techniques revealed

several small errors which were corrected. Improving the numerical integration used in the mass balance calculations accounts for approximately 25% of the mass defect. In some instances, (at the highest initial densities) another 10% of the missing mass can be attributed to multiple scattering of the electron beam in the thermal layer near the wall. On the other hand, several other possible effects are shown to have no influence on the measured mass defect at the conditions of the present experiments. These include multiple scattering at low initial densities, changes in the instrumental calibration constant due to the proximity of the aluminum end wall, shifts in distance between the beam and end wall caused by vibrations initiated by the opening of the diaphragm, loss of mass through the cutouts in the end-wall simulator, Piva's ruler-and-magnifying-glass data reduction technique, and certain procedures which might have led to systematic error.

Thus, the new experimental results verify Piva and Sturtevant's original conclusion that mass disappears at least temporarily from the region behind the reflected shock wave; the density profiles of a shock wave in neon reflecting from a wall and an investigation of experimental techniques substantiate the previous results.

II.2 Variations in the Amount of Adsorption

II.2.1 Description of Piva's Experiment

A complete description of the experiment and the procedures may be found in Piva's thesis[39]. The basic experiment is performed as a shock wave reflects from a moveable end wall. An electron beam densitometer[10] (figure 29) records density vs. time (figure 30) at a fixed distance from the end wall. After density traces at different distances from the wall have been synchronized so that the incoming shock approaches the wall at a constant velocity, they are cross plotted giving a family of isochrones, curves of density vs. distance from the wall at selected times (figure 31). Finally, the mass balance, figure 28, is calculated from the data in figure 31 and the continuity equation.

After the mass defect shown in figure 28 has been verified (see section II.4), it is clear that adsorption by a solid surface is an important boundary condition. Then one question which arises is can it be modeled in the Monte Carlo calculation, and the answer is, of course, yes. However, the reliability of such a calculation is increased if 1) the model for the adsorption boundary condition is based on the answer to a more immediate problem - identifying a parameter which influences the amount of adsorption - and 2) the Monte Carlo calculation can predict the measured variations in adsorption. Therefore, three modifications

of Piva's experiment are tried in order to vary the amount of missing mass (or adsorption): 1) changing the test gas from argon to neon, 2) attempting to change the nature of the adsorbed gas layer formed on "unclean" surfaces by exposing the surface to a different gas, and 3) changing the end wall from aluminum to brass. Only the first - changing the test gas - produces a substantial change in the amount of missing mass. The other two methods may produce changes, but the changes are so small that they are indistinguishable from scatter. Piva himself changed the end wall material from aluminum to brass but found no change in the amount of missing mass.

II.2.2 Neon Density Profiles

Piva's experiment is repeated with neon as the test gas. In figure 32 the density profiles of a shock wave in neon reflecting from an end wall are at the same initial conditions as the profiles for argon shown in figure 31. The two figures have the same characteristics (in fact they are nearly identical) so that the neon results need not be discussed in detail. It should be noted that the subscript 1 indicates initial conditions (those ahead of the incident shock), the subscript 2 refers to conditions behind the incoming shock, and the subscript 5 indicates conditions behind a shock reflecting from an adiabatic, nonadsorbing wall.

The comparison of the results shown in figure 33 is very important because this is the figure which makes it obvious that the amount of adsorption has changed. On this plot not only does the neon reflected shock precede the argon one but also the densities in the thermal layer are greater for neon than for argon. This is a contradiction which cannot be explained solely by thermal accommodation. (It was explained earlier that a lower thermal accommodation coefficient - a fact which is true for neon on clean surfaces and which is independent of the molecular weight of the surface molecules - produces a faster reflected shock. On the other hand, higher densities are produced by more thermal accommodation.) However, the contradiction between

the higher densities indicating more thermal accommodation and the displacement of the shock indicating less thermal accommodation can be explained by introducing a second phenomenon, e.g., adsorption. Less adsorption results in higher densities near the wall, and since this would induce a lower velocity towards the wall, less adsorption also results in higher shock velocities.

No less important than the comparison of the density profiles for the reflecting shocks is the mass balance calculation shown in figure 34. For the same initial pressure and Mach number the amount of missing mass in the case of neon is half of that for argon. In figure 34 the argon results from Piva's original data have been recalculated using the same improved numerical technique (described in section II.4.2) that was used to obtain the new neon curve. Had the neon profiles indicated a negative ψ (excess mass in the region behind the reflected shock) this would have indicated another effect was more important than adsorption. Because this situation does not occur, that is, because the mass balance shows that less neon is unaccounted for than for argon, the comparison of the neon and argon profiles is convincing proof that adsorption occurs at the end wall.

II.2.3 The Memory Effect

The reflecting shock experiment was repeated in order to see if a memory effect, which has been observed when calibrating hot wires in mixtures[40] and when measuring thermal accommodation coefficients[37], could be observed. According to Tombach[40] (Way and Libby[41] claimed that they did not encounter this effect) the calibration "constants" of King's law[40] for a platinum hot wire took several hours to return to their original values for air after the wire had remained in helium for an extended period of time. Tombach attributed this behavior to adsorption. Also Eggleton and Tompkins[37] reported that small amounts of impurities - H_2, N_2, and O_2 - significantly increased the thermal accommodation coefficient of neon on an iron wire and that this adsorption effect, which occurs in 30 - 60 minutes, appeared to be reversible. For example, they found that the increase in α due to the admission of an N_2 impurity could be reduced to the normal value α for an O_2 impurity by the admission of O_2. In spite of these memory effects[37,40], a memory effect, which would have changed the reflecting shock wave density profiles if either the thermal accommodation coefficient or the amount of adsorption were changed, was not observed for the reflecting shock experiment performed after the aluminum end wall had been exposed to helium.

II.2.3a Experimental Procedure

During the search for a memory effect dependent upon the exposure of aluminum to argon and helium, the shock tube operating procedure described by Piva[39] is modified so that helium is admitted to the test section after evacuating the tube below one micron Hg. After a waiting period, either two or eighteen hours, the tube is re-evacuated, and the normal procedure is resumed. All runs are made with the same separation, 3.5 mm. ($x/\lambda_2 \simeq 4.7$), between the electron beam and moveable end wall (figure 29). At this separation the reflecting shock is distinguishable from the incoming shock, see figure 35, and the outer regions of the thermal layer can be seen at times greater than $t/\tau_2 = 25$. Density measurements at a single separation are sufficient for detecting a memory effect as long as both the shock location and the thermal layer are visible. This is because, as will be apparent after reading the sections on the Monte Carlo results and the experiment in neon, the thermal layer thickness and the shock location are sufficient to characterize a density profile and hence the missing mass.

II.2.3b Results of Experiments with Helium

The scatter between results of experiments in which both the pressure of the He and the time between re-evacuating and firing the shock tube are varied is no greater than that typically observed by Piva[39] while doing

the original experiment. The density histories are shown in figure 35; Table VI lists the modified run conditions. In figure 35 the overlapping curves have the same reflected shock location at times close to $t/\tau_2 = 18$, and furthermore, the coincidence of the curves implies that the trajectory and thermal layer are the same for all five runs. Although identical curves of ρ vs. t might result from other combinations of adsorption and thermal accommodation, this is considered unlikely.

At any given instant the thermal layer close to the wall may actually vary in thickness for the different run conditions listed in Table VI, but because of the difficulty of calibrating memory effect runs made with separations less than $x/\lambda_2 \simeq 4.7$, measurements even of very large changes in density closer to the wall would never be conclusive. Liberally interpreted, figure 35 may show a small effect due to exposing the wall to He. However, the effect is too small to affect significantly the amount of missing mass. Thus, the experiments show that the memory effect (and small amounts of impurities, i.e., helium) have no effect on the amount of missing mass.

II.3 The Monte Carlo Molecular Simulation Method

The Monte Carlo method developed by Bird[11-15] and described in section I.4 is one of the most powerful techniques for theoretically predicting a rarefied gas flow because it depends only upon the choice of intermolecular potential and the flow boundary conditions. For many flows[11-15, 18-21] the potential and boundary conditions are known sufficiently accurately to provide agreement with experiments; for example, even the hard sphere or simple repulsive potentials are accurate enough for Monte Carlo reflected shock calculations because these potentials give good results at room temperature and because the approximation to the true potential improves as collision energy (temperature) increases. However, experience has shown that the correct boundary condition at a wall is more important than the correct intermolecular potential. Thus, the Monte Carlo calculation is unreliable, not because it gives incorrect answers for a given boundary condition, but because this condition may be a poor approximation to the real one. Once the correct conditions are known, the Monte Carlo method can be expected to duplicate the experiments.

Some density profiles, figures 36-40 which will be discussed later, have been calculated for a shock wave reflecting from a thermally accommodating wall. Apparently, thermal accommodation alone is not sufficient to reproduce

the experimental results. This inadequacy implies that the boundary condition used in the Monte Carlo calculation is wrong because the experimental results have been verified. Because of its sensitivity to the boundary condition, the Monte Carlo method can be helpful in finding those boundary conditions which reproduce the experimentally measured shock reflection.

II.3.1 Description of Monte Carlo Calculations

The general Monte Carlo procedure is summarized in section I.4. Adapting the procedure used for the shock structure problem to the reflecting shock is simple. The laboratory coordinate system is used, and the flow time (see figure 3) is allowed to continue past time t_r and t_j in order to let the reflected shock develop. Although the sampling of the distribution function is still the same, the unsteadiness decreases the efficiency of obtaining large sample sizes. Because the flow conditions at successive times are no longer the same, statistical scatter in an unsteady flow can be reduced only by recycling the x-t calculations and sampling at identical times. Specifically, for an unsteady calculation one additional sample is obtained during each period consisting of a few uncoupling intervals Δt .

The boundary condition for a thermally accommodating wall is easily applied. The thermal accommodation coefficient is defined as the ratio of the energy a particle loses before being reflected to the energy it would lose before reaching thermal equilibrium with the wall:

$$\alpha = \frac{\epsilon_\infty - \epsilon_r}{\epsilon_\infty - \epsilon_w} \qquad 2.3\text{-}1$$

Here, ϵ_∞ is the average energy of the gas molecule in equilibrium far away from the wall, ϵ_r is the energy of

the gas molecule when it leaves the wall, and ϵ_w is the energy of the gas molecule if it were in equilibrium with the wall. The thermal accommodation coefficient may also be thought of either in terms of the energy flux as the efficiency of the energy transfer between the solid and gas or in terms of molecular interactions as the fraction of molecules which have diffuse reflections. During the movement calculations whenever a particle strikes the end wall, it can be specified that the molecule is reflected either diffusely or specularly. The fraction of molecules that are reflected diffusely are re-emitted with a Maxwell Boltzmann velocity distribution appropriate to the constant wall temperature. All other molecules have specular reflections in which the kinetic energy remains unchanged and the velocity component normal to the wall reverses.

II.3.2 Results of the Monte Carlo Thermal Accommodation Calculations

Density profiles of a shock wave reflecting from a thermally accommodating end wall are computed for $\alpha = 1.0$ and $\alpha = 0.25$. In addition the author is indebted to G. S. Deiwert[42] who provided him with other profiles for thermal accommodation coefficients of $\alpha = 1.0, 0.75, 0.25$ and 0.0 obtained using Bird's technique and using a simple repulsive potential $\Phi = Kr^{-11}$. In figures 36 and 37 density profiles from these two independent sources are compared at the common values of $\alpha = 1.0$ and 0.25. For the case of $\alpha = 1.0$ the potentials used in the Monte Carlo calculations are the same, $\Phi = Kr^{-11}$. In the case of $\alpha = 0.25$ (figure 37) the agreement between the results reconfirms the unimportance of using an accurate intermolecular potential since the Bird Monte Carlo results are for the hard sphere potential.

The effects of thermal accommodation are shown in figure 38. Without thermal accommodation there should, of course, be no thermal layer at the wall. This situation, $\alpha = 0$, corresponds to both a shock reflecting from an adiabatic wall and to the case in which molecules reflect specularly from the wall. It was noted that Deiwert's profiles for $\alpha = 0$ showed no thermal layer, and his reflected shock location coincided with the location of a Rankine-Hugoniot shock reflecting from an adiabatic wall. The other profiles

on figure 38 demonstrate that increasing the amount of thermal accommodation has two effects: 1) the thickness of the thermal layer increases and 2) the shock reflects more slowly. More thermal accommodation transfers more heat from the gas to the wall and thereby lowers the temperature of the gas and increases its density near the wall. The speed of the reflected shock is largely controlled by the magnitude of the velocity that is induced toward the wall in order to supply the thermal layer with the required mass. The results of the calculations indicate that at $t/\tau_2 = 25$ this induced velocity is approximately $\frac{1}{4}\sqrt{RT_1}$ for the $\alpha = 0.25$ case and about $\frac{1}{2}\sqrt{RT_1}$ for the $\alpha = 1.0$ case.

Some Monte Carlo density results at various times are plotted as points on figures 39 and 40 which have the argon experimental curves superimposed. These figures give Monte Carlo profiles at four or five different times. The thermal accommodation coefficients, $\alpha = 1.0$ for figure 39 and $\alpha = 0.75$ for figure 40, are the two which are most useful for analyzing the present experimental results. These Monte Carlo profiles are the same ones shown in figures 45 and 46 along with the experimental neon profiles.

A measure of the statistical fluctuations in the results of these calculations can be seen in the region immediately behind the reflecting shock in figure 39.

According to the Rankine-Hugoniot conditions for a shock reflecting from an adiabatic wall, all densities should be approximately 1.0 (as shown for the case of $\alpha = 0$ in figure 38). The deviations ± 0.1 are attributed to statistical scatter.

Calculations of shock wave structure are customarily normalized by the mean free path and the collision time ahead of the incident shock. When reflected shocks are studied, it would therefore seem reasonable that the results should be normalized with conditions ahead of the reflected shock. In order to do this, the ratio λ_2/λ_1, a function of Mach number and intermolecular potential, is needed. For simplicity, both the Monte Carlo and experimental profiles are customarily normalized by the hard sphere mean free path which is defined in terms of the viscosity μ

$$\lambda = \frac{16}{5}\sqrt{\frac{\gamma}{2\pi}}\,\frac{\mu}{\rho a} \,. \qquad 2.3\text{-}2$$

The mean collision time is defined as

$$\tau = \lambda/\bar{c} \qquad 2.3\text{-}3$$

where $\bar{c}$ is the mean speed of the molecules

$$\bar{c} = a\sqrt{\frac{8}{\pi\gamma}} \,. \qquad 2.3\text{-}4$$

According to Hirshfelder[7] the viscosity, μ, of a gas having a simple repulsive potential, the model used for the Monte Carlo calculations of reflected shock waves, is

$$\mu = \frac{5}{8}\sqrt{\frac{km}{\pi}}\left(\frac{k}{sK}\right)^{\frac{2}{s}} T^{\left(\frac{1}{2}+\frac{2}{s}\right)} \Big/ \Gamma\left(4-\frac{2}{s}\right) A^{(2)}(s) \quad . \qquad 2.3\text{-}5$$

Substitution of equations 2.3-2 and 2.3-5 into

$$a_2/a_1 = (T_2/T_1)^{\frac{1}{2}}$$

gives:

$$\frac{\lambda_1}{\lambda_2} = \frac{\mu_1}{\mu_2}\frac{\rho_2}{\rho_1}\frac{a_2}{a_1} = \frac{\rho_2}{\rho_1}\left(\frac{T_1}{T_2}\right)^{\frac{2}{s}} \quad . \qquad 2.3\text{-}6$$

(Remember that ahead of the incident shock the flow conditions are referred to by the subscript 1 and that behind the incident shock the conditions referred to by the subscript 2 are evaluated using the Rankine-Hugoniot shock jump relations and the measured Mach number.) The distances and times of the Monte Carlo profiles are easily renormalized with λ_1/λ_2 and τ_1/τ_2. Then the origin $t/\tau_2 = 0$ is chosen so that at $t/\tau_2 = 0$ the incident shock wave is just starting to interact with the wall.

II.4 Verification of "Missing Mass"

A discovery as startling as missing mass should be verified in order to be sure that the effect is real and not a result of some oversight. This section, by describing investigations of the accuracy of the original procedures and by reporting that only small errors were caused by these procedures, verifies that mass is indeed missing. Ordinarily, it would be desirable to have a second independent confirmation of missing mass. However, this has not yet been possible.

Past experience with the electron beam equipment helps eliminate some improbable causes of error immediately. The ability to repeat Piva's experiment and to obtain not only the same oscillograms but also the same values of ρ vs. t (as in figure 30) shows that any errors would have to occur on every run. An example would be flow nonuniformities around the cage or needle; however, these are thought to be small[39]. Another likely source of error is the assumption that K in the exponential attenuation law used to convert the current to density

$$I = I_o e^{-K\rho} \qquad 2.4\text{-}1$$

is constant (i.e., not $K = K(\rho)$). The behavior of K is carefully examined (see section II.4.2) because the Monte Carlo calculations for large α's $\simeq 0.9$ predict shock

locations which agree with the experimental measurements but predict more mass in the dense thermal layer than the experiments show. Other likely mistakes are in the numerical calculations required for cross plotting or in the numerical integrations; these are not likely to be due to arithmetic errors but rather to poor choices of numerical techniques. For example, in cross plotting which requires fitting polynomials to points, an error might be a poor choice for the order of polynomial or too few points for a least squares fit. The numerical integration could be very inaccurate especially if either the derivatives or the intervals are very large.

II.4.1 Mass Balance

The continuity equation says that during any time interval the increase of mass between the wall and a fixed location must equal the flux of mass across the fixed boundary. This is called a mass balance; the appropriate equation is:

$$\int_{W}^{X} \frac{\rho(x,t) - \rho(x,t_o)}{\rho_2} dx = \int_{t_o}^{t} \rho(X,\tau)u(X,\tau)d\tau \qquad 2.4\text{-}2$$

where X is the location of the measuring station farthest from the wall, where time t_o is some initial time, and where W indicates that density is linearly extrapolated to the wall using the values at the two measuring stations closest to the wall. The missing mass, ψ, is defined as the flux of mass into this region minus the measured increase of mass there:

$$\psi = \int_{t_o}^{t} \frac{\rho(X,\tau)u(X,\tau)}{\rho_2 \quad \bar{c}_2} d\left(\frac{\tau}{\tau_2}\right) - \int_{W}^{X} \frac{\rho(x,t) - \rho(x,t_o)}{\rho_2} d\left(\frac{x}{\lambda_2}\right) \qquad 2.4\text{-}3$$

The physical significance of these terms is shown in figure 41.

Piva did not investigate the accuracy of the integration of the LHS of 2.4-2 by using different techniques. His single approximation was to adapt Simpson's method to unequal intervals. The integration is by no means trivial.

Since the densities are known at only a few X's , the integration can be inaccurate, especially where derivatives are large. Because the densities near the wall are lower than those of the Monte Carlo calculation for a nonadsorbing wall, the inaccuracy of integration is not responsible for all the missing mass. However, since the experimental densities are found to be correct, the inaccurate integration is the largest single error in the determination of the amount of missing mass. The missing mass calculations are repeated using another numerical integration technique: one point on either side of an interval is used along with the end points of the interval to compute two second degree polynomials which when integrated in the interval and added together equal twice the mass. This integration reduces the amount of missing mass from 20% to 15% of the mass that should be behind the reflected shock. The results of this improved calculation are shown in figure 34 (cf. figure 28).

Different values of X and t_o are used in the mass balance equation. Varying X and yet obtaining the same amounts of missing mass shows that the missing mass is not dependent on the mass flux at any one X location, i.e., data from any single run. Changing t_o eliminates the possibility that any curve $\rho(x, t_o)$ is in error. The latter is unlikely first because $\rho(x, t_o)$ depends upon data at many different x/λ_2 locations, second because the

shock approaches at a uniform speed, and third because the incident shock profiles (see figure 30) are the same. The other mistake that can be made in determining an isochrone in addition to a poor choice of polynomial for cross plotting is selecting the improper additive constant to synchronize the density histories. This would result in all the isochrones at one X location being distorted since the time increments between isochrones are determined exactly from the density traces. Thus, smooth, nonintersecting isochrones indicate correct isochrones.

Piva's original approximation to the right hand side of equation 4.1-1,

$$\frac{u_2}{\bar{c}_2} \frac{\rho(t) + \rho(t_o)}{2\rho_2} \left[t - t_o\right] / \tau_2 , \qquad 2.4\text{-}4$$

was successively improved by

$$\frac{u_2}{\rho_2 \bar{c}_2} \int_{t_o}^{t} \rho(X,\tau) \, d\left(\frac{\tau}{\tau_2}\right) \qquad 2.4\text{-}5$$

and the correct value

$$\int_{t_o}^{t} \frac{\rho(X,\tau) \; u \; (X,\tau)}{\rho_2 \quad \bar{c}_2} \, d\left(\frac{\tau}{\tau_2}\right) \qquad 2.4\text{-}6$$

without noticeably affecting the mass balance. In addition to the improved integration technique, a different approach

is used for the mass balance, and the amount of missing mass calculated by this new method agrees with that of the improved calculation. The original density histories at their X_i's , the normalized distance between the end wall and electron beam, are used to generate profiles $\rho(X, t/\tau_2)$ at intermediate X's . This alternate procedure assumes the existence of a smoothly varying shock speed and a nearly uniform profile between the measurement stations. The soundness of these assumptions is easily seen on figure 42. Lines of constant ρ are assumed to be piecewise parabolic in x/λ_2 and t/τ_2 . The ρ's at intermediate X's are computed using a least squares fit. Then the integration is performed with the smaller interval size of the X's . A tenfold decrease in interval size gives the same answers as the improved mass balance. Therefore, it is assumed that the integral has converged and that no further increase in accuracy is possible.

II.4.2 High Density Calibration

Since for an $\alpha \simeq 0.9$ the molecular simulation technique which conserves mass agrees with the electron beam measurements of shock wave location, the density calibration especially for high densities is re-examined. This is strongly motivated by faith in the Monte Carlo calculation and by the disagreement with it which occurs only in high density regions. However, the agreement with the shock trajectory does not preclude the loss of mass because, obviously, the trajectory produced by diffuse reflection can also be produced by combinations of specular reflection and adsorption, combinations which do not conserve mass in the gas phase. This is another way of saying that the Monte Carlo calculations are no better than the boundary condition used to model the gas-surface interaction

The high density calibrations are made in two ways, and the K's (see equation 2.4-1) from both methods show moderately good agreement. For the dynamic calibrations a shock wave is generated in a gas denser than is normally used for the run conditions. Then K is determined from points on each density history which are identified as ρ_1 and ρ_2 and from the ratio ρ_2/ρ_1 which is a known function of the Mach number. The numbers next to the dynamic calibration symbols on figure 43 are the shock tube run numbers for that particular dynamic calibration. The static

calibrations are made by admitting a known density into the shock tube test section and measuring the ratio of current leaving the needle, I_N (held constant during a calibration), to the current reaching the Faraday cup, I. The error bars on the static calibration, figure 43, delimit the resolution of the ruler-and-magnifying-glass data reduction technique when the ratio of the currents is large. This error is reduced when measuring densities in a shock wave. The ratio of the currents is reduced somewhat by setting the partially attenuated cage current at ρ_1 to full scale on the oscilloscope. This is possible when using the dynamic calibration because only relative currents are required. An additional decrease in error is provided by the more accurate data reduction technique described by Barcelo[22].

Two separate high density effects occur near the end wall, but because the initial densities are low, neither effect is large enough to account for more than 10% of the missing mass. First, the approximation of a constant $K(\rho)$ that Piva used for computing the density histories (see equation 2.4-1) from each experimental run breaks down at high densities as shown by the dynamic and static calibrations in figure 43. For example, correcting the densities in the case of $M_s = 6.0$, $p_1 = 35$ microns Hg of argon reduces the missing mass at $t/\tau_2 = 25$ from 15% to 13% of the total mass. A second, counteracting effect is caused by the proximity of the electron beam and the aluminum end wall.

High density static calibrations made near the end wall are shown in figure 44, and a comparison of figures 43 and 44 shows that the effect of the wall proximity is even less important than the constant K approximation. Both high density effects are caused by changes in the number of secondary electron-atom collisions which alter the current by redirecting a fraction of the already scattered electrons toward the Faraday cage. The secondary collisions cause the breakdown of the constant K approximation simply because this approximation applies only for single scattering - out of the electron beam; the presence of the conducting wall shifts K back towards the single scattering result by grounding some electrons before their secondary collisions.

The apparent conflict between our observation that increasing density causes the transmitted current to rise above the single scattering result and Center's[43] observation that increasing density causes the centerline current to fall below the single scattering value is attributed to differences in target thickness. Our gap and maximum density have the same target thickness as his smallest one, for which he himself claims that electron optics and needle geometry are important in determining the beam dispersion. The small target thickness is undoubtedly responsible for another phenomena - scatter in calibration

constant. Although the needle geometry is unchanged, changes in electron optics, which are caused by variations in the voltages of the grid-biasing batteries, do cause changes in the calibration constant by changing the dispersion. However, a dynamic calibration for each run removes any dependence of density on the electron optics.

II.4.3 Distance Measurement

The distance between the end wall and the beam is measured by a micrometric jack screw. The zero setting, $d = x/\lambda_2 = 0$, is determined prior to each run by moving the end wall to the location at which one half of the beam current reaches the Faraday cage. This definition of $d = 0$ depends upon the beam and end wall being coplanar. Any departure from a coplaner alignment would produce consistently low values of X_i's making the wall appear too close to the beam and thus accounting for missing mass. In order to measure the influence of alignment on the mass balance, the beam and end wall have been carefully realigned perpendicular ($\pm$ 5 x 10^{-4} radians) to the shock tube centerline, and the density profiles are remeasured at $M_s = 6.0$, $p_1 = 35$ microns Hg of argon. As anticipated, this repetition of the experimental runs shows the same profiles and hence the same amount of missing mass as the original runs showed. Additional runs are made varying the coplanar angle by $\pm$ 5 x 10^{-3} radians. Minor changes occur in the density profiles near the wall; at moderate distances the change in angle causes changes in the profile which appear to be scatter and are roughly equivalent to a change in distance of $\pm$ ¼ mm. However, the largest change in mass caused by these angular variations, which are much greater than those due to poor alignment, is 0.4% of the total mass. The conclusion is that the amount of missing mass is insensitive

to the alignment of the beam and wall.

An assumption implicit in setting the beam distance is that the static setting $d = 0$ is unchanged when the shock wave is propagating in the shock tube. This is true if the bellows (see figure 29) are sufficiently flexible to allow the beam and end wall to remain stationary while the shock tube vibrates. The beam is set at $d = 0$, and a run is made in order to demonstrate that vibrations caused by the opening of the diaphragm do not shift the beam and end wall relative to each other. In the dynamic case one half of the beam is still cut off just as in the static setting of $d = 0$. Thus, any shift must be much smaller than the diameter of the beam which is about 0.5 mm. A shift of $\pm$ 0.1 mm. would result in 70% to 30% of the beam being cut off. Such a large departure from 50% would certainly be noticed so that this value $\pm$ 0.1 mm. is used as the maximum shift. A shift of -0.9 mm. and linear extrapolation of the density to the end wall are required to account for the missing mass at $M_s = 6$, $p_1 = 15$. Thus, the worst possible shift, -0.1 mm., is insufficient to explain more than about 10% of the missing mass.

II.5 Discussion

Because the accuracy of the experimental technique is verified in section II.4, the comparison of the density profiles in neon and argon shown in figure 33 provides such a convincing proof of adsorption that any further discussion is unnecessary. However, significant points can be made by comparing the density profiles with other avilable data and with the Monte Carlo data. On the other hand, the failure of the memory effect to produce any change has not succeeded in increasing the understanding of the gas-surface interaction problem.

II.5.1 Comparison of Experimental and Monte Carlo Results

Figures 39, 40, 45, and 46 superimpose a few experimental density profiles on the Monte Carlo profiles for thermal accommodation coefficients $\alpha = 1.0$ and 0.75. The Monte Carlo points are known at only a few discrete t/τ_2's. Densities at t/τ_2's closer to the integral values of t/τ_2 shown for the experimental results are not available. Nevertheless, the present curves are adequate for qualitative comparisons with experimental results.

Figure 38 allows an estimate to be made for the α which would cause the Monte Carlo result to coincide with the experimental curves. This gives an $\alpha \simeq 0.9$ for argon, and comparing figures 33 and 38 gives an estimate of $\alpha \simeq 0.85$ for neon. For both test gases, however, the measured densities in the thermal layer are lower than the predicted ones. In addition the estimated α's are much higher than the clean surface values for neon and argon.

Another experiment on reflecting shock waves is available for comparison with the argon results. Our $\alpha = 0.9$ is slightly higher than that reported by Hanson[44] whose experiments were also made with technical surfaces - ones which had not been carefully cleaned before the experiment. Hanson measured end wall pressure and heat transfer simultaneously. These quantities were compared with the values Deiwert[42] predicted in order to determine the thermal accommodation coefficient. When this was done, they found

agreement for $\alpha \simeq 0.75$ (cf. shock location implies that $\alpha \simeq 0.9$ for argon according to figure 38). Now if thermal accommodation were the only boundary condition, one value of α would have to predict correctly momentum flux, heat flux, and shock location. At this time, Hanson's results are still preliminary; he might re-evaluate his experimental technique. The nature of the density measurements, particularly the traces shown in figure 30, leaves no doubt about the $\alpha \simeq 0.9$ based on shock location. Furthermore, this value of α is verified by a completely independent measurement[45] made with heat transfer gauges mounted on the end wall at known distances from it. If Hanson does not revise his preliminary values for α, the disagreement in α between Hanson's measurements and the density measurements for reflecting shock location provides additional evidence that thermal accommodation is not the only boundary effect.

Therefore, because of our confidence in the Monte Carlo technique and in the experiments, we must conclude that an additional parameter is needed in order to produce the same shock trajectory with a lower thermal accommodation coefficient. Mass accommodation is one such parameter, and fortuitously, this is exactly what density measurements require. Whether or not it will make the momentum flux and heat flux measurements consistent with the density measurements is presently being investigated by G.S. Deiwert.

II.5.2 Adsorption

The amount of missing mass would cover the surface lattice sites with approximately one monolayer of gas atoms. The number of monolayers is the ratio of the number of missing molecules per unit area, $\rho_2 \lambda_2 \psi$, to the number of molecules per unit area on an aluminum surface, N. Aluminum is an FCC crystal with a lattice constant of 4.05Å. The spacing between molecules is $a = \sqrt{2} / 2 * 4.05Å = 2.86Å$. If one of the crystal axes is perpendicular to the surface, the number of surface molecules per square centimeter is $N = a^{-2}$. At $M_s = 6.0$, $p_1 = 35$ μ Hg of argon, one monolayer on a perfectly smooth aluminum crystal corresponds to a ψ of:

$$\psi_1 = \frac{m}{\rho_2 \lambda_2 a^2} = \frac{40 \times 1.660 \times 10^{-24} \text{ gm}}{0.278 \text{ gm/m}^3 \times 0.745 \text{ mm} \times (2.86Å)^2} = 3.9. \qquad 2.5\text{-}1$$

If, as is likely, an engineering surface has a substantially larger microscopic surface area than a perfect crystal, then $\psi = 3.9$ would imply a coverage of somewhat less than one monolayer.

The accuracy of Monte Carlo predictions for flows interacting with solid boundaries can, obviously, be improved if the dependence of the adsorption boundary condition on the other parameters in the problem is known. Presently, insufficient data have been obtained from the shock reflection measurements to determine this dependence, but the measurements do serve to confirm the existence of larger

amounts of adsorption than anticipated and to suggest areas for further investigation. Until more information is available, the soundness of hypothetical models for adsorption can be tested by trying to rescale the missing mass curves of ψ vs. t/τ_2 to a single curve. For example, normalizing ψ with some of the more convenient variables, ρ_2, ρ_5, p_2, p_5, λ_2, τ_2, $\frac{1}{4}\rho_2\bar{c}_2$, or $\frac{1}{4}\rho_5\bar{c}_5$ increases the relative scatter between curves. Multiplying ψ by $(m/\rho_5)^{2/3} / a^2$, where a is the lattice constant of the solid, gives a new parameter for which the scatter between the six curves is reduced somewhat. This parameter was obtained by noticing that $\psi \sim (\rho_5)^{2/3}$ and then by non-dimensionalizing ρ_5 with m and a. Hence, the dependence on a is untested; it is simply a convenient length. However, since ψ is proportional to $(\rho_5)^{2/3}$ (i.e., to the number of molecules per unit area), this suggests an adsorption rate related to the number of gas molecules adjacent to the wall. The increase in ψ with time would occur because of the growing thermal layer. One might expect that if the density at the wall were known accurately, then the dependence of ψ on time could be removed by scaling the missing mass with $(\rho_{wall})^{2/3}$.

The well known[46-48] estimate for the number of molecules which can be physically adsorbed per unit area is equal to the product of the number of molecules incident on the

adsorbing surface per unit area per unit time and the average time a molecule spends on the wall. Thus, the number of monolayers η is

$$\eta = \tfrac{1}{4}\, n\, \bar{c}\ \ a^2\ \ \tau_o\, e^{Q/RT}\ , \qquad 2.5\text{-}2$$

where $\tfrac{1}{4}\, n\, \bar{c}$ is the flux to the wall, where τ_o is a characteristic vibration time approximately 10^{-13} sec., and where Q is the heat of adsorption. At the same conditions used in the previous example $\tfrac{1}{4}\, n_1\, \bar{c}_1$ is approximately 10^{19} molecules/cm.^{2} sec., and $\tfrac{1}{4}\, n_5\, \bar{c}_5$ is approximately fifty times as great. The heat of adsorption, Q, for argon on aluminum may be taken[49] as 2.8 kcal./mole From equation 2.5-2,

$$\eta \simeq 10^{19} \times (2.86)^2 \times 10^{-16} \times 10^{-13} \times e^{4.73} \simeq 10^{-7}\ .$$

On the other hand the shock reflection measurements show that ψ (i.e., the number of molecules on the surface) varies approximately as n. At conditions "5" approximately one monolayer is on the wall; consequently, 1/10 monolayer would be on the wall at conditions "1". Even using the more generally accepted result[46-48] that adsorption varies as the number flux to the wall, we conclude 1/50 of a monolayer would have to be adsorbed at conditions "1". This crude calculation shows that physical adsorption is not the

cause of the mass defect. In fact, according to equation 2.5-2, the experiments would suggest a heat of adsorption $Q \simeq 11$ kcal./mole, a value which is too high for argon but typical of heavier molecules such as the molecules of many organic substances.

Thus, two contradicting observations exist: 1) the experiments show that the missing mass must be on the wall and yet 2) estimates of physical adsorption show that the wall cannot adsorb this much noble gas. The values of the variables in equation 2.5-2 are accurate with the possible exception of $\tau = \tau_o e^{Q/RT}$. Moreover, τ can be affected by the conditions of the solid surface which, for example, are known[36] to increase the accommodation coefficient. De Boer[46] has shown that in practical cases capillaries can increase τ several orders of magnitude. A similar effect might be caused by the penetration of argon atoms into the lattice of a layer of impurities on the surface of the aluminum. Such situations almost certainly exist; the surface of the aluminum end wall probably has a layer of O_2, probably has residues from organic cleaning agents, and has an unknown roughness. These effects might be the cause of the differences in the amounts of adsorption between the experimental case and the ideal case.

II.5.3 Memory Effect

So little is known about the memory effect that explanations for why no effect is observed are mere speculations. Perhaps the accommodation coefficient is not affected because of the substitutions of argon for air and aluminum for platinum. The contaminants[37] which are known to change the thermal accommodation coefficient are the diatomic molecules H_2, O_2, and in addition N_2 for which the change is reversible. Using two monatomic gases such as helium and argon may not change α, but the case of air and argon has in reality already been done because the end wall is exposed to air at atmospheric pressure between each run.[39]

If it is assumed that the memory effect does occur, another uncertainty is its duration. The available evidence, although not directly applicable to helium and argon on an aluminum surface, indicates that for some cases the change in α should be large enough to be observed by the reflecting shock experiment. Tombach[40], whose experiments were done near atmospheric pressure, reported that the memory effect lasted a few hours. At pressures comparable to the initial pressure of the reflecting shock experiment, Thomas[36] measured increases in α of 3% per hour, Eggleton and Tompkins[37] measured increases of 10% per hour, and according to Thomas, Roberts had measured increases in α as large as 800% per hour. When Eggleton and Tompkins added trace amounts of an impurity, α increased at a rate of

approximately 800% per hour. A rate lower than this latter rate of change in α would have been detectable by the reflecting shock equipment. Thus, the fact that no memory effect was observed suggests that any change in α, if any at all occurred because of the soaking in helium, was too small or that the reversion in α occurred too quickly. However, the possibility remains that in other situations, for example, with different wall materials, with N_2 instead of He, or with higher soaking pressures, the shock reflection experiment could detect changes in the wall boundary conditions due to a memory effect.

II.6 Summary

The new experimental results verify Piva and Sturtevant's original conclusion that mass disappears at least temporarily from the region behind the reflected shock wave. The density profiles of a shock wave in neon reflecting from a wall and the investigation of experimental technique indicate missing mass directly. The substitution of neon for argon makes the experiment a relative one. Even if the experimental technique were inaccurate in absolute value, the results for different gases but at the same initial conditions show that more mass disappears in one case than in the other. There can be no doubt that the fundamental observation - missing mass - is correct. The investigation of the techniques reveals only small errors in the amount of missing mass. Thus, because of this independent investigation we are confident that the magnitude of the amount of missing mass is nearly correct.

In addition to the density experiments two other results, Hanson's[44] experiment and the Monte Carlo calculations[42], support the argument for missing mass indirectly by indicating a need for a second boundary condition to supplement thermal accommodation. Hanson's pressure and heat transfer measurements give values of thermal accommodation coefficient which differ from that determined from the density measurements of shock location. The latter are

verified by a completely independent measurement[45] made with heat transfer gauges instead of the electron beam. The different values for thermal accommodation would, of course, be unacceptable if thermal accommodation were the only adjustable parameter in the wall boundary conditions. Rather, these results imply that a second parameter, namely adsorption, must be specified in order to eliminate differing values for α . Similarly, the inability to fit results of Monte Carlo calculations to the experimental density profiles for any value of α indicates the need for another boundary condition. Therefore, the accumulated evidence indicates the need, at least during such an unsteady process, for a second gas-surface boundary condition and suggests the use of adsorption at this condition.

REFERENCES

1. Keller, J.B., and Zumino, B., J. Chem. Phys., 30, 1351 (1959).

2. Dymond, J.H., and Alder, B.J., J. Chem. Phys., 51, 309 (1969).

3. Amdur, I., Glick, C.F., and Pearlman, H., Amer. Acad. Arts Sci. Proc., 76, 101 (1948).

4. Amdur, I., and Mason, E.A., J. Chem. Phys., 22, 670 (1954), 23, 415 (1955), 23, 2268 (1955), and 25, 624 (1956).

5. Kamnev, A.B., and Leonas, V.B., Soviet Physics-Doklady, 10, 1202 (1966) and 10, 529 (1965).

6. Leonas, V.B., and Sermyagin, A.V., JETP Letters, 12, 300 (1970).

7. Hirshfelder, J.O., Curtiss, C.F., and Bird, R.B., Molecular Theory of Gases and Liquids, (Wiley, New York, 1954).

8. Whalley, E., and Schneider, W.G., J. Chem. Phys., 23, 1644 (1955).

9. Mason, E.A., and Rice, W.E., J. Chem. Phys., 22, 843 (1954)

10. Schmidt, B., J. Fluid Mech., 39, 361 (1969).

11. Bird, G.A., Rarefied Gas Dynamics, 1, 216 (Academic Press, N.Y., 1965).

12. Bird, G.A., J. Fluid Mech., 30, 479 (1967).

13. Bird, G.A., J. Fluid Mech., 31, 576 (1968).

14. Bird, G.A., Rarefied Gas Dynamics, 1, 85 and 301 (Academic Press, N.Y., 1969).

15. Bird, G.A., Phys. of Fluids, 13, 2676 (1970).

16. Russell, D., Rarefied Gas Dynamics, 1, 265 (Academic Press, N.Y., 1965).

17. Schultz-Grunow, F., and Frohn, A., Rarefied Gas Dynamics, 1, 250 (Academic Press, N.Y., 1965).

REFERENCES (cont.)

18. Bird, G.A., AIAA Journal, 4, 55 (1966).

19. Vogenitz, F.W., Bird, G.A., Broadwell, J.E., and Rungaldier, H., AIAA Journal, 6, 2388 (1968).

20. Vogenitz, F.W., Broadwell, J.E., and Bird, G.A., AIAA Journal, 8, 504 (1970).

21. Vogenitz, F.W., and Takata, G.Y., AIAA Journal, 9, 94 (1971).

22. Barcelo, B.T., Ph.D. Thesis, CIT (1971).

23. Pitzer, K.S., J. Chem. Phys., 7, 583 (1939).

24. Liepmann, H.W., To be published.

25. Liepmann, H.W., Roshko, A., Coles, D.E., and Sturtevant, B., Rev. Sci. Instr., 33, 625 (1962).

26. Liepmann, H.W., Narasimha, R., Chahine, M.T., Phys, of Fluids, 5, 1313 (1962).

27. Liepmann, H.W., and Roshko, A., Elements of Gas Dynamics, (Wiley, New York, 1957).

28. Mason, E.A., J. Chem. Phys., 22, 169 (1954).

29. Alder, B., ed., Methods in Computational Physics, 4, 109, (Academic Press, New York, 1965).

30. de Boor, C., J. Math. Phys., XLI, 212 (1962).

31. Cottrell, T.L., Discus. Farad. Soc., 22, 10 (1956).

32. Mason, E.A., and Rice, W.E., J. Chem. Phys., 22, 522 (1954).

33. Mason, E.A., J. Chem. Phys., 32, 1832 (1960).

34. Amdur, I., and Mason, E.A., Phys. of Fluids, 1, 370 1958).

35. Hartnett, J.P., Rarefied Gas Dynamics, 1, 1 (Academic Press, New York, 1961).

36. Thomas, L.B., Rarefied Gas Dynamics, 2, 155 (Academic Press, New York, 1967).

REFERENCES (cont.)

37. Eggleton, A.E.J., and Tompkins, F.C., Trans. Farad. Soc., 48, 738 (1952).

38. Piva, H.O., and Sturtevant, B., Rarefied Gas Dynamics, 1, 381 (Academic Press, New York, 1969).

39. Piva, H.O., Ph.D. Thesis, California Institute of Technology, 1968.

40. Tombach, I.H., Ph.D. Thesis, California Institute of Technology, 1969.

41. Way, J., and Libby, P.A., AIAA Journal, 9, 1567 (1971).

42. Deiwert, G.S., Ames Research Center, to be published.

43. Center, R.E., Phys. of Fluids, 13, 79 (1970).

44. Hanson, R.K., Ames Research Center, to be published.

45. Sturtevant, B., and Slachmuylders, E., Phys. of Fluids, 7, 1201 (1964).

46. De Boer, J.H., The Dynamical Character of Adsorption, (Oxford University Press, London, 1968).

47. Young, D.M., and Crowell, A.D., Physical Adsorption of Gases, (Butterworths, London, 1962).

48. Saltzburg, H., ed., Fundamentals of Gas-Surface Interactions, p. 27 (Academic Press, New York, 1967).

49. Steele, W.A., and Halsey, Jr., G.D., J. Chem. Phys., 22, 979 (1954).

50. Barker, J.A., Bobetic, M.V., and Pompe, A., Mol. Phys., 20, 347, (1971).

TABLE I
POTENTIAL PARAMETERS

	NEON			ARGON			KRYPTON			XENON		
EXP-6*	α	σ_m (Å)	ϵ/k (°K)	α	σ_m (Å)	ϵ/k (°K)	α	σ_m (A)	ϵ/k (°K)	α	σ_m (A)	ϵ/k (°K)
1. Shock Structure	13.5	3.225	30.6	13.5	3.914	111	13.5	4.246	155	13.5	4.686	204
5. Amdur & Mason	14.0	3.135	38.5	12.0	3.87	116	13.0	4.17	174	14.0	4.59	251
Mason & Rice	14.5	3.147	38.0	14.0	3.866	123	12.3	4.056	158	13.0	4.450	231
6. Whalley & Schneider				15.0	3.748	132	15.0	3.962	184	15.0	4.497	249
Saxena, et. al.	14.	2.96	66.6	14.	3.68	148						
Keeler, et. al.				13.5	3.80	123				13.5	4.45	236
LENNARD-JONES*		σ_o (Å)	ϵ/k (°K)		σ_o (Å)	ϵ/k (°K)		σ_o (Å)	ϵ/k (°K)		σ_o (Å)	ϵ/k (°K)
2. Shock Structure		2.630	66.8		3.336	138		3.621	188		4.029	233
7. Whalley & Schneider					3.41	119		3.68	167		4.075	225
8. Hirshfelder, et. al.		2.858	27.5		3.465	116		3.61	190		4.055	229
Konowalow, et. al.		2.82	36.3		3.45	119		3.60	159		3.97	228
SIMPLE REPULSIVE $\Phi = er^{-\alpha}$	α	ϵ (eV Å$^\alpha$)		α	ϵ (eV Å$^\alpha$)		α	ϵ (eV Å$^\alpha$)		α	ϵ (eV Å$^\alpha$)	
12. Shock Structure	12	1700		11	26200		10	29700		9	28500	
3. Kamnev & Leonas	7.65	78		6.06	171		7.70	1382		6.35	463	
4. Amdur and Mason	9.99	312		8.33	848		5.42	159		7.97	7050	
EXP $\Phi = \epsilon \exp(-\alpha r)$	α (Å^{-1})	ϵ (eV)		α (Å^{-1})	ϵ (eV)		α (Å^{-1})	ϵ (eV)		α (Å^{-1})	ϵ (eV)	
9. Leonas & Sermyagin	6.20	44000		3.56	2540		2.60	668		2.64	1635	

*See equations 1.1-2 and 1.1-3 as well as the footnote on page 7.

TABLE II

Experimentally Determined Shock Wave Density Profile

$$\rho = \frac{\rho - \rho_1}{\rho_2 - \rho_1}$$

X/λ_1	Ne M = 6 p_1=25,50 3 runs	Ar M = 8 p_1=25,50 5 runs	Kr M = 8 p_1 = 25 3 runs	Xe M = 8 p_1 = 15 5 runs
-8.0	0.000	0.001	0.002	0.002
-7.5	0.000	0.001	0.003	0.003
-7.0	0.000	0.002	0.005	0.004
-6.5	0.001	0.004	0.007	0.007
-6.0	0.001	0.006	0.010	0.010
-5.5	0.002	0.009	0.013	0.014
-5.0	0.005	0.013	0.019	0.020
-4.5	0.008	0.019	0.026	0.028
-4.0	0.013	0.028	0.037	0.040
-3.5	0.024	0.043	0.053	0.057
-3.0	0.041	0.062	0.077	0.081
-2.5	0.066	0.092	0.108	0.115
-2.0	0.107	0.133	0.149	0.163
-1.5	0.168	0.190	0.213	0.223
-1.0	0.257	0.266	0.297	0.299
-0.5	0.366	0.372	0.387	0.392
0.0	0.500	0.500	0.500	0.500
0.5	0.629	0.624	0.619	0.614
1.0	0.755	0.735	0.724	0.716
1.5	0.850	0.826	0.814	0.801
2.0	0.918	0.892	0.878	0.866
2.5	0.960	0.936	0.922	0.911
3.0	0.986	0.962	0.952	0.942
3.5	1.002	0.977	0.971	0.963
4.0	1.011	0.989	0.982	0.977
4.5	1.017	0.995	0.989	0.986
5.0		1.000	0.994	0.992
5.5		1.004	0.998	0.997
6.0		1.006	1.002	0.999
6.5		1.008	1.005	1.000
7.0		1.009	1.006	1.001

TABLE III

	Shock Structure exp-6			Shock Structure Lennard-Jones		
	kT_{cr}/ϵ	σ/r_{cr}	$\hbar/\sigma\sqrt{\epsilon m}$	kT_{cr}/ϵ	σ/r_{cr}	$\hbar/\sigma\sqrt{\epsilon m}$
Neon	1.447	0.524	0.0868	0.664	0.427	0.0721
Argon	1.364	0.533	0.0267	1.095	0.442	0.0281
Krypton	1.355	0.525	0.0144	1.116	0.448	0.0153
Xenon	1.419	0.533	0.0091	1.244	0.459	0.0099

TABLE IV

Molecular Simulation Shock Wave Density Profiles in a Gas with an Exp-6 Intermolecular Potential

$$\rho = \frac{\rho - \rho_1}{\rho_2 - \rho_1}$$

X/λ_1	M = 8 T* = 1.20	M = 8 T* = 1.60	M = 8 T* = 2.15	M = 8 T* = 2.50
-7.75	0.000	0.004	0.004	0.004
-7.25	0.010	0.005	0.000	-0.002
-6.75	0.006	0.007	0.000	0.003
-6.25	0.012	0.003	0.009	0.004
-5.75	0.012	0.009	0.007	0.007
-5.25	0.016	0.016	0.016	0.018
-4.75	0.023	0.023	0.024	0.011
-4.25	0.036	0.030	0.032	0.030
-3.75	0.045	0.033	0.051	0.041
-3.25	0.065	0.056	0.067	0.063
-2.75	0.086	0.071	0.083	0.080
-2.25	0.123	0.103	0.125	0.123
-1.75	0.167	0.141	0.185	0.175
-1.25	0.252	0.201	0.259	0.252
-0.75	0.319	0.277	0.338	0.360
-0.25	0.394	0.359	0.454	0.464
0.25	0.493	0.505	0.582	0.583
0.75	0.610	0.609	0.687	0.713
1.25	0.725	0.718	0.793	0.800
1.75	0.782	0.811	0.872	0.866
2.25	0.862	0.868	0.917	0.917
2.75	0.922	0.921	0.947	0.959
3.25	0.945	0.951	0.966	0.941
3.75	0.971	0.949	0.988	0.956
4.25	0.969	0.982	0.983	0.961
4.75	0.998	1.001	0.992	0.957
5.25	1.005	0.987	1.010	0.999
5.75	1.022	0.967	0.991	1.016
6.25	1.004	1.026	1.004	1.010
6.75	1.023	1.026	0.989	0.976
7.25	1.009	1.006	1.003	1.017
7.75	1.003	1.015	0.981	0.986

TABLE V

Molecular Simulation Shock Wave Density Profiles in a Gas with a Lennard-Jones Intermolecular Potential

$$\rho = \frac{\rho - \rho_1}{\rho_2 - \rho_1}$$

X/λ_1	M = 8 T* = 1.20	M = 8 T* = 1.56	M = 8 T* = 2.10	M = 8 T* = 2.56
-7.75	-0.001	0.004	0.006	0.006
-7.25	0.004	0.000	-0.001	0.004
-6.75	0.007	0.009	0.009	0.003
-6.25	0.012	0.008	0.005	0.007
-5.75	0.009	0.019	-0.002	0.008
-5.75	0.016	0.020	0.012	0.015
-4.75	0.029	0.023	0.010	0.020
-4.25	0.025	0.038	0.021	0.021
-3.75	0.040	0.046	0.028	0.044
-3.25	0.052	0.053	0.031	0.037
-2.75	0.079	0.081	0.063	0.077
-2.25	0.107	0.105	0.092	0.097
-1.75	0.167	0.167	0.132	0.135
-1.25	0.222	0.221	0.197	0.173
-0.75	0.301	0.313	0.281	0.253
-0.25	0.388	0.419	0.388	0.390
0.25	0.471	0.524	0.500	0.518
0.75	0.592	0.638	0.629	0.651
1.25	0.729	0.714	0.750	0.749
1.75	0.818	0.799	0.835	0.888
2.25	0.875	0.883	0.925	0.936
2.75	0.923	0.911	0.936	0.926
3.25	0.960	0.948	0.965	0.969
3.75	0.982	0.971	1.013	0.993
4.25	0.977	0.996	1.010	0.983
4.75	0.988	0.974	1.009	1.011
5.25	0.968	0.986	0.995	0.983
5.75	1.023	1.004	1.007	1.009
6.25	1.066	0.979	1.029	1.003
6.75	1.056	0.979	1.010	0.994
7.25	1.018	0.969	1.018	1.010
7.75	1.004	0.991	1.016	1.034

TABLE VI

Modified Run Conditions for Memory Effect Shots

Run#	Soaking		Pumping		Firing
	p_1 (μ Hg of He)	Time (hrs.)	Time	p_o (μ Hg)	Delay (min.)
3351	0	18	--	0.1	20
3352	50	2	35 min.	0.08	20
3353	1000	18	30 min.	0.08	20
3354	1000	18	5 min.	0.2	13
3355	0	0	4 hrs.	0.02	15

p_1 is the pressure in the shock tube during the soaking.

p_o is the ultimate pressure attained after soaking and prior to firing.

The Firing Delay is the time between turning off the pumps at the ultimate pressure and firing the shock tube.

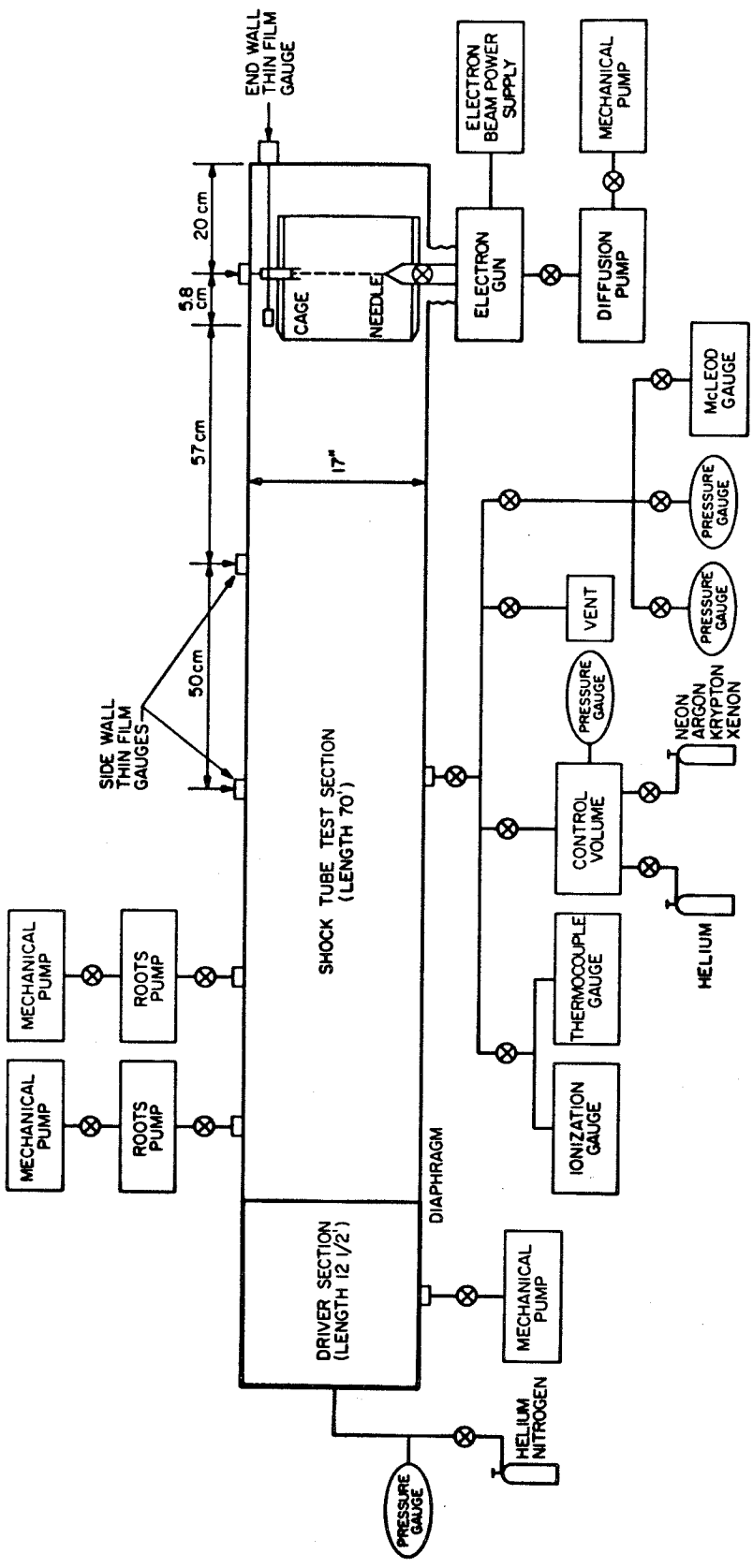

Figure 1. Schematic Diagram of the Experimental Apparatus

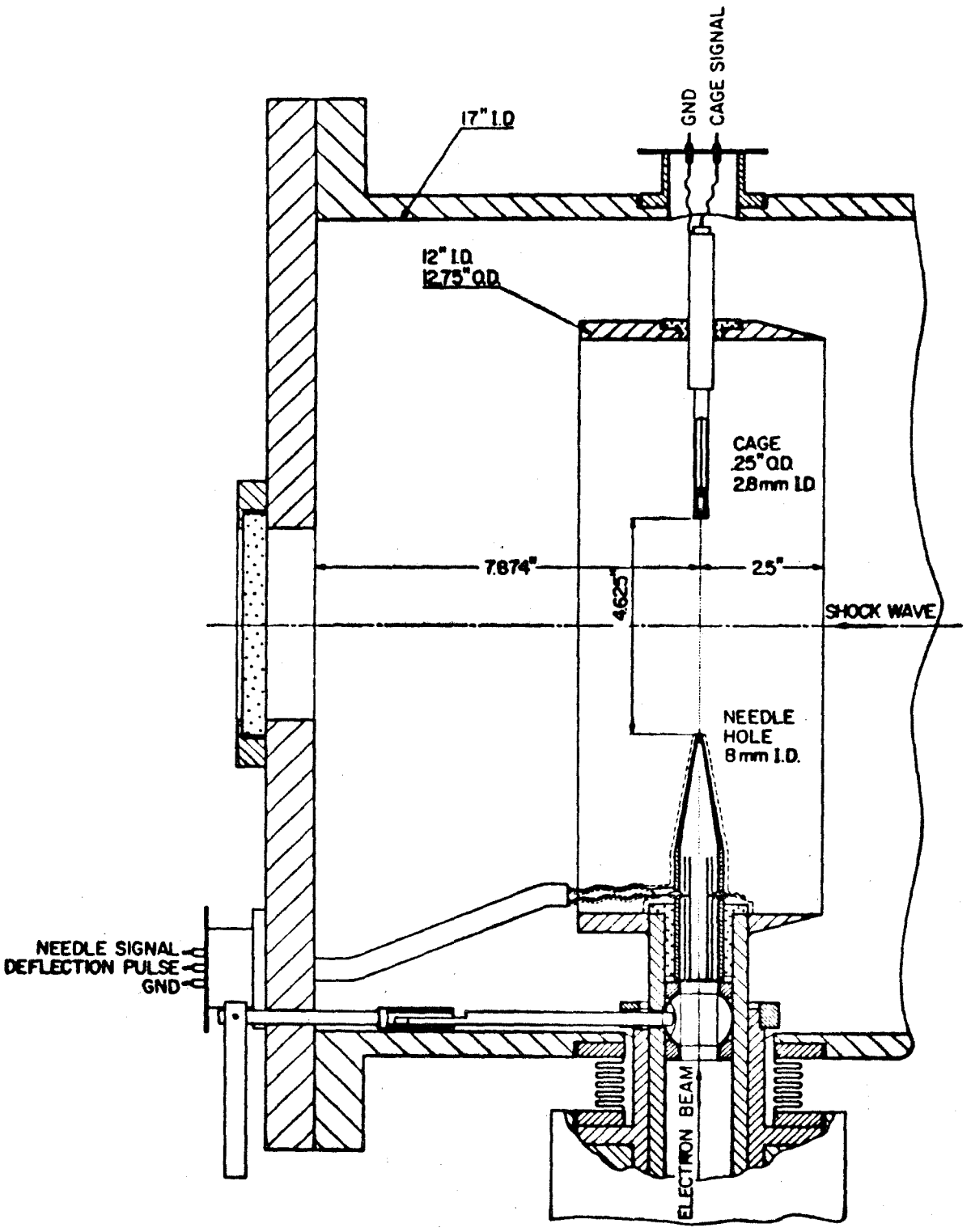

Figure 2. Diagram of Electron Beam Densitometer

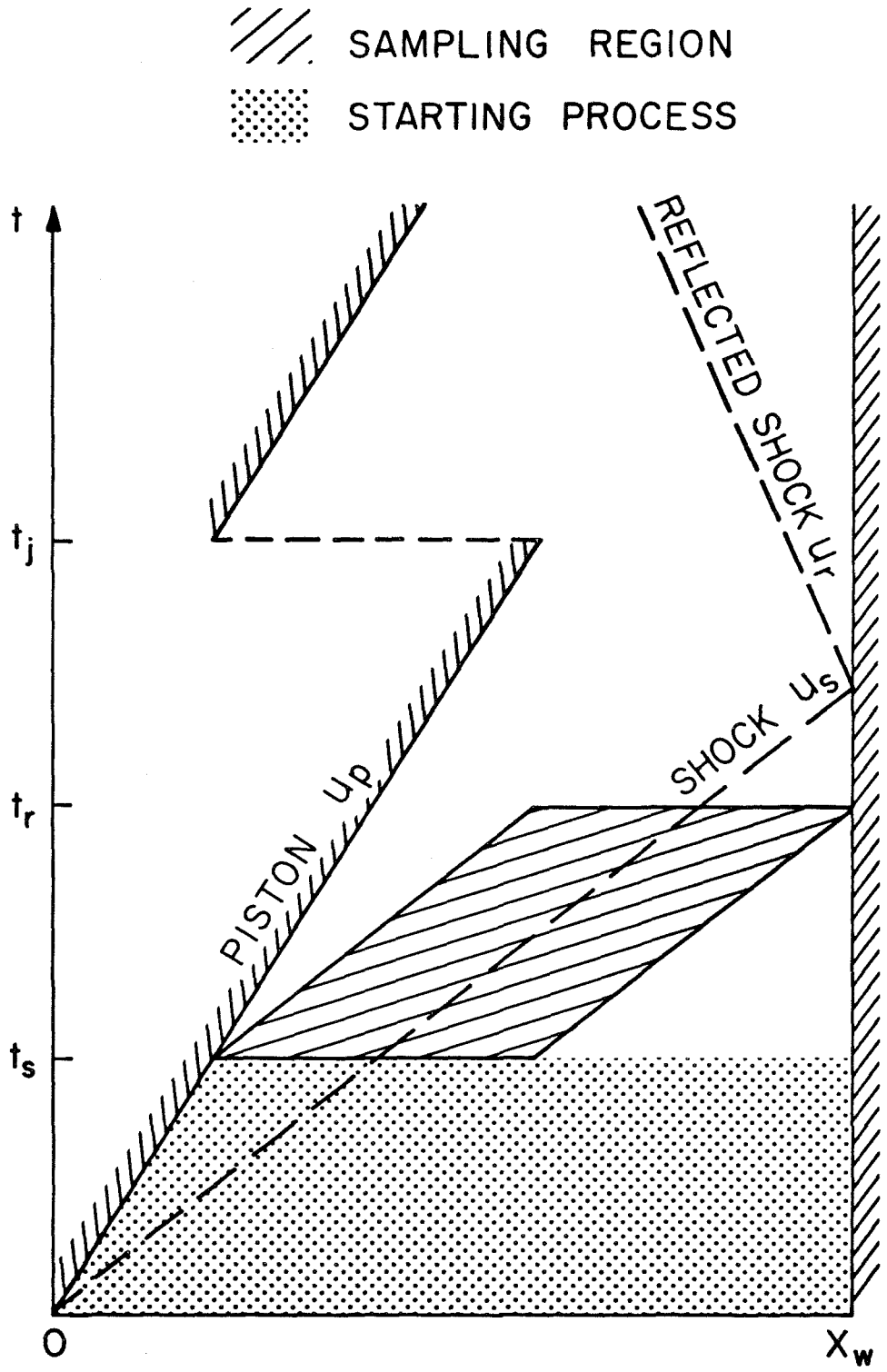

Figure 3. An x-t Diagram of the Piston Problem in Stationary Coordinates

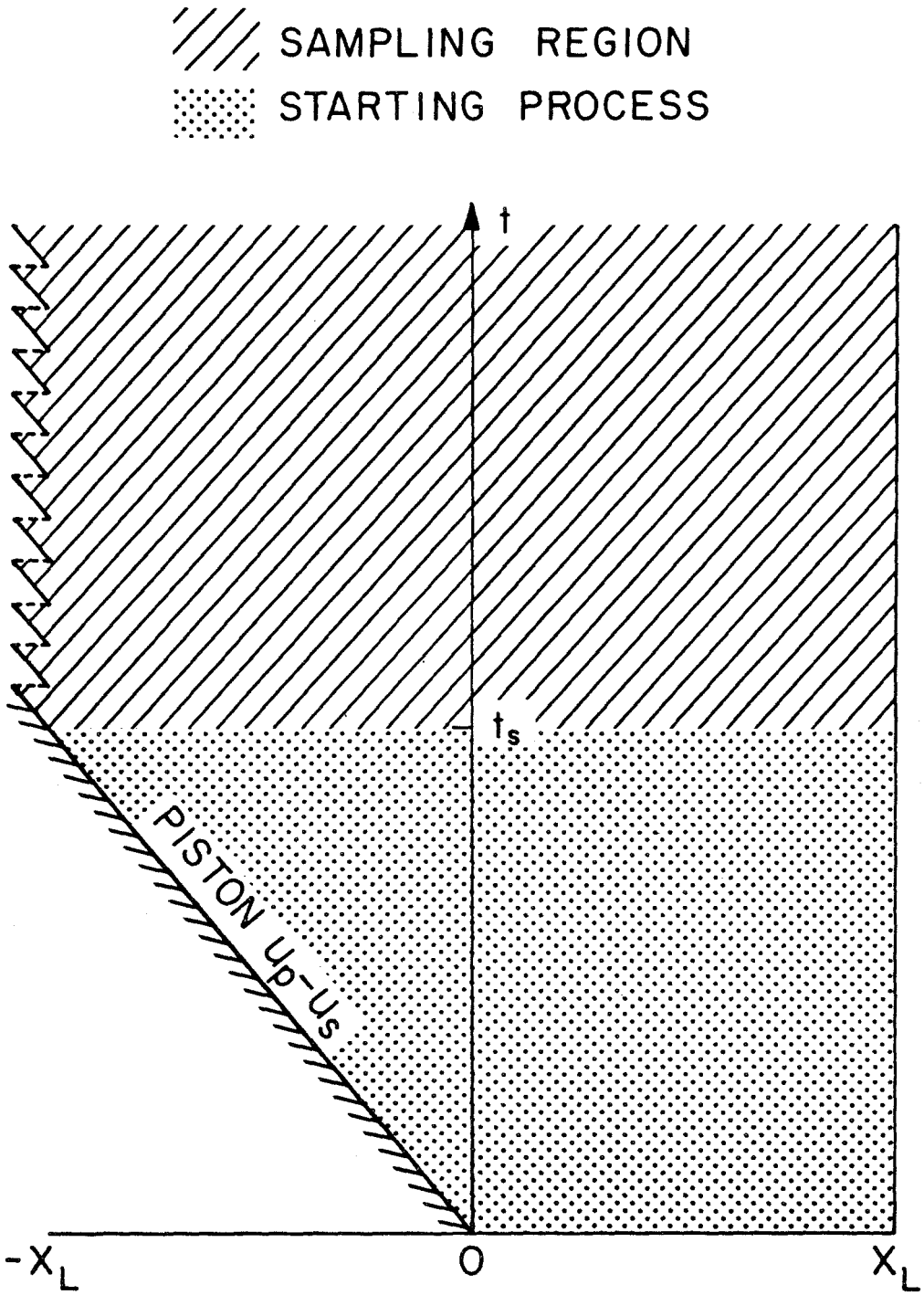

Figure 4. An x-t Diagram of the Piston Problem in Shock Fixed Coordinates

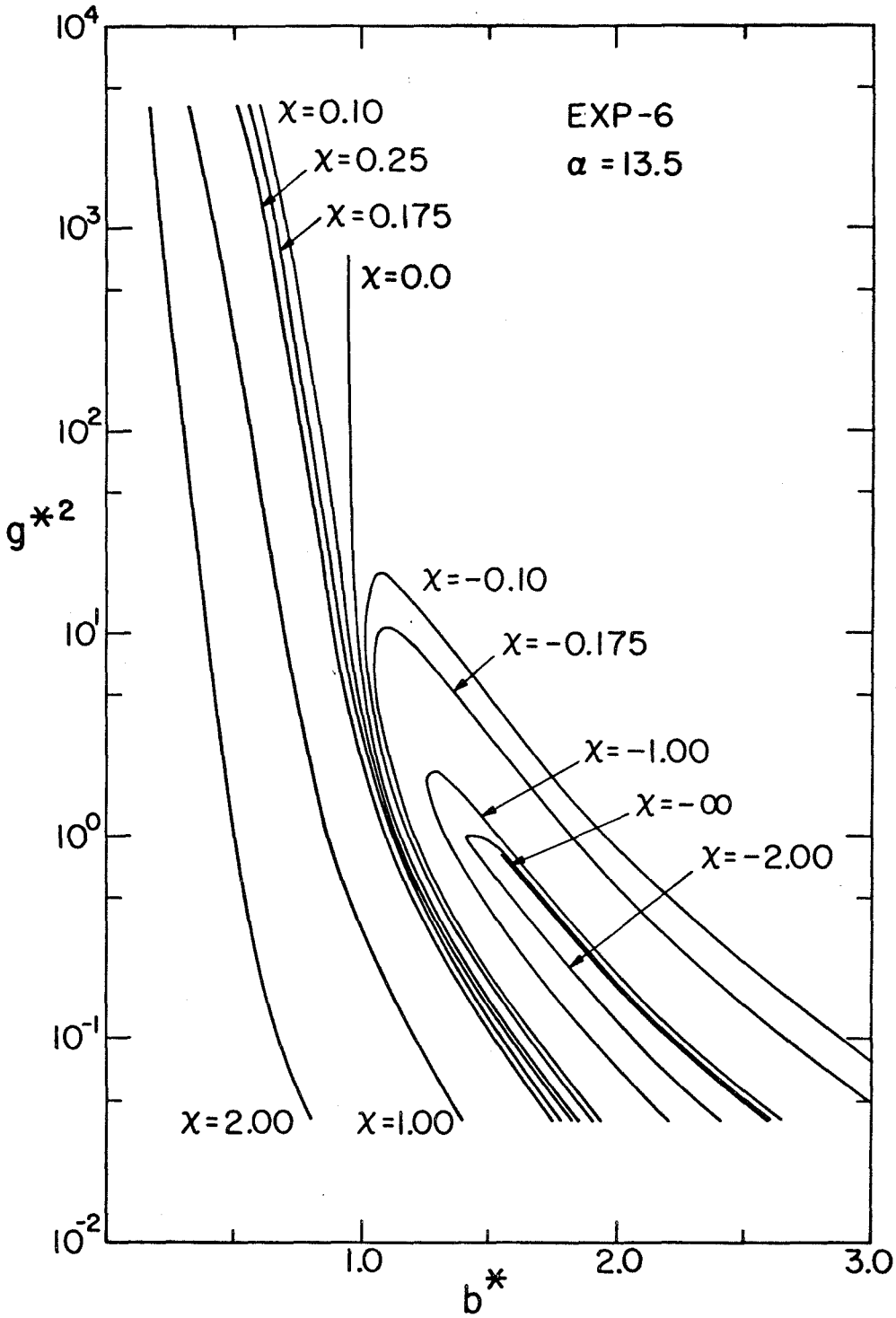

Figure 5. Angle of Deflection, χ , for Collisions as a Function of g^{*2} and b^*

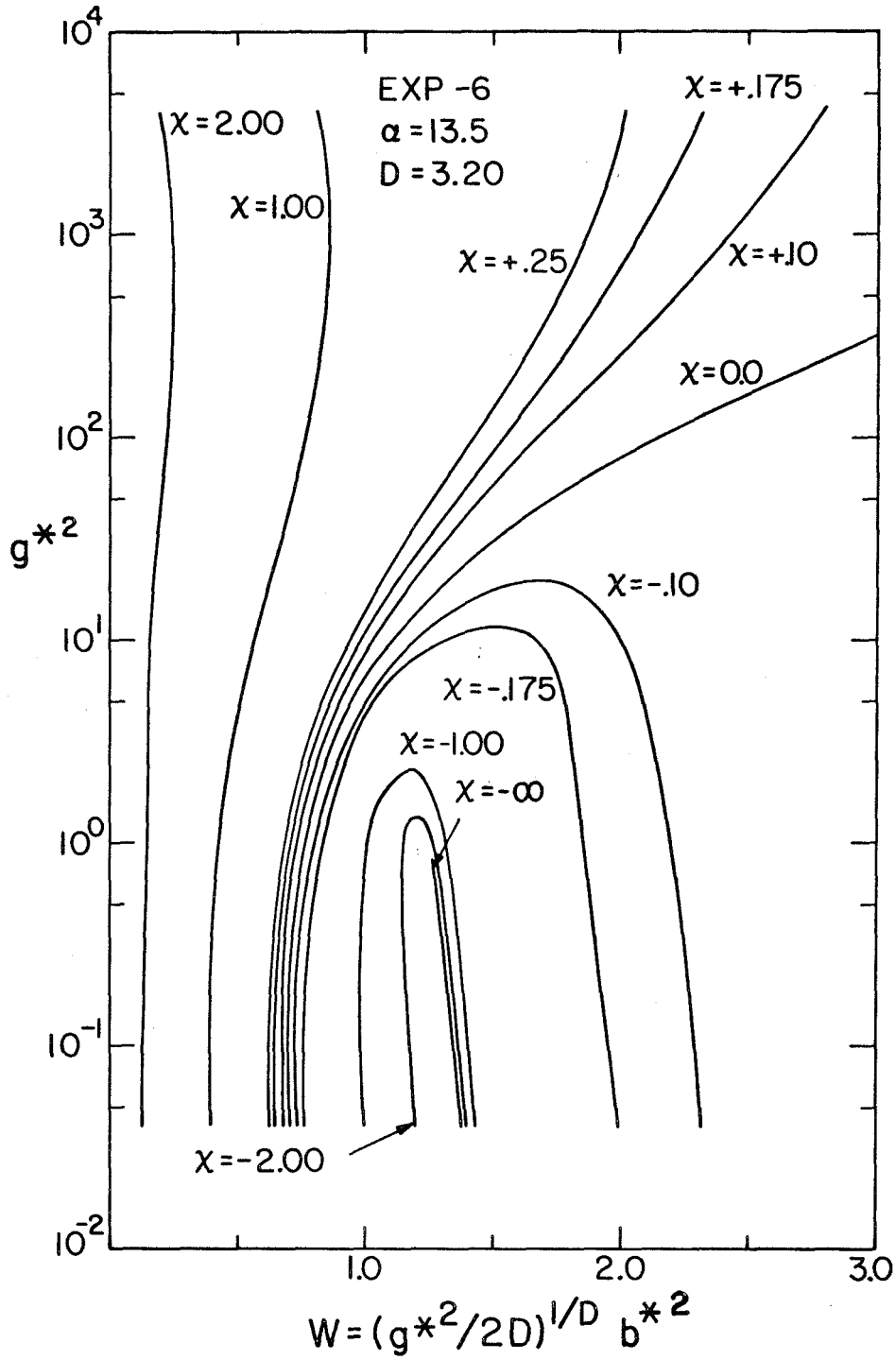

Figure 6. Angle of Deflection, χ , for Collisions as a Function of g^{*2} and W

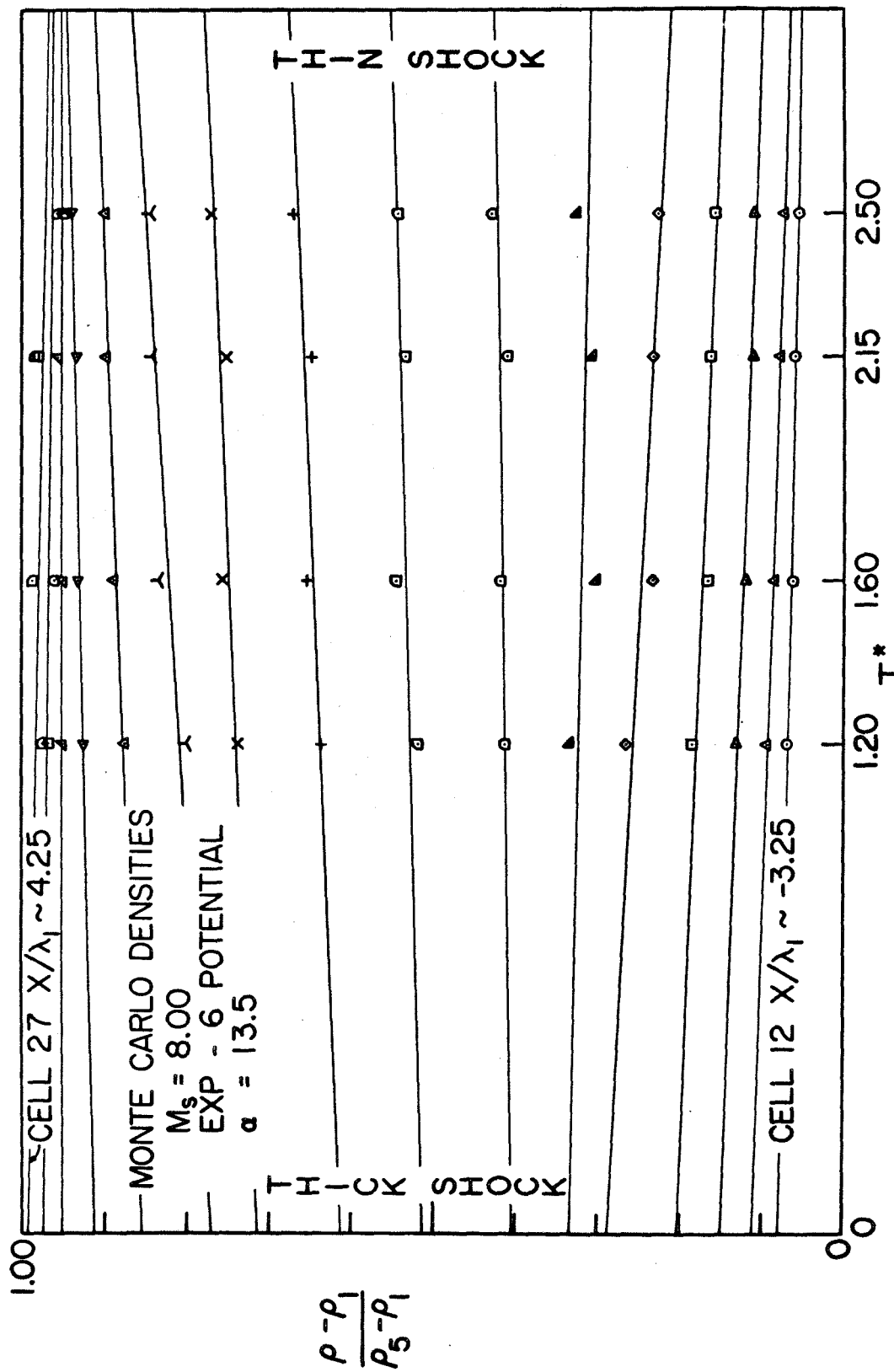

Figure 7. Least Squares Smoothing Procedure for the Monte Carlo Density Profiles

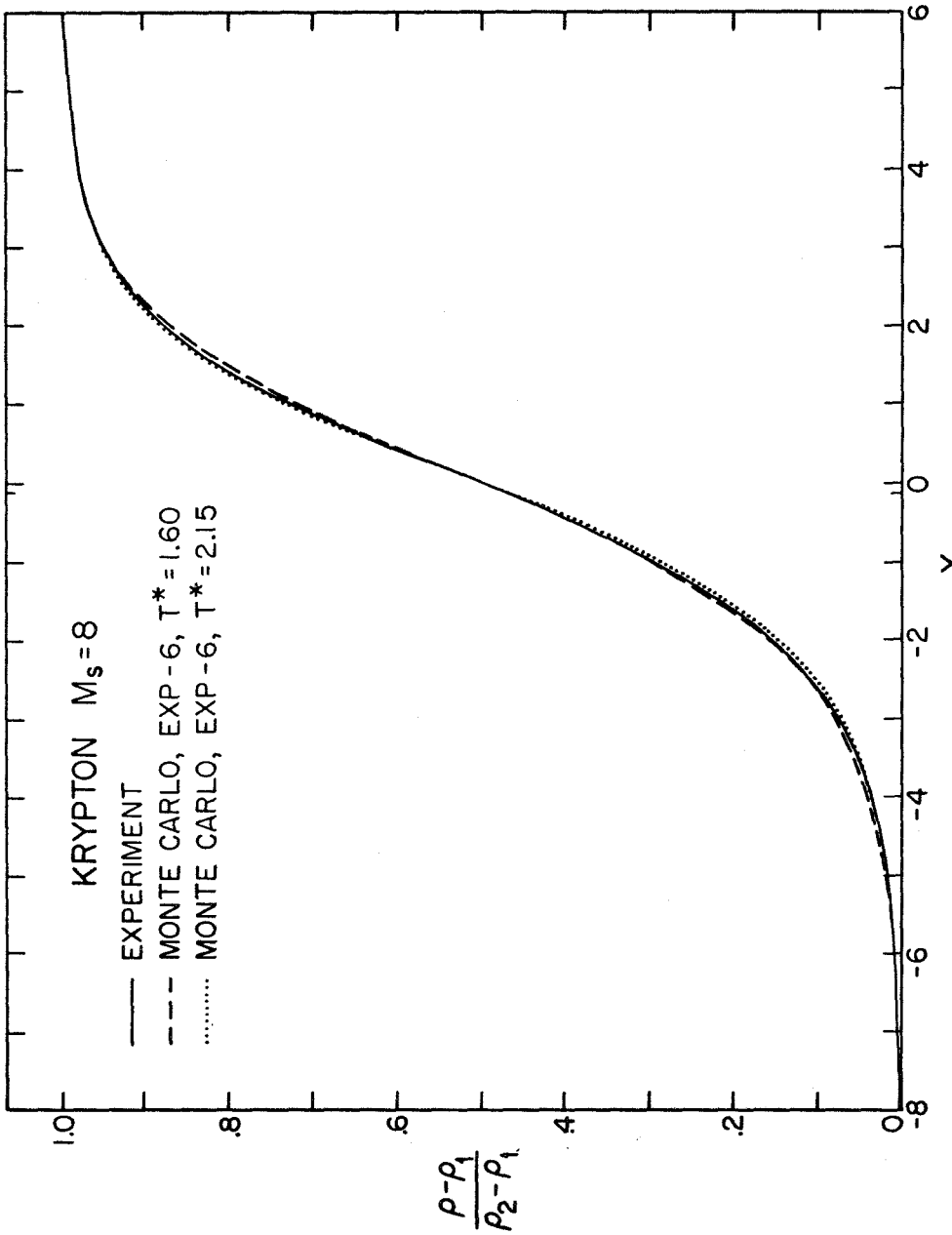

Figure 8. Comparison of Experimental and Smoothed Monte Carlo Density Profiles

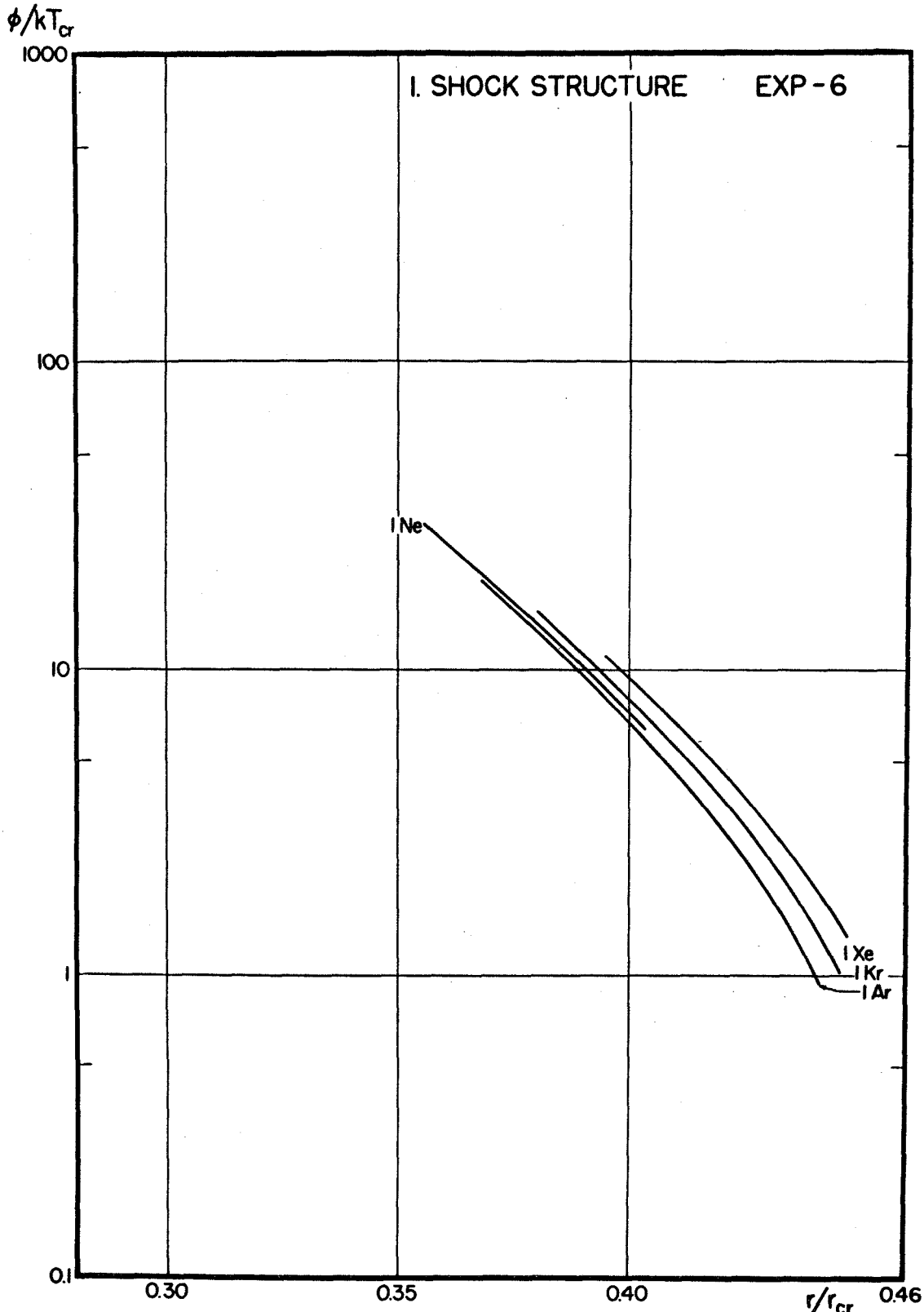

Figure 9. Corresponding States Plot of Exp-6 Shock Structure Potentials

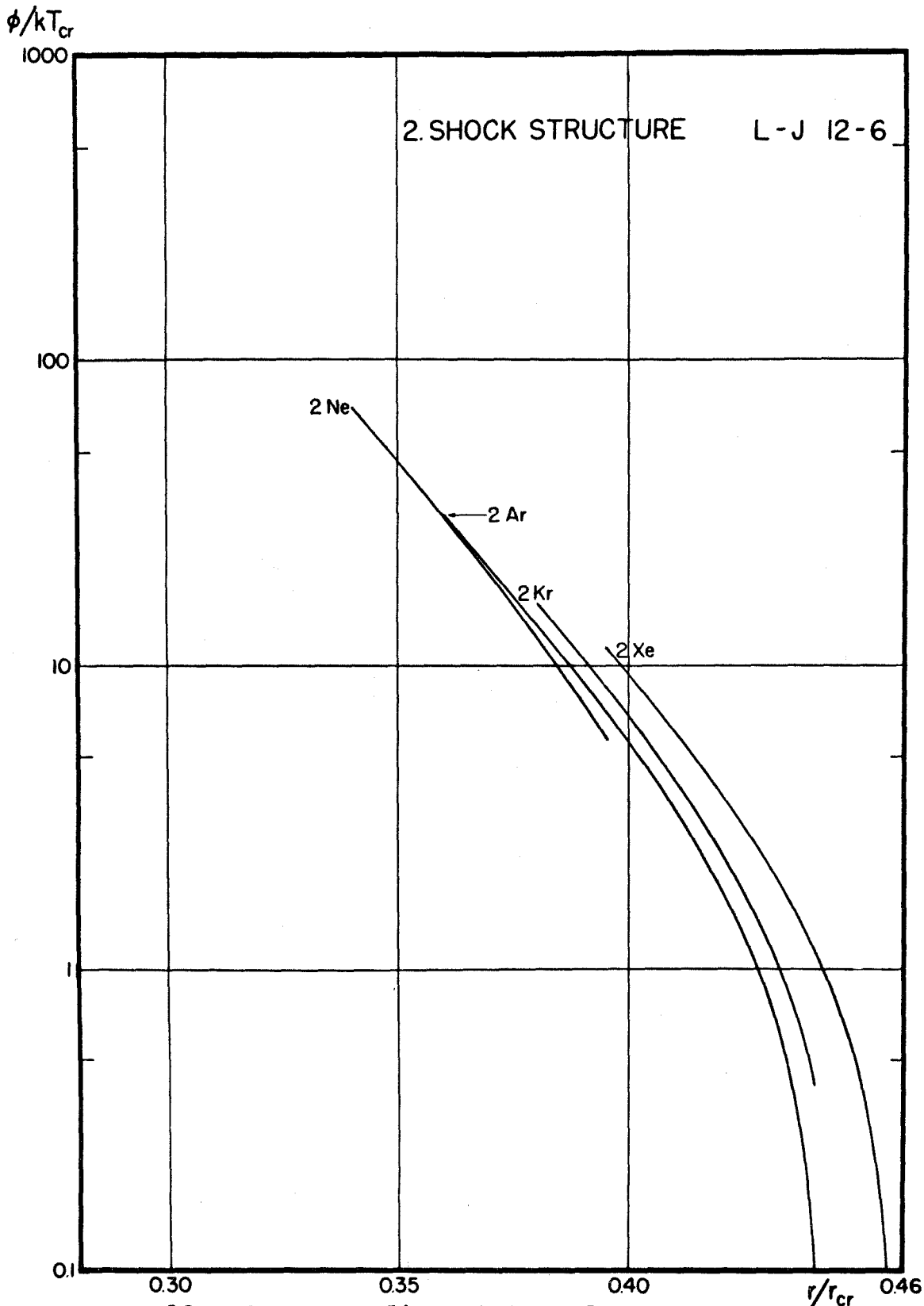

Figure 10. Corresponding States Plot of Lennard-Jones Shock Structure Potentials

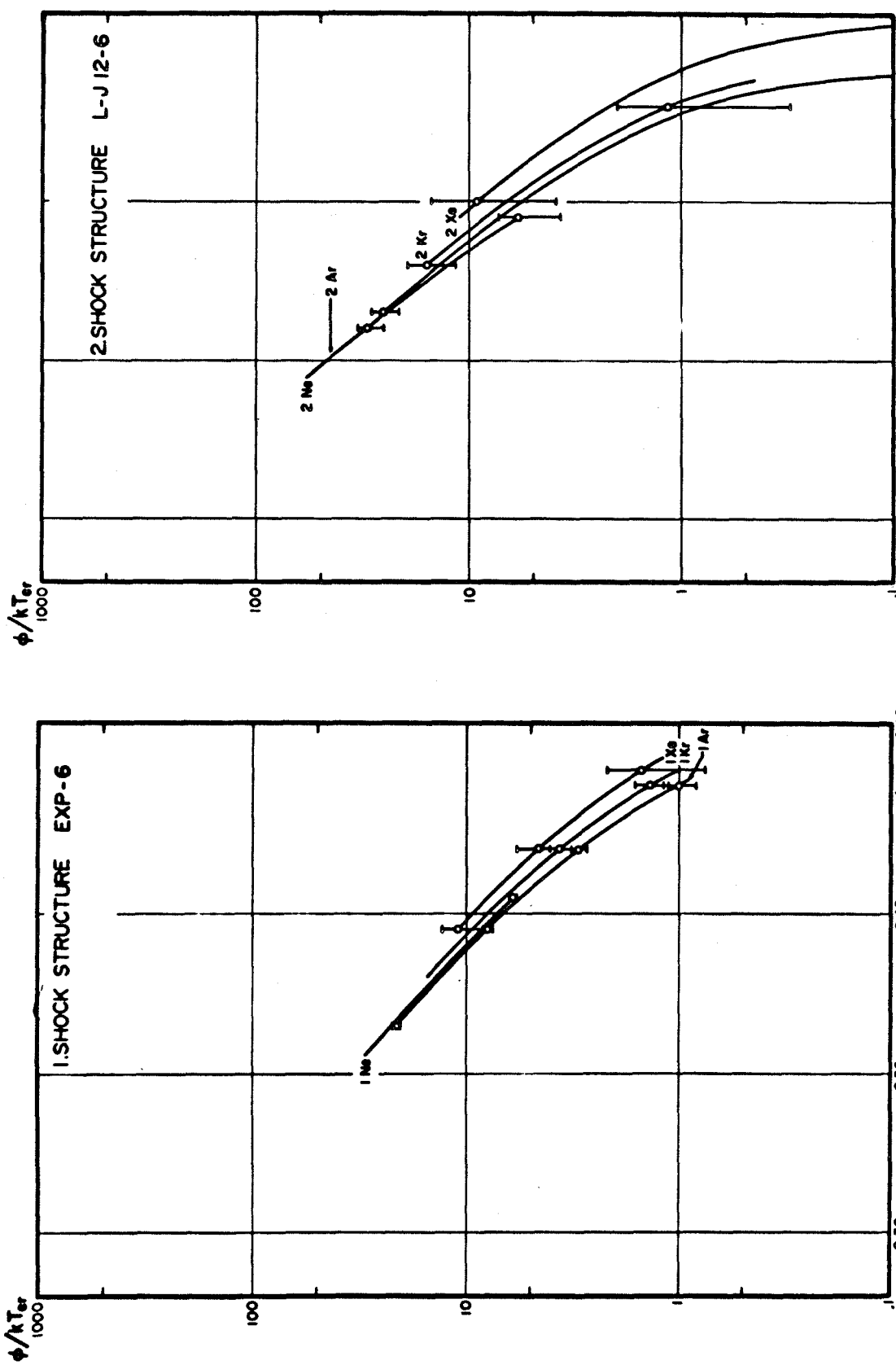

Figure 11. Corresponding States Plots of Shock Structure Potentials with Error Bars: (a) Exp-6 Potential and (b) Lennard-Jones Potential

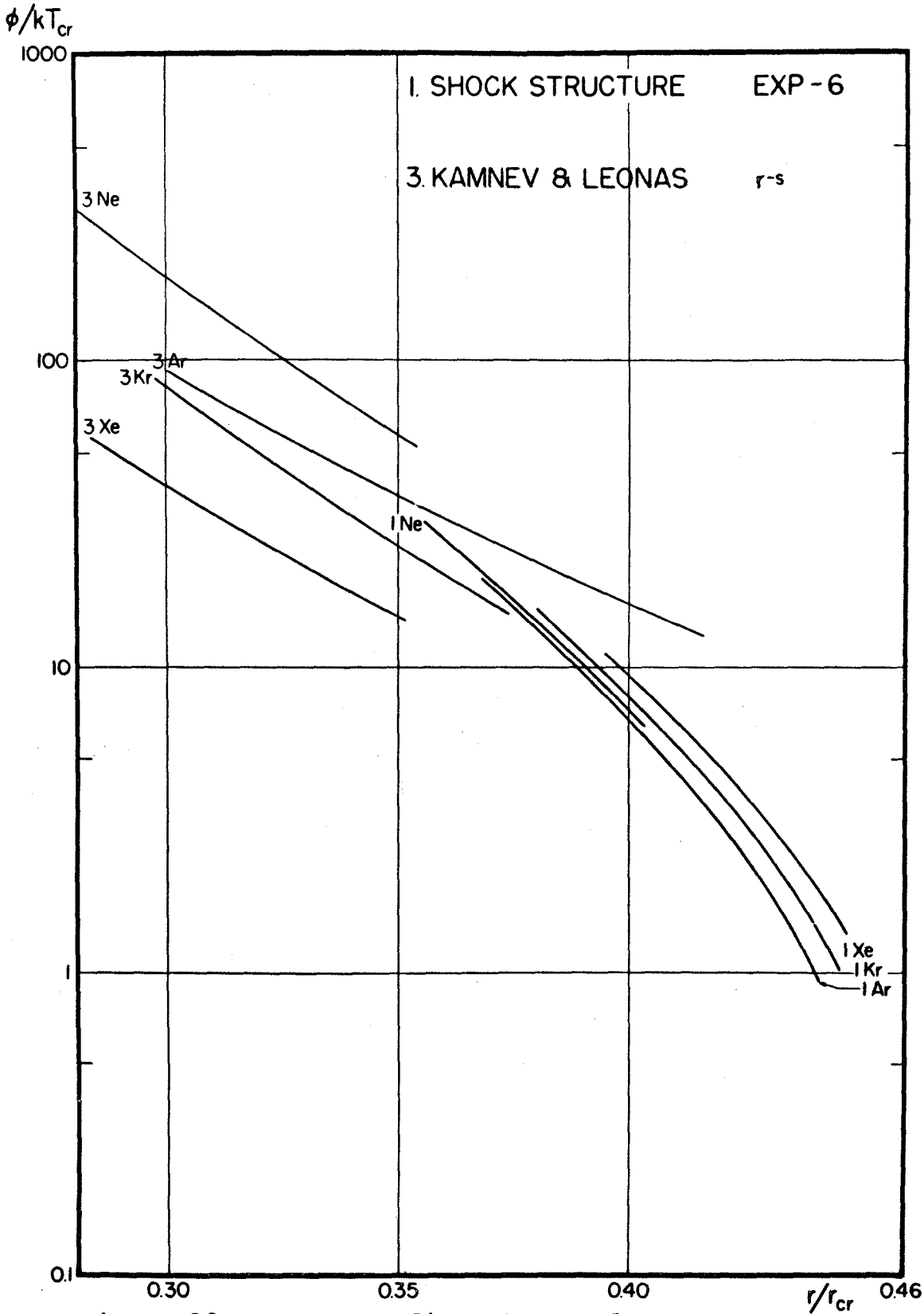

Figure 12. Corresponding States Plot of Potentials Obtained from Molecular Beam Data.[5]

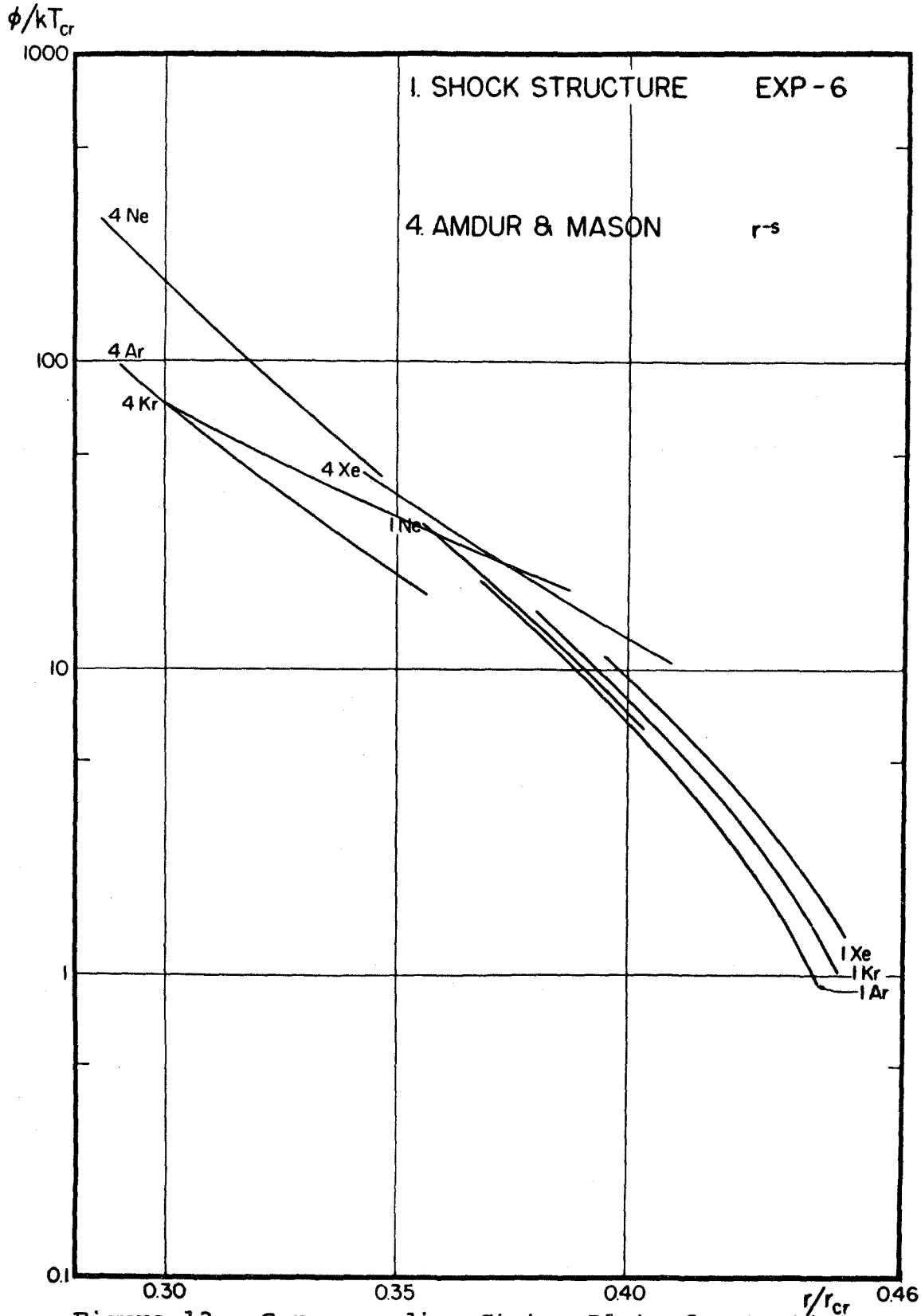

Figure 13. Corresponding States Plot of Potentials Obtained from Molecular Beam Data.[3,4]

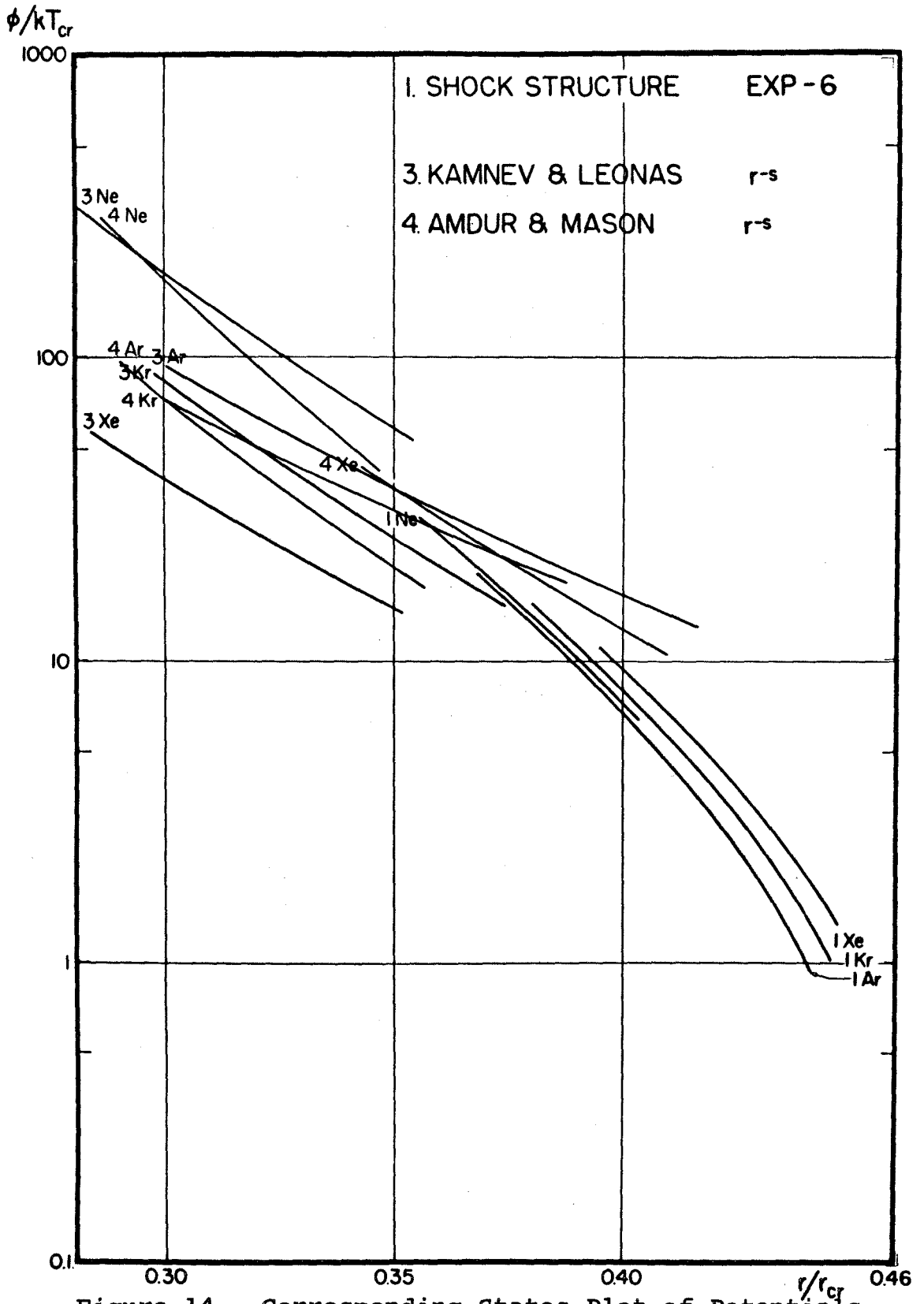

Figure 14. Corresponding States Plot of Potentials Obtained from Molecular Beam Data.[4,5]

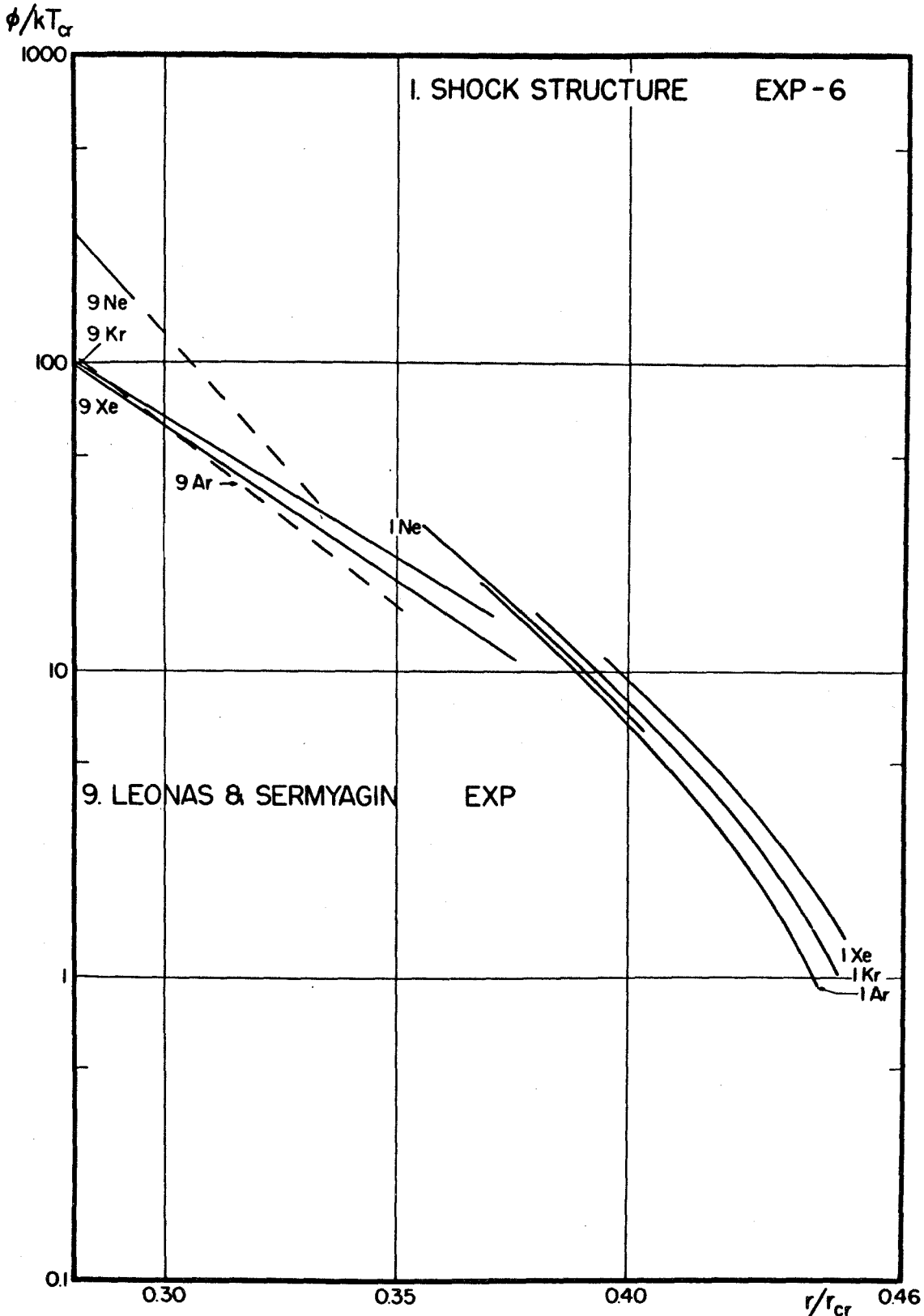

Figure 15. Corresponding States Plot of Potentials Obtained from Molecular Beam Data.[6]

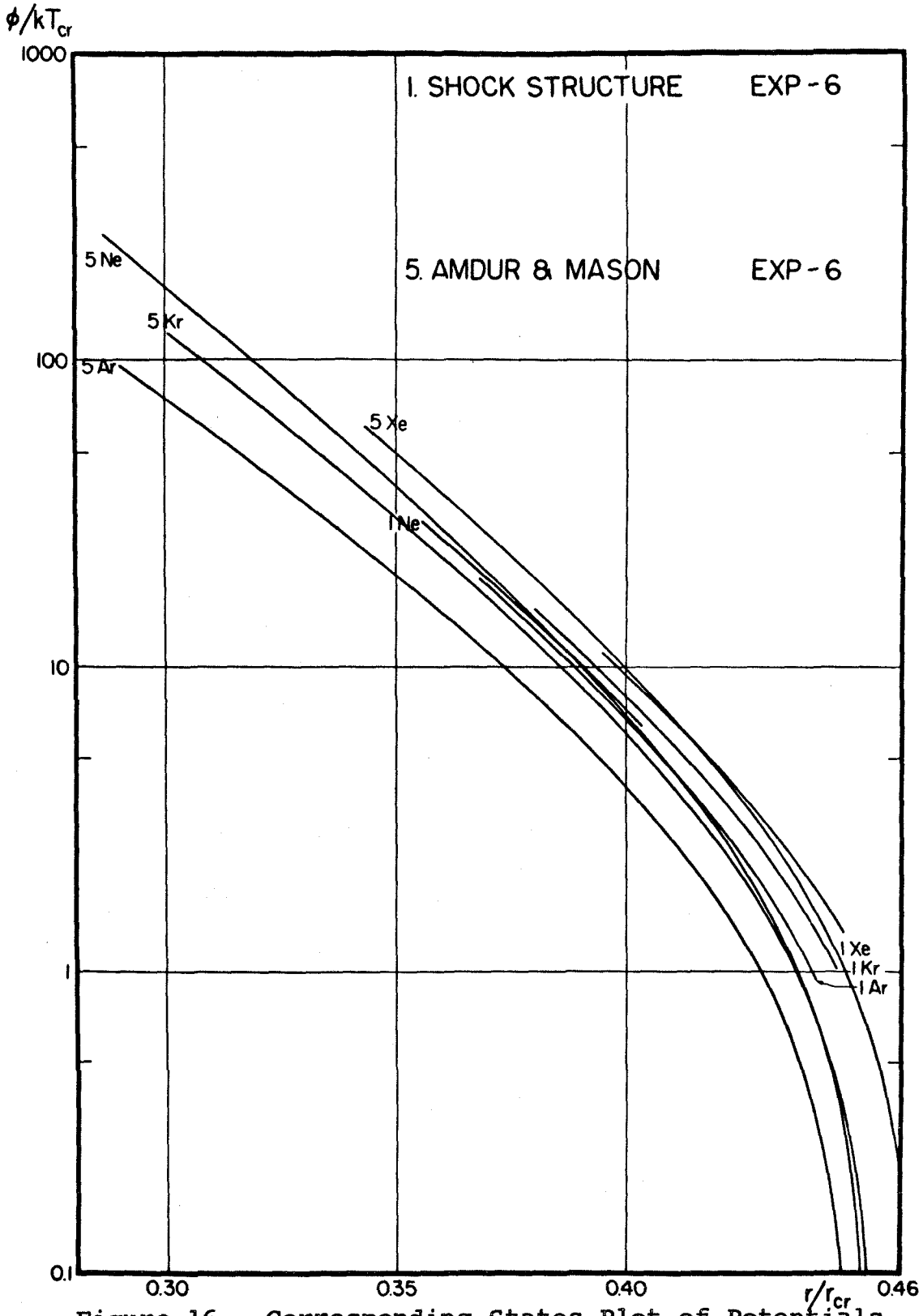

Figure 16. Corresponding States Plot of Potentials Obtained from Several Properties.[34]

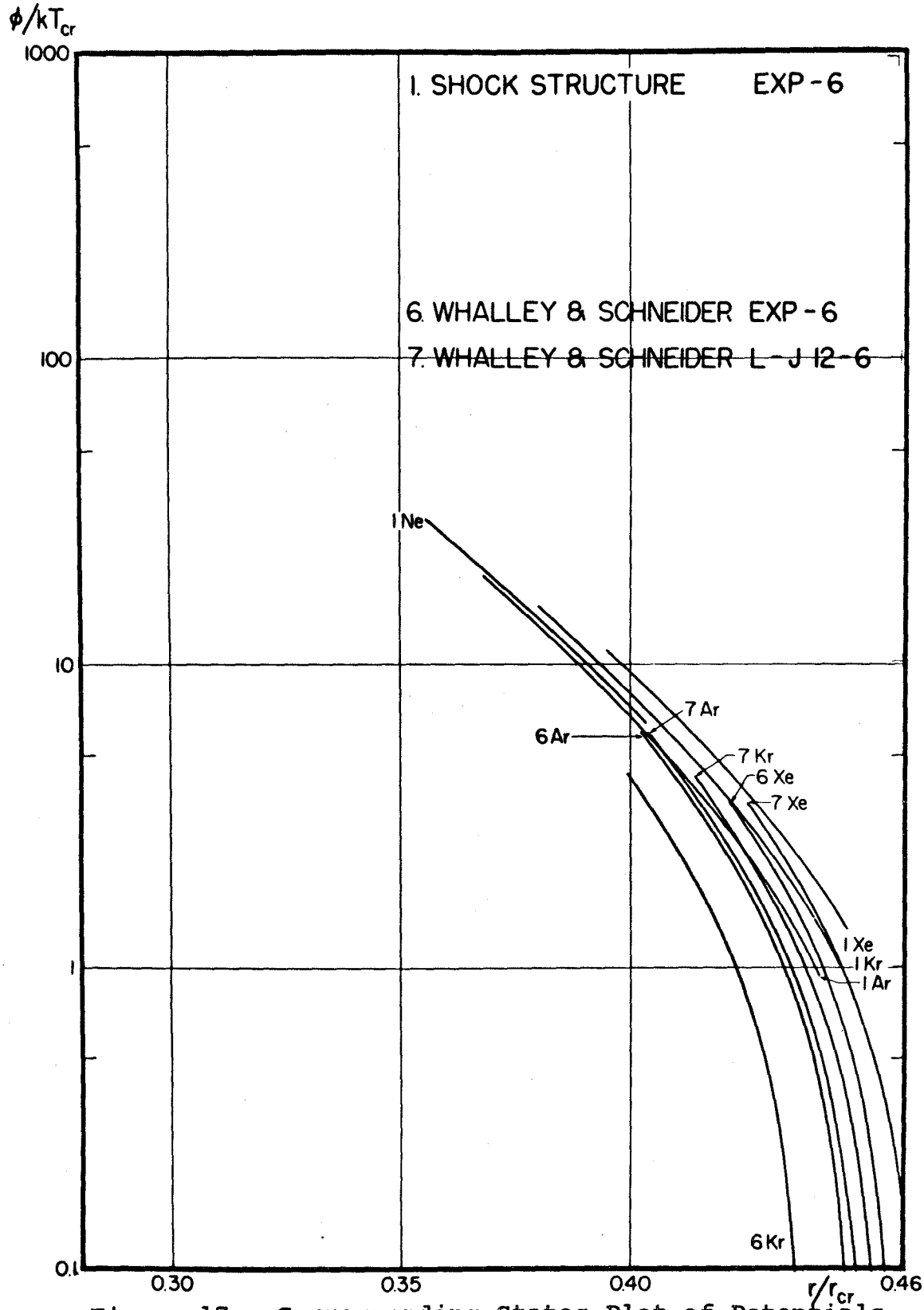

Figure 17. Corresponding States Plot of Potentials Obtained from Second Virial Coefficient Data.[8]

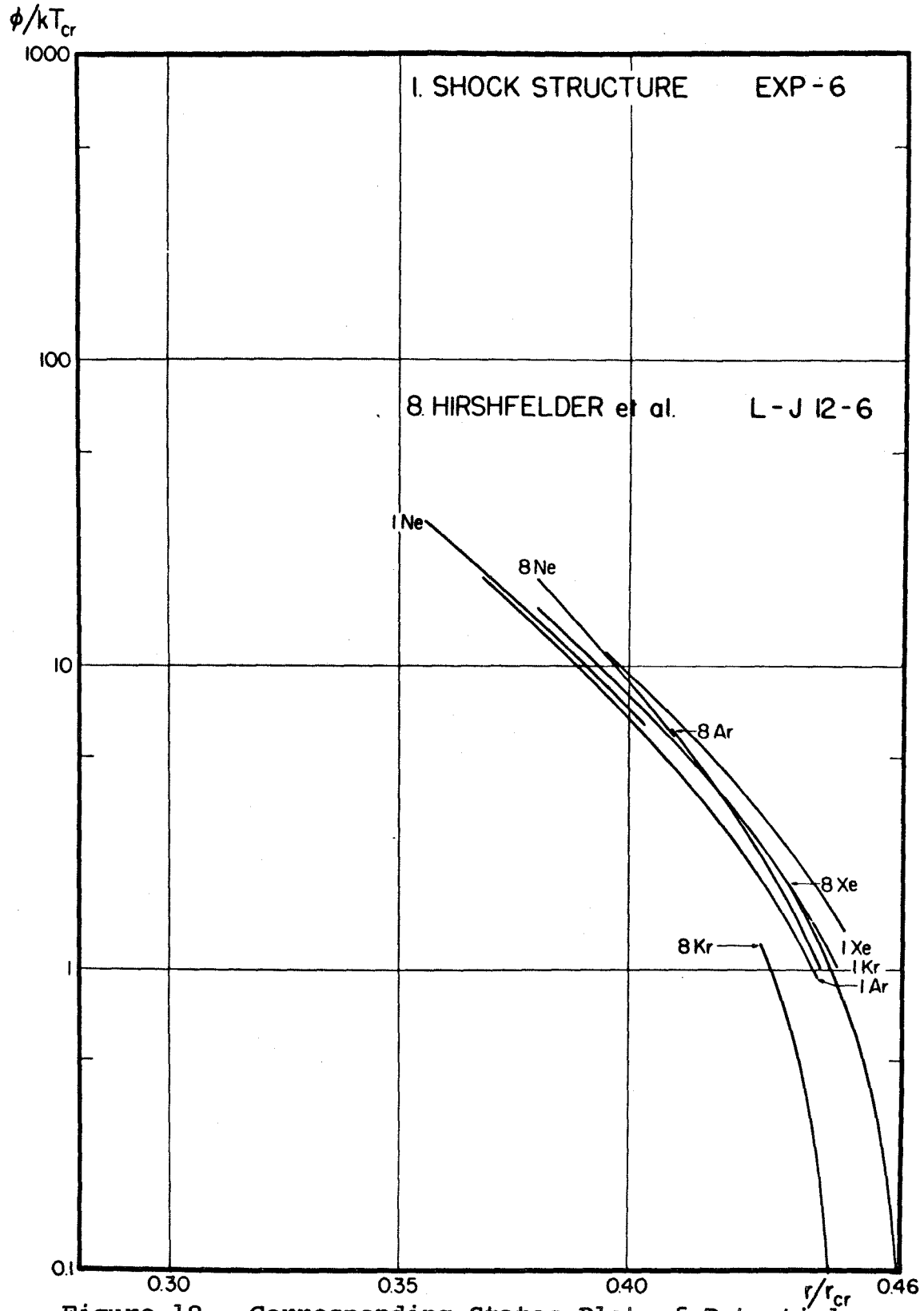

Figure 18. Corresponding States Plot of Potentials Obtained from Viscosity Data.[7]

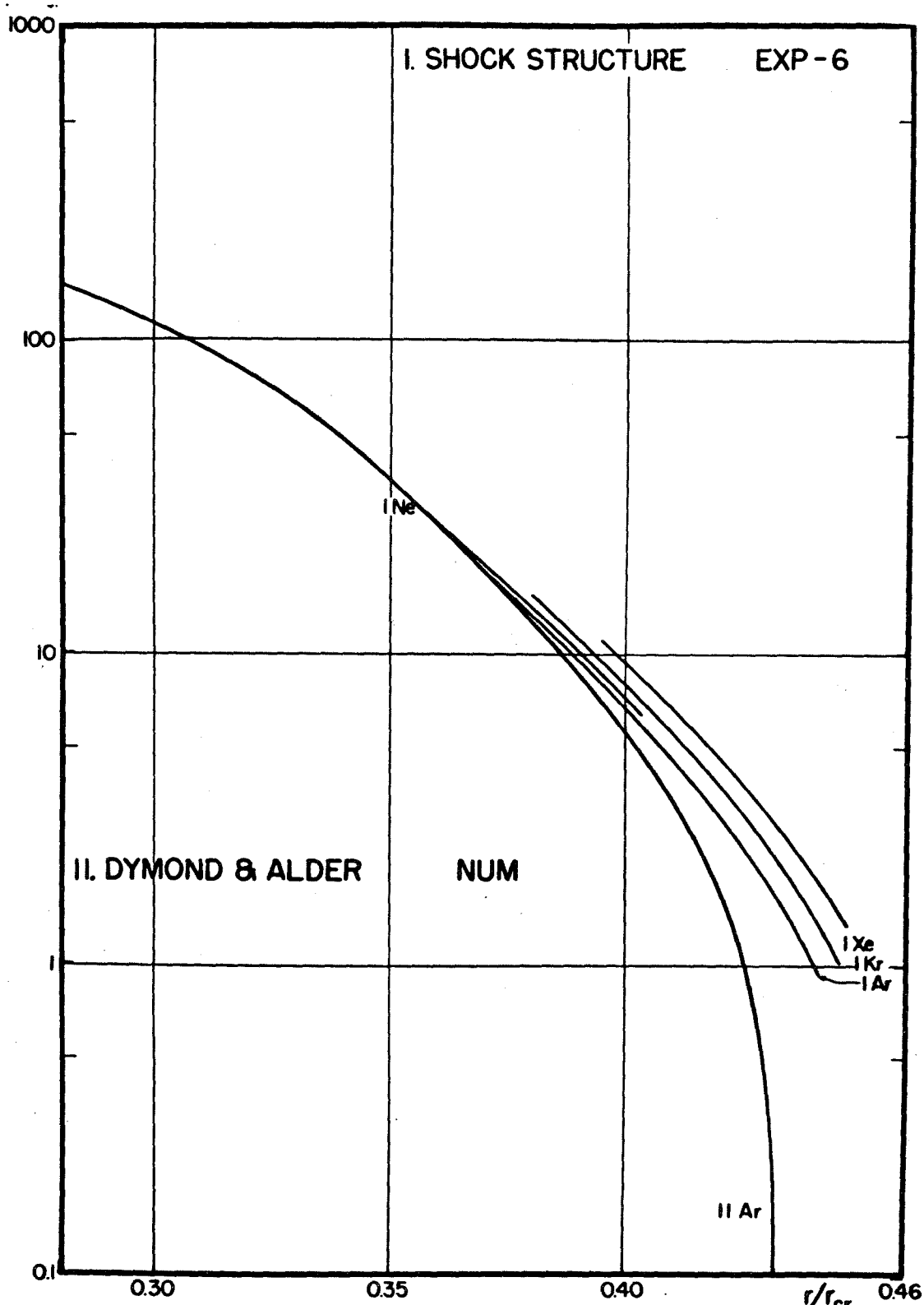

Figure 19. Corresponding States Plot of Potentials Obtained from Several Properties.[2]

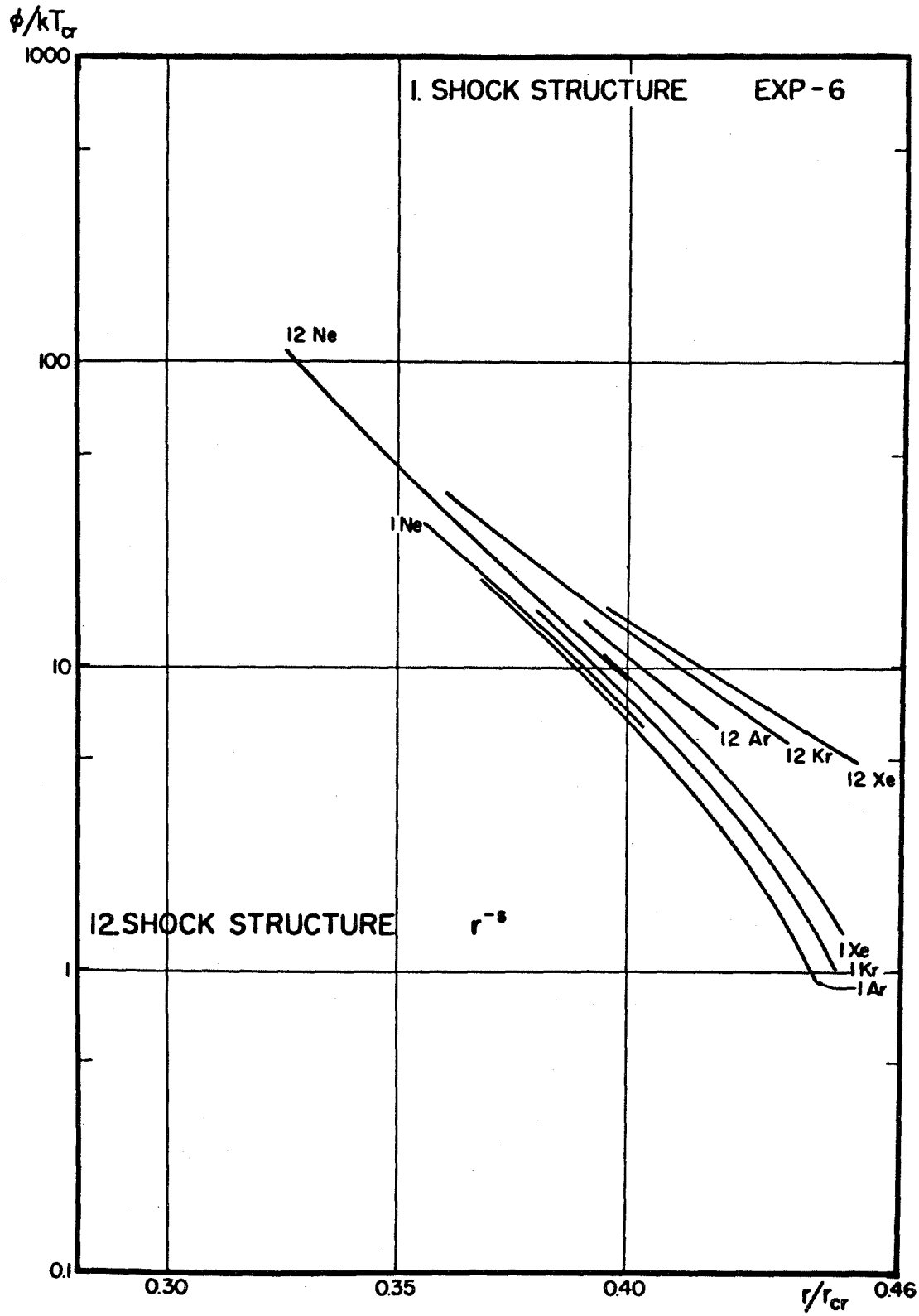

Figure 20. Corresponding States Plot of Simple Repulsive Shock Structure Potentials

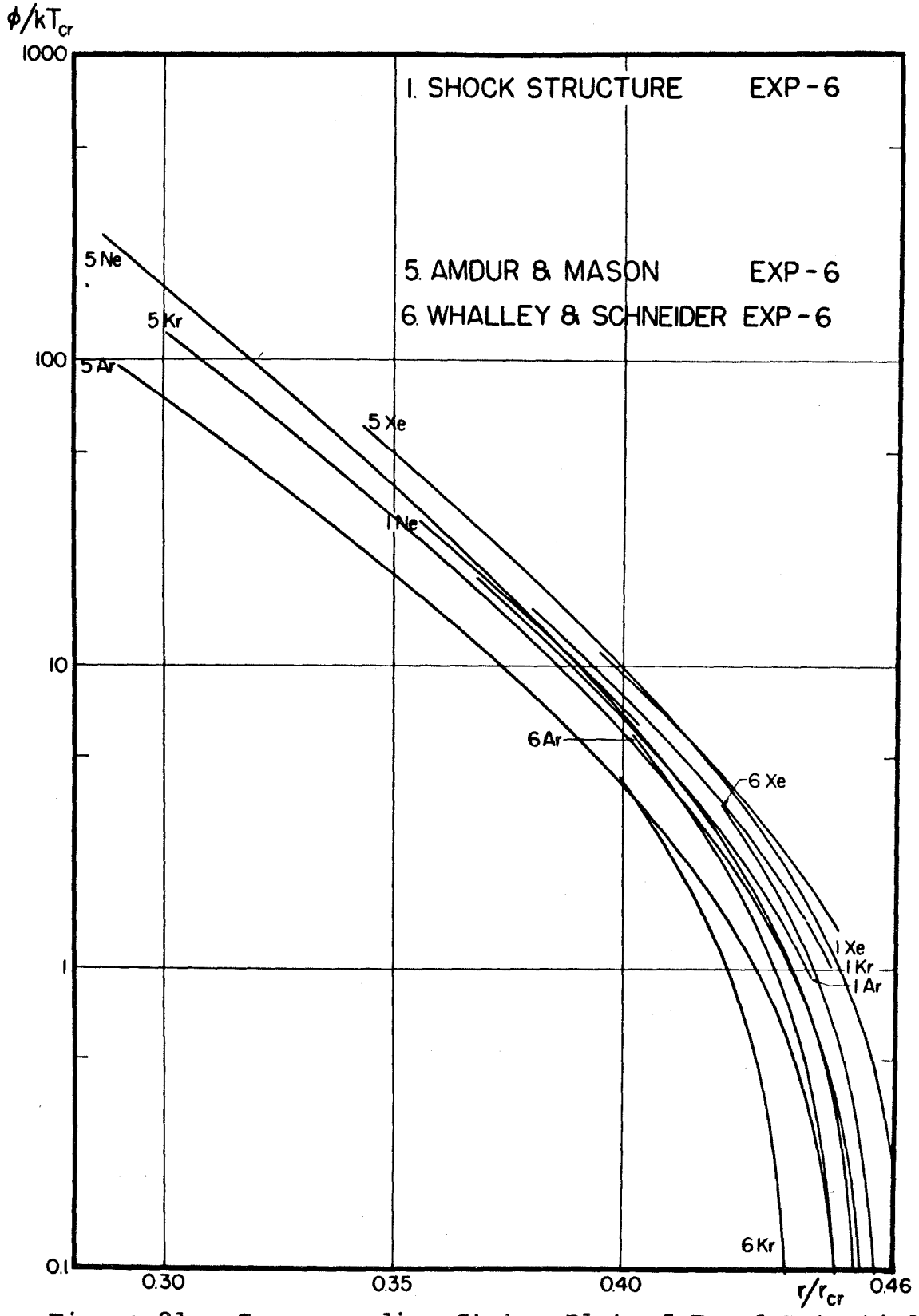

Figure 21. Corresponding States Plot of Exp-6 Potentials

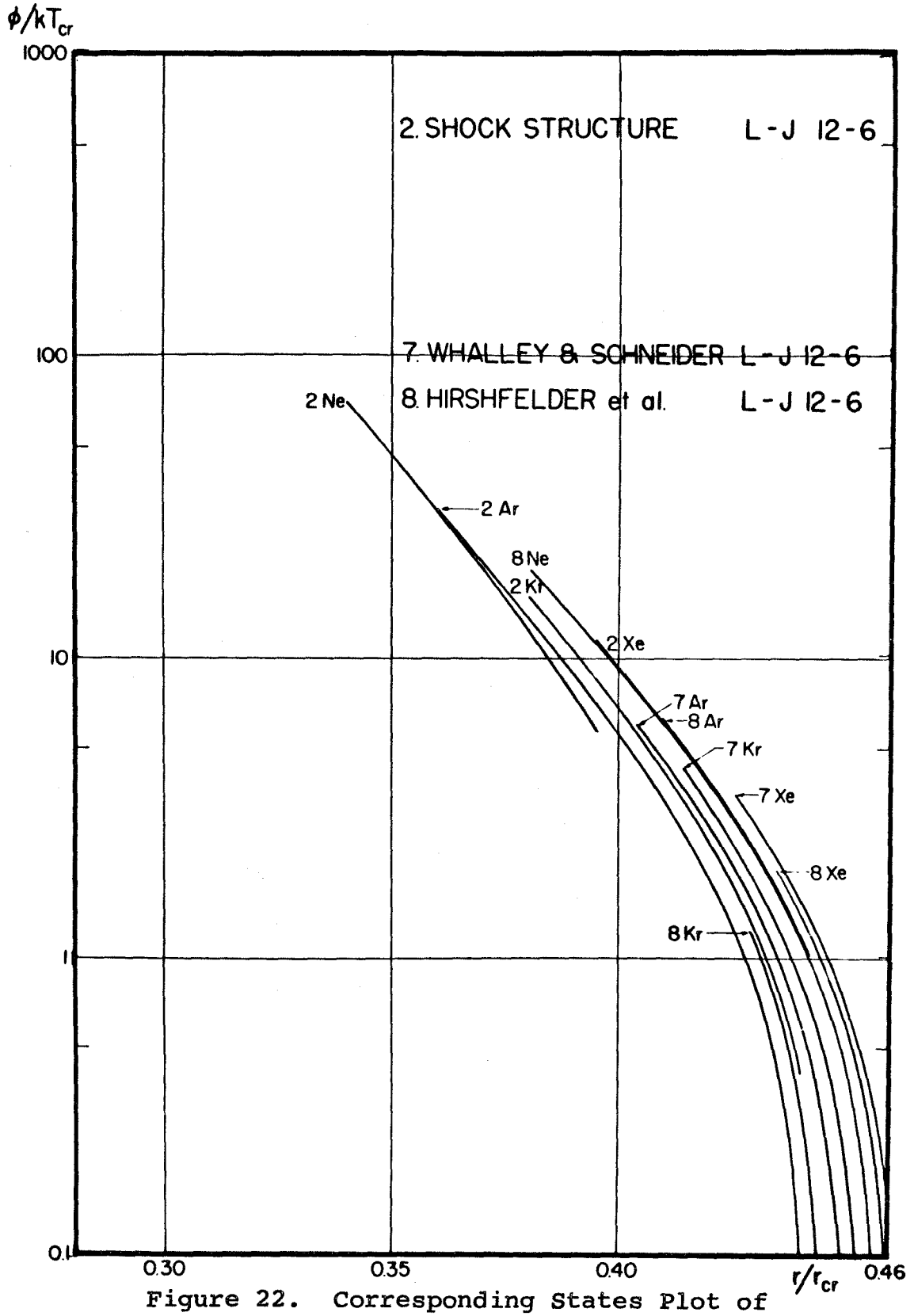

Figure 22. Corresponding States Plot of Lennard-Jones Potentials

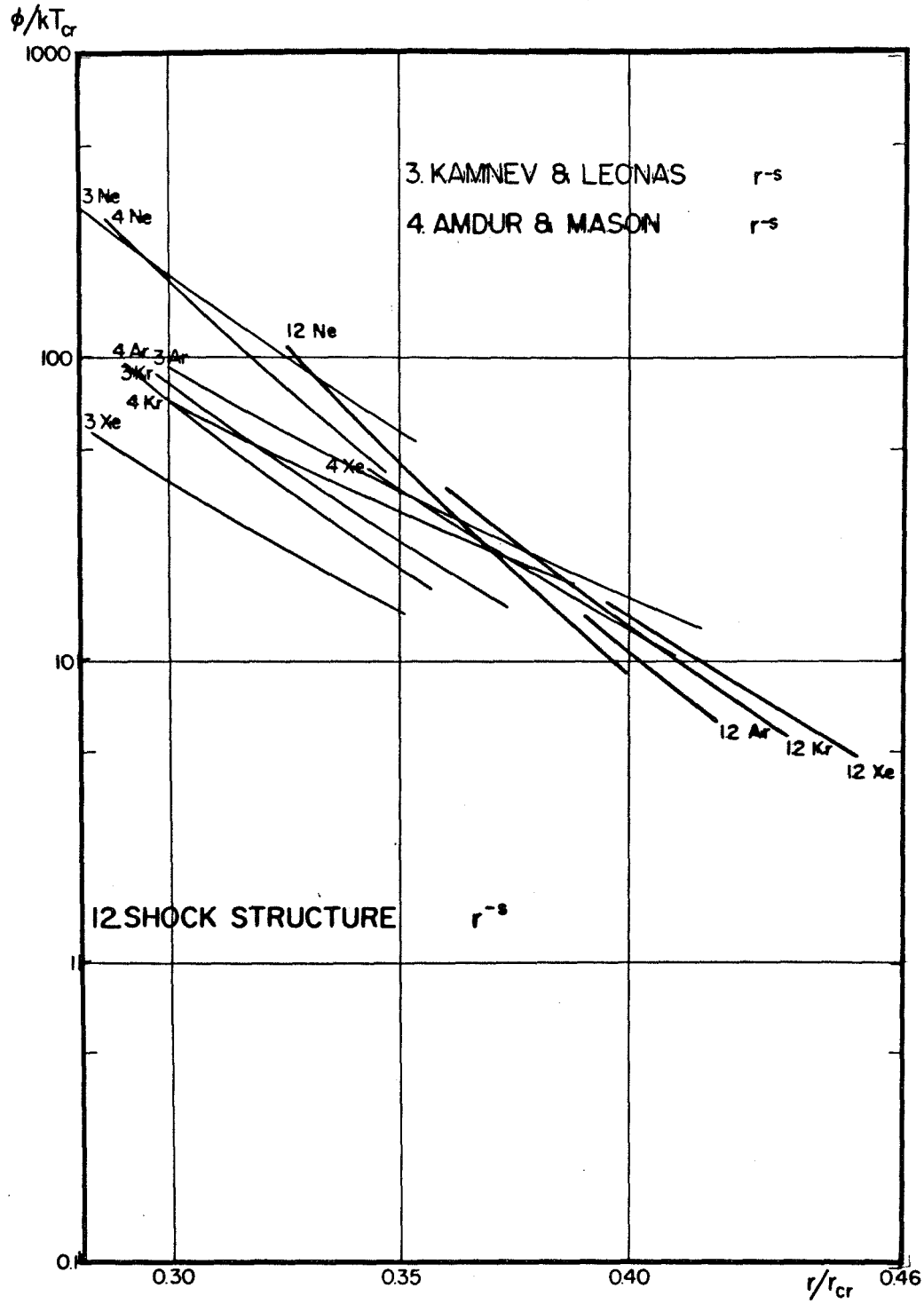

Figure 23. Corresponding States Plot of Simple Repulsive Potentials

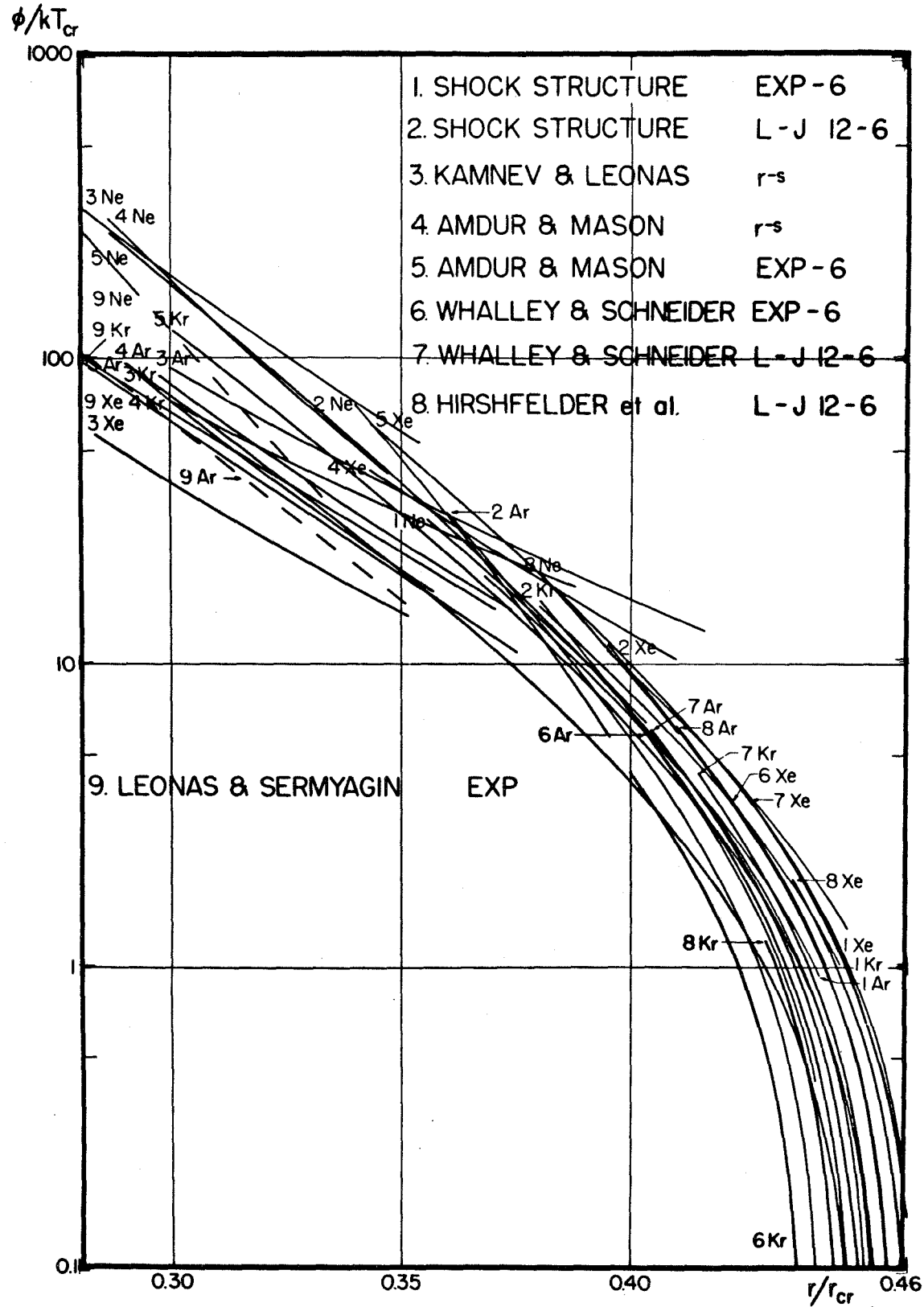

Figure 24. Corresponding States Plot of a Comparison of Different Potentials

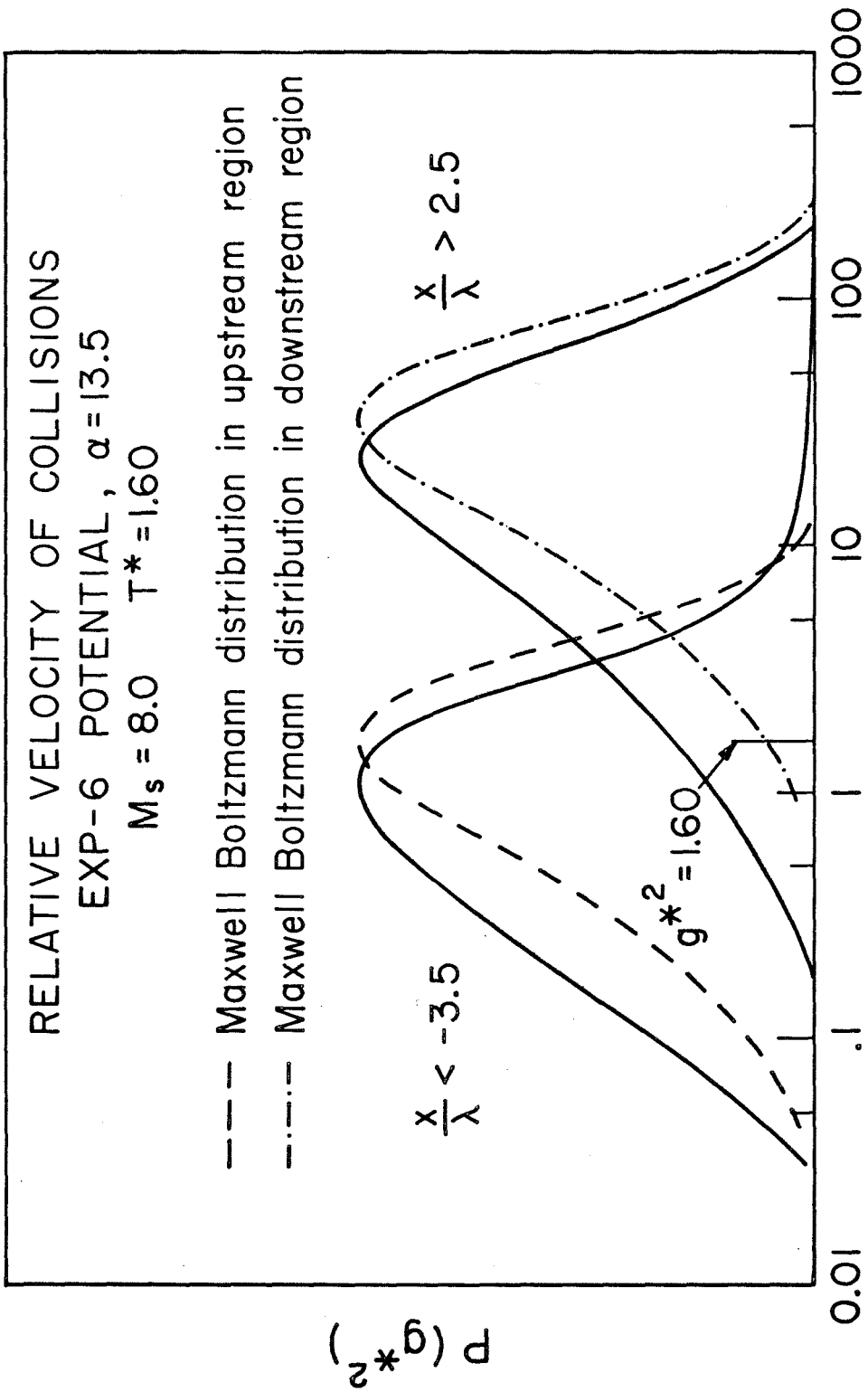

Figure 25. Monte Carlo Calculation Velocity Histogram

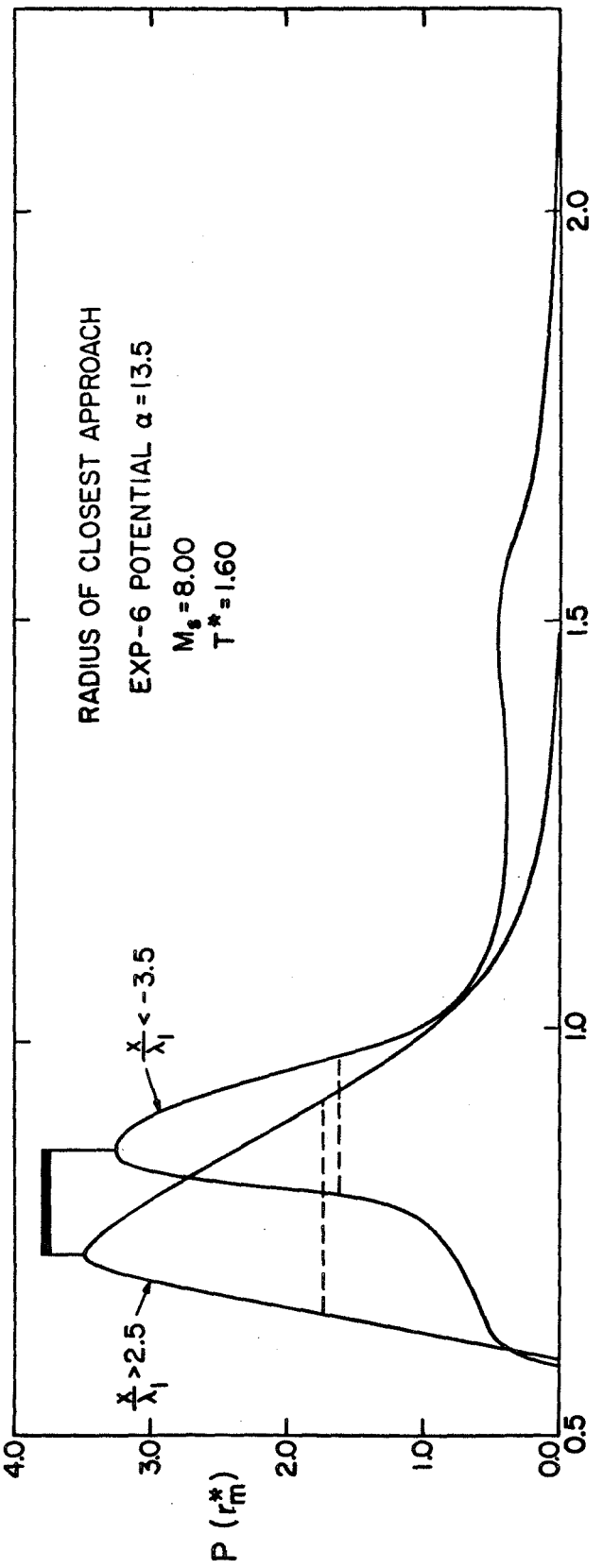

Figure 26. Monte Carlo Calculation Closest Approach Histogram

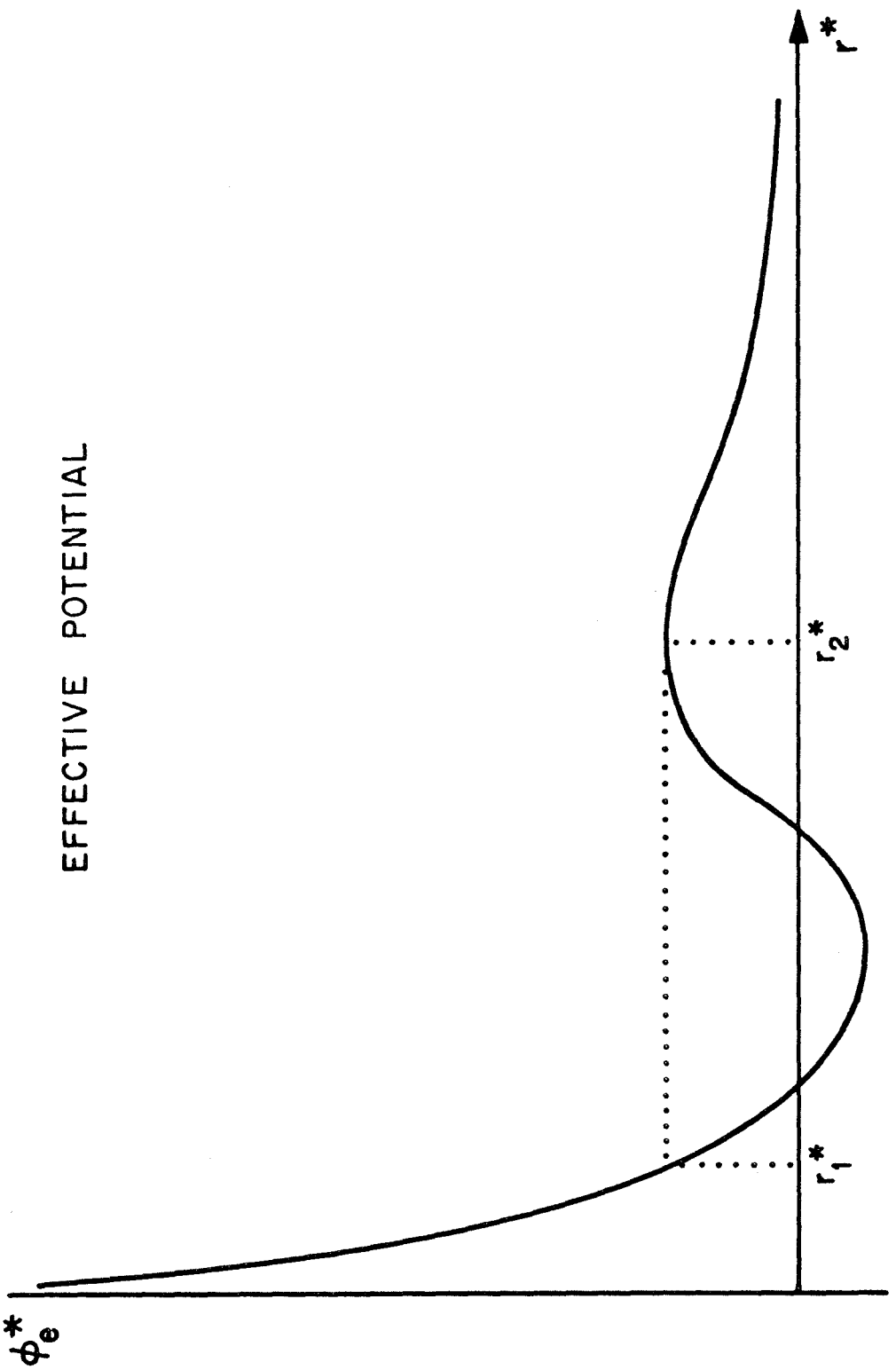

Figure 27. Effective Potential, ϕ_e^*, vs. r^*.

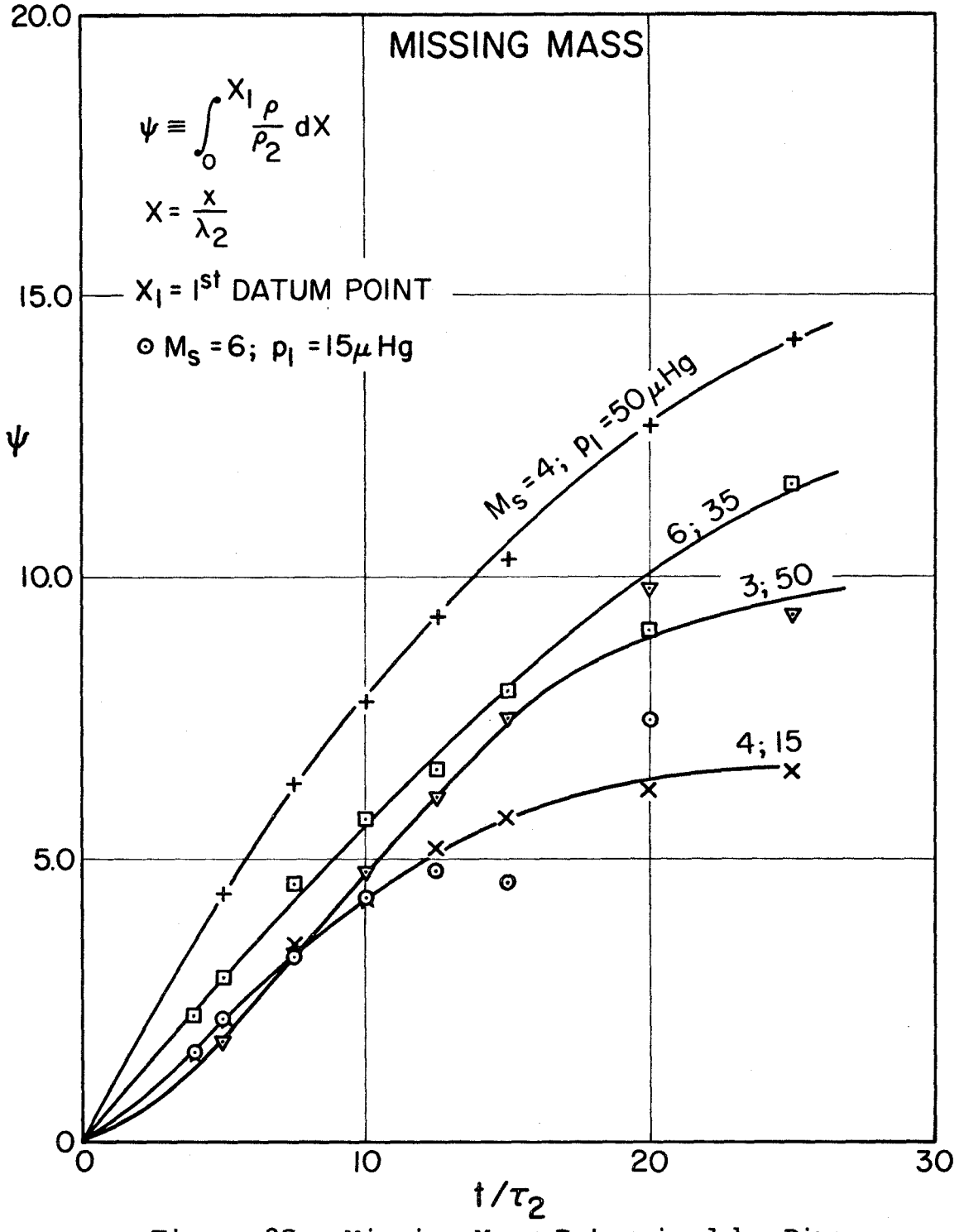

Figure 28. Missing Mass Determined by Piva

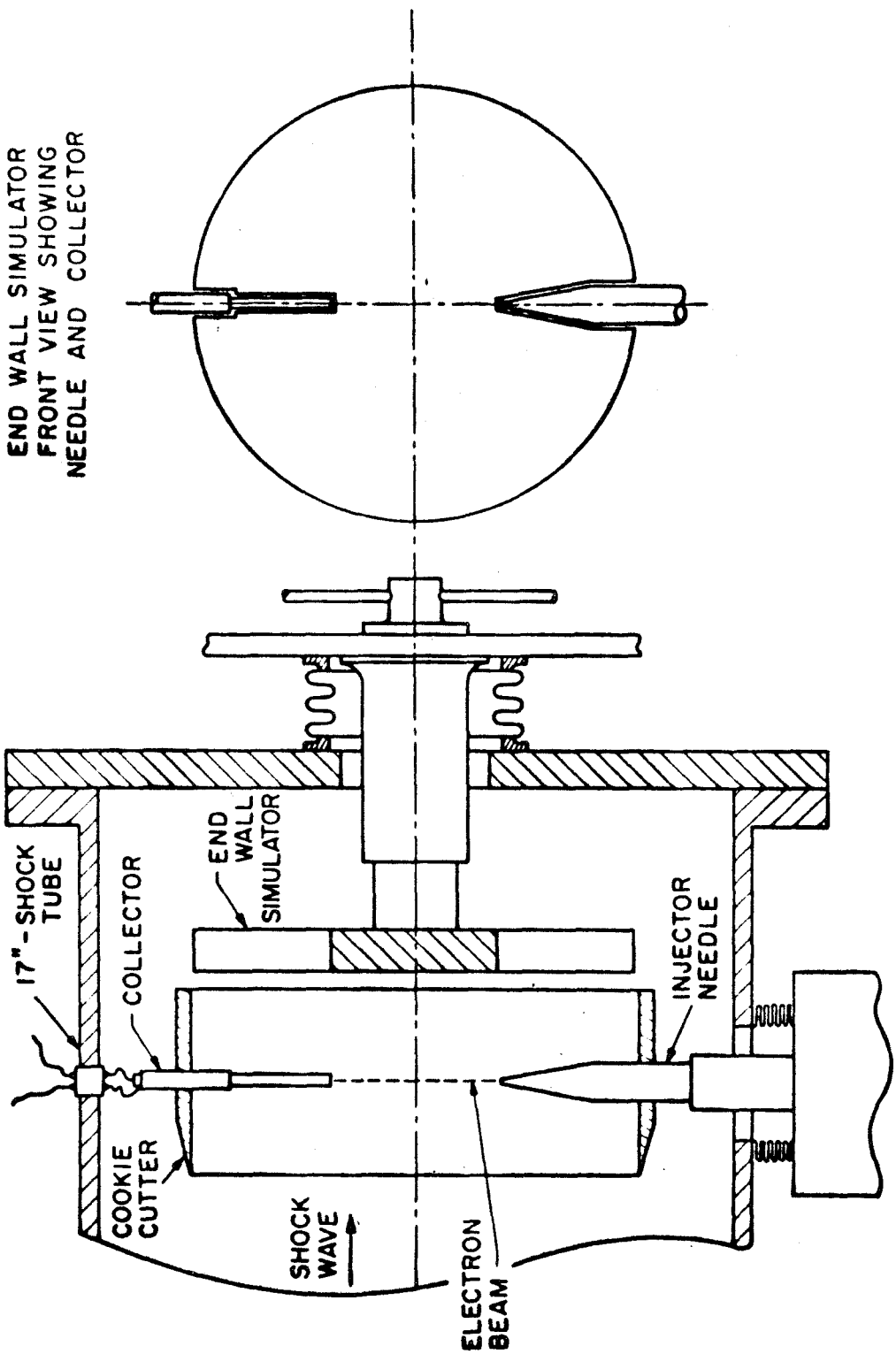

Figure 29. Electron Beam Densitometer and Moveable End Wall

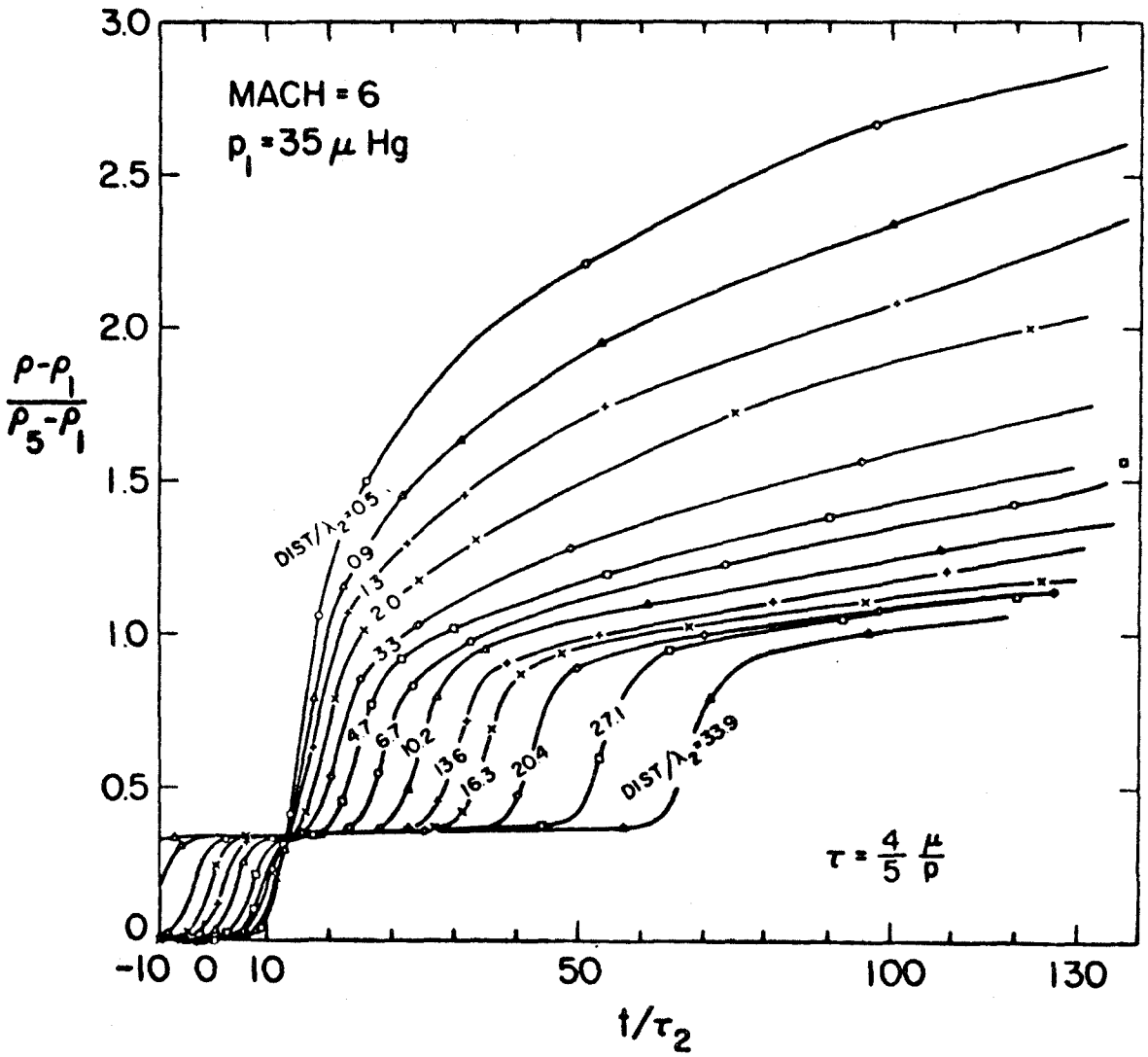

Figure 30. Density vs. Time Measured at Fixed Distances from the End Wall

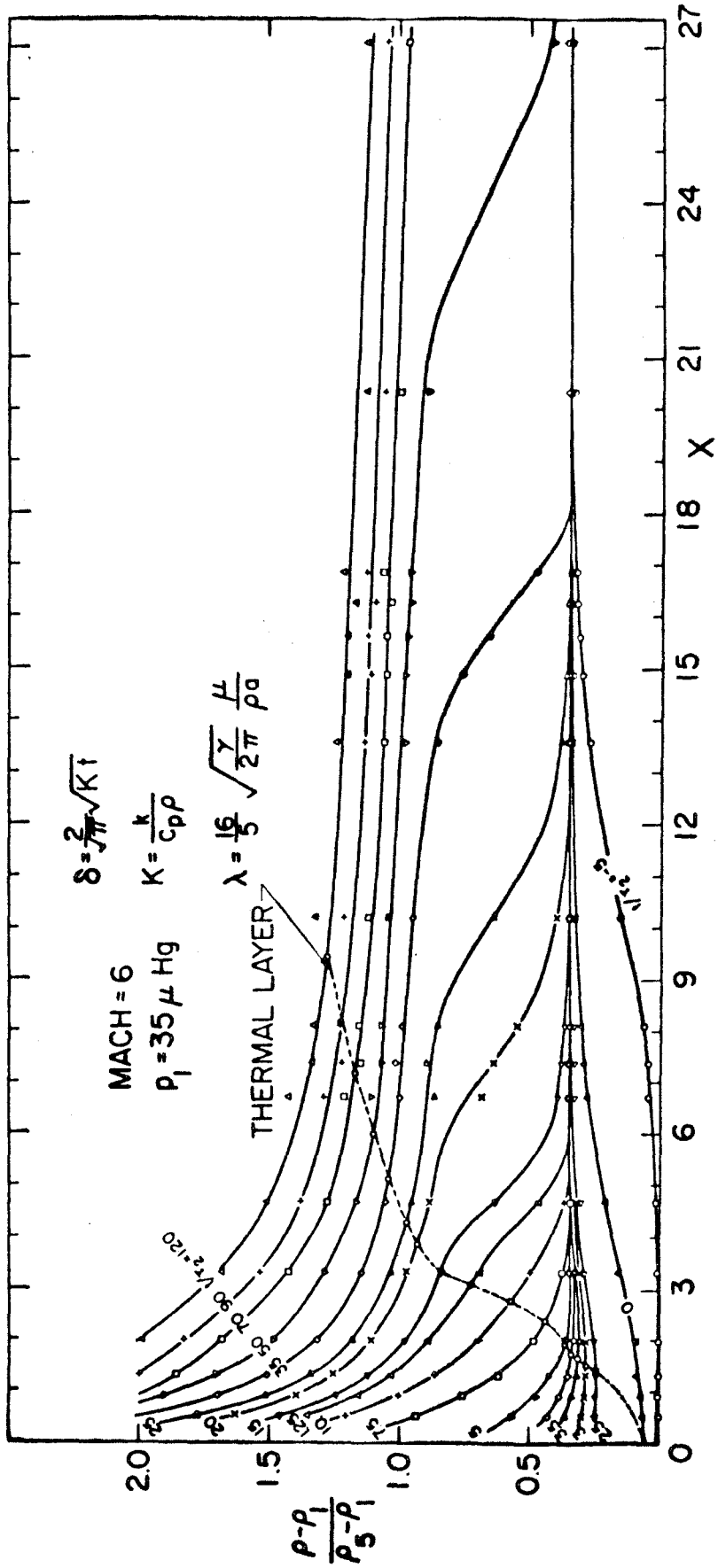

Figure 31. Density vs. Distance from the Wall for a Shock Reflecting in Argon

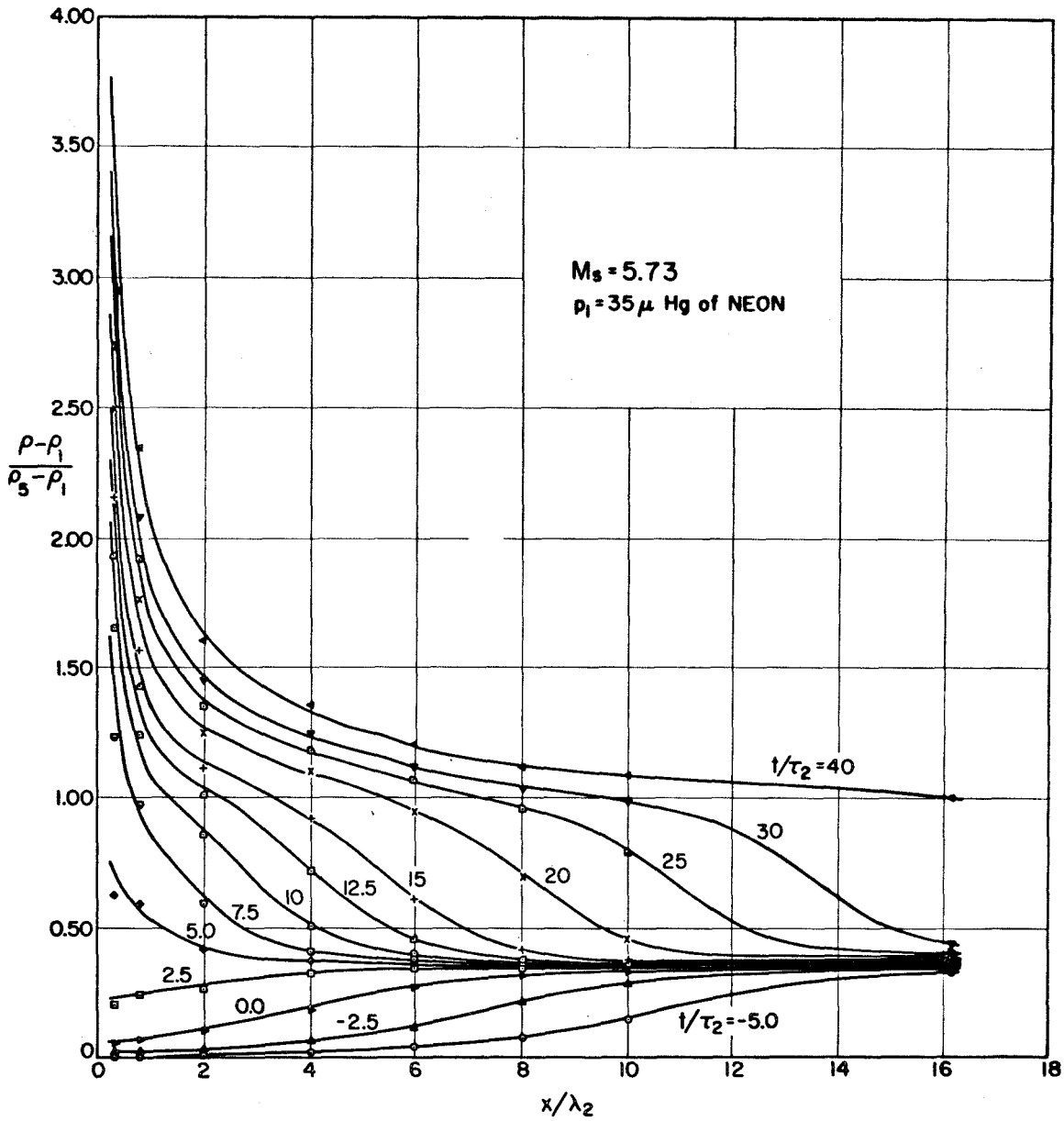

Figure 32. Density vs. Distance from the Wall for a Shock Reflecting in Neon

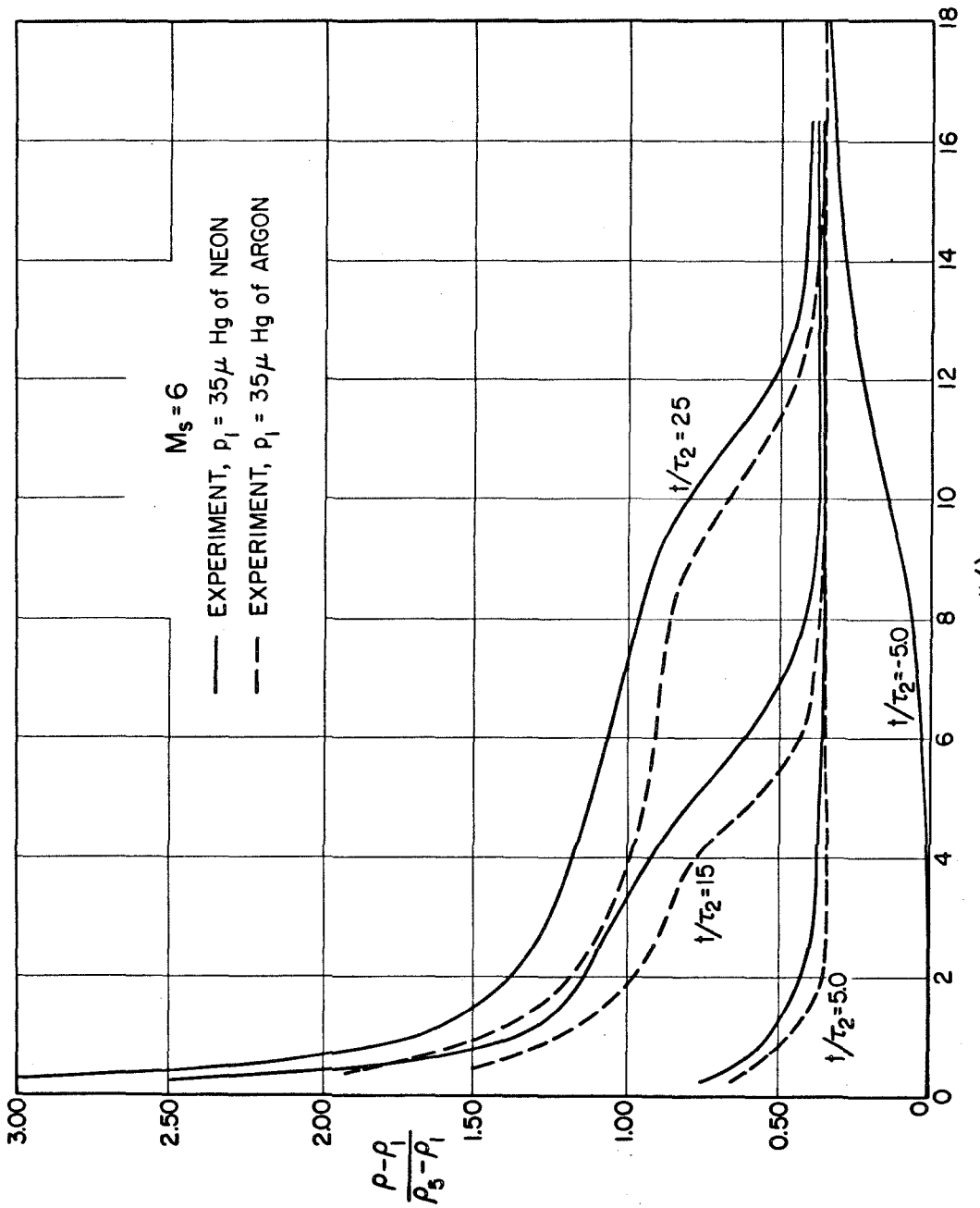

Figure 33. Comparison of Density Profiles for Shocks Reflecting in Argon and Neon

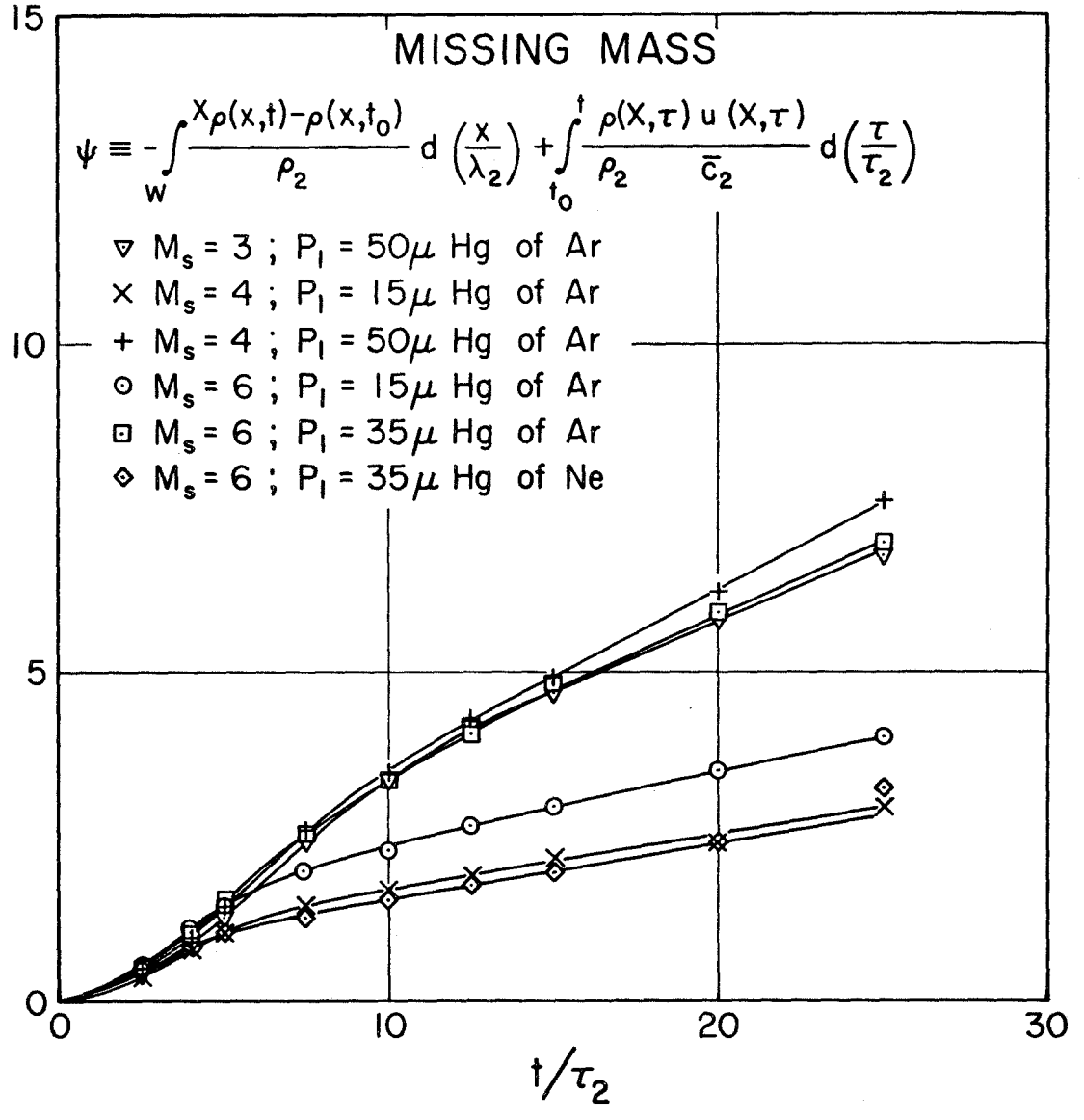

Figure 34. Improved Mass Balance (Missing Mass)

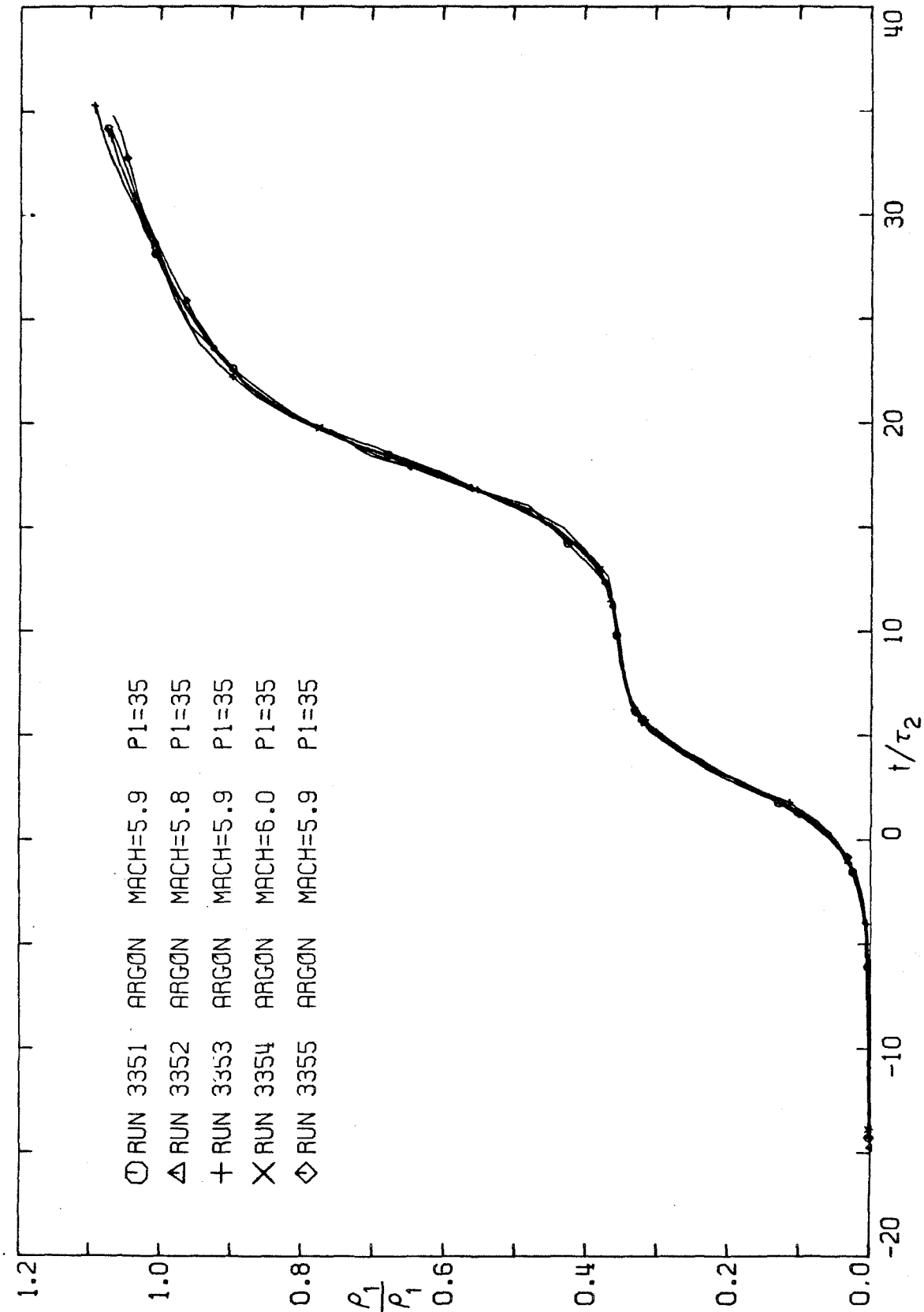

Figure 35. Density vs. Time Measured at 3.5 mm. from the End Wall

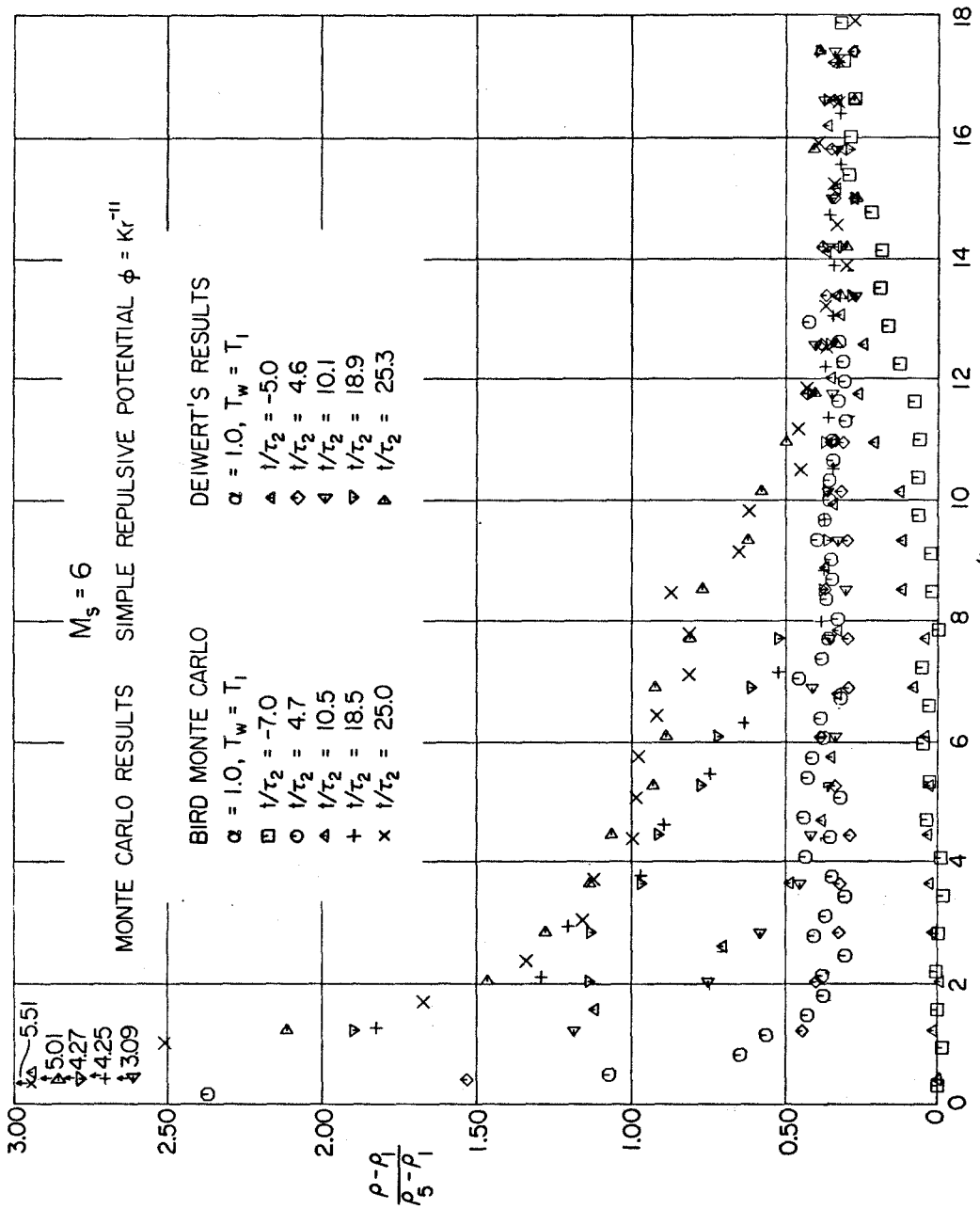

Figure 36. Comparison of Bird Monte Carlo Method with Deiwert's Monte Carlo Results at $\alpha = 1.0$

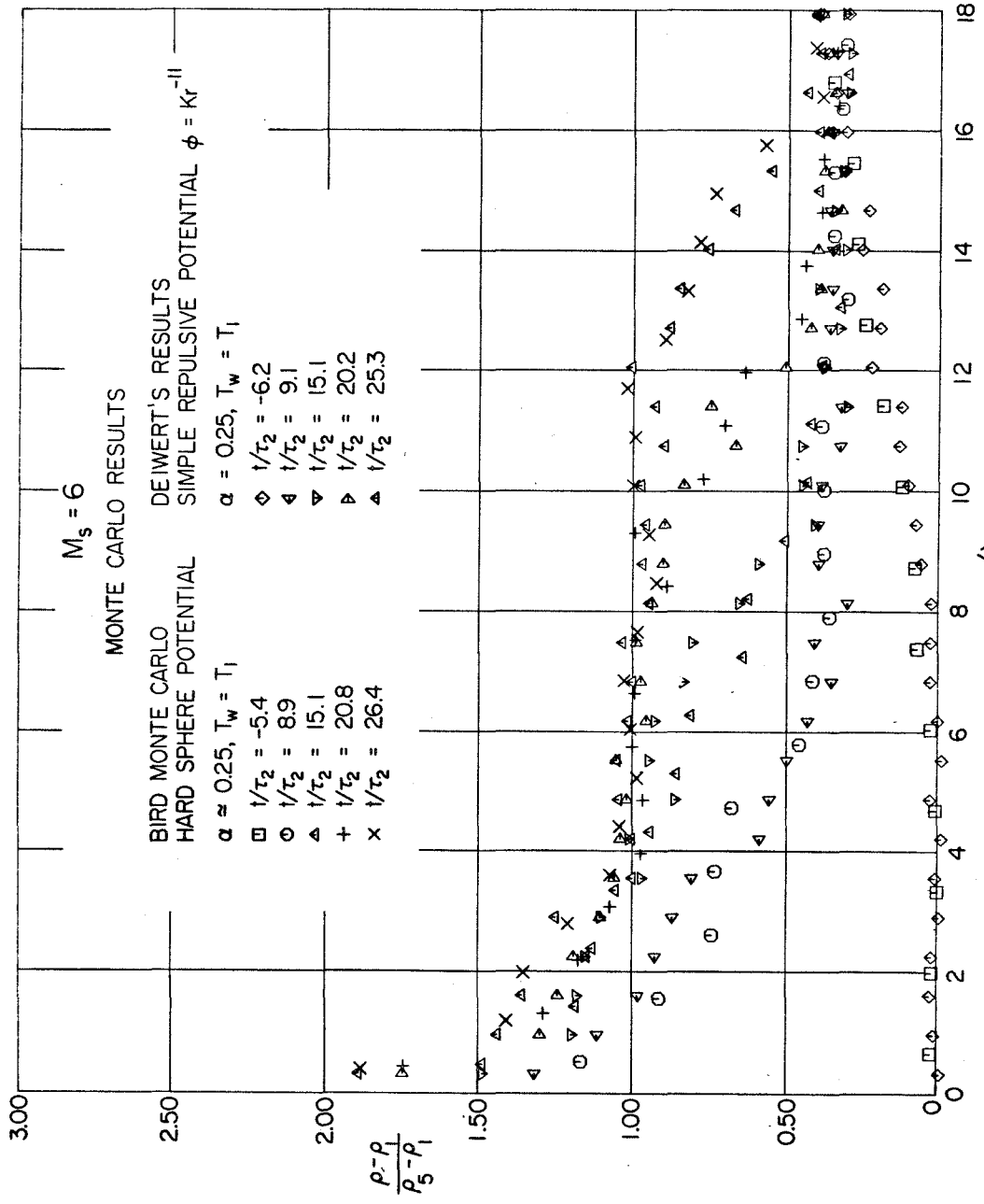

Figure 37. Comparison of Bird Monte Carlo Method with Deiwert's Monte Carlo Results at $\alpha = 0.25$

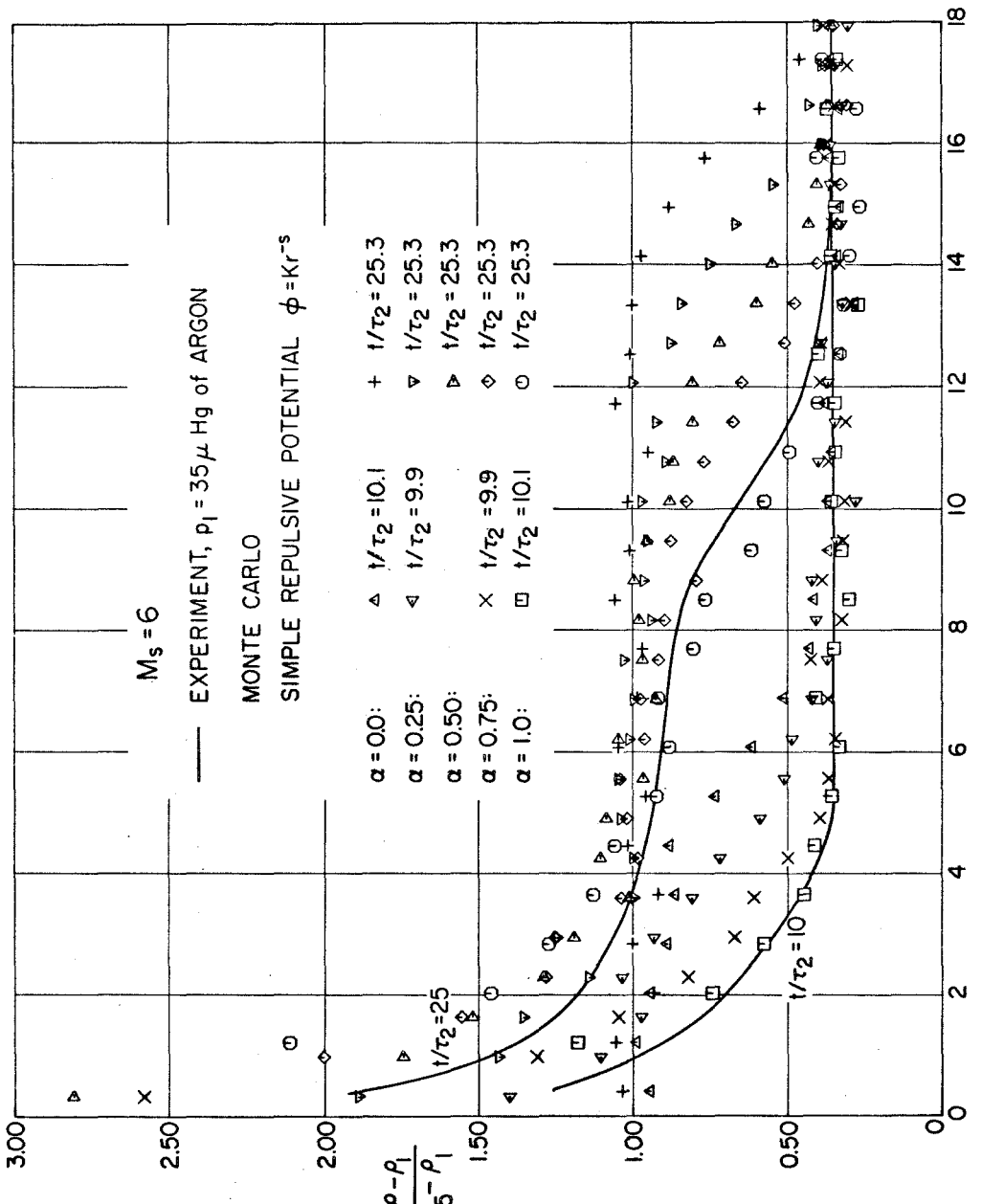

Figure 38. Deiwert's Monte Carlo Results for Different Amounts of Thermal Accommodation

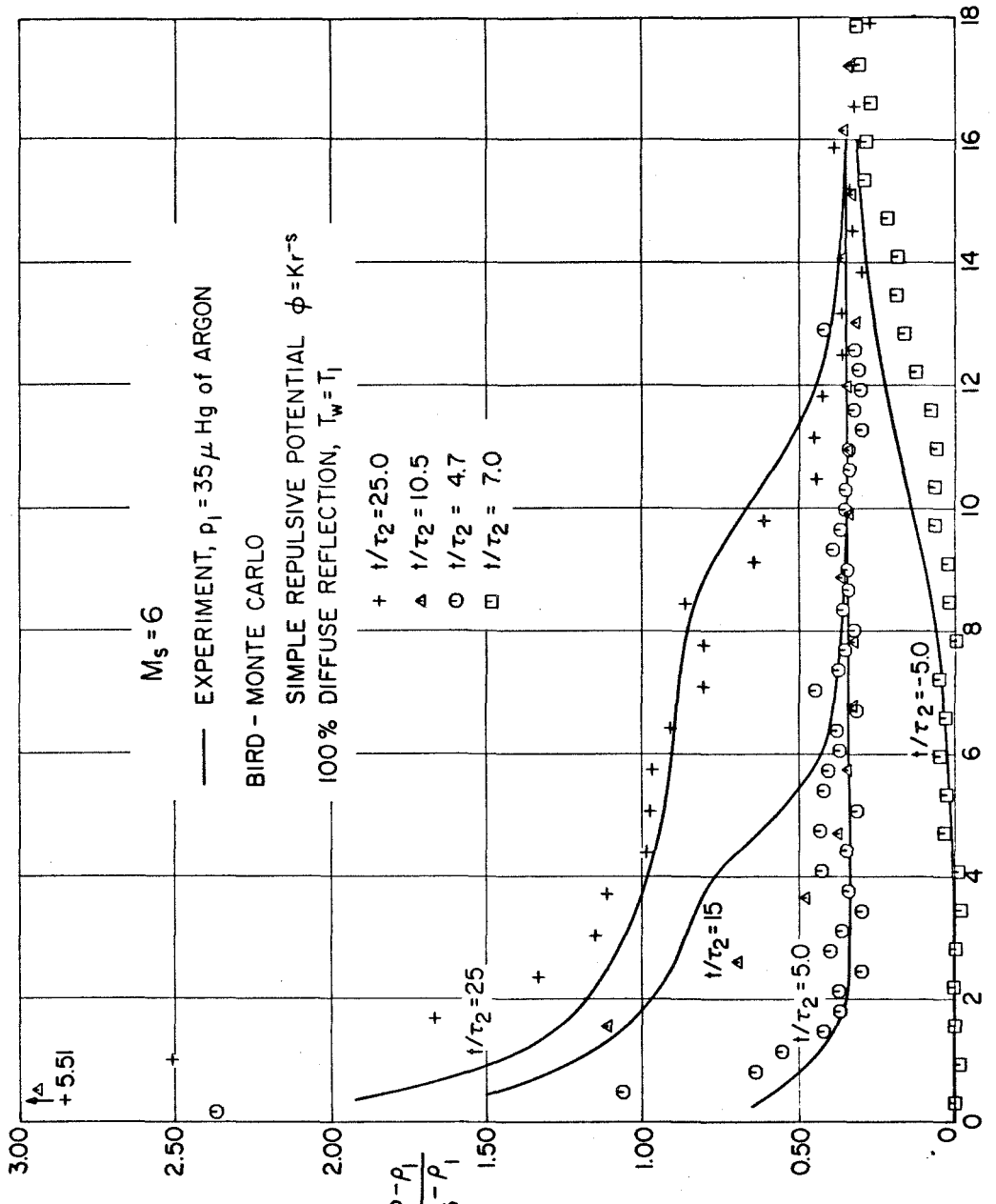

Figure 39. Comparison of Bird Monte Carlo Method with Experimental Density Profiles in Argon

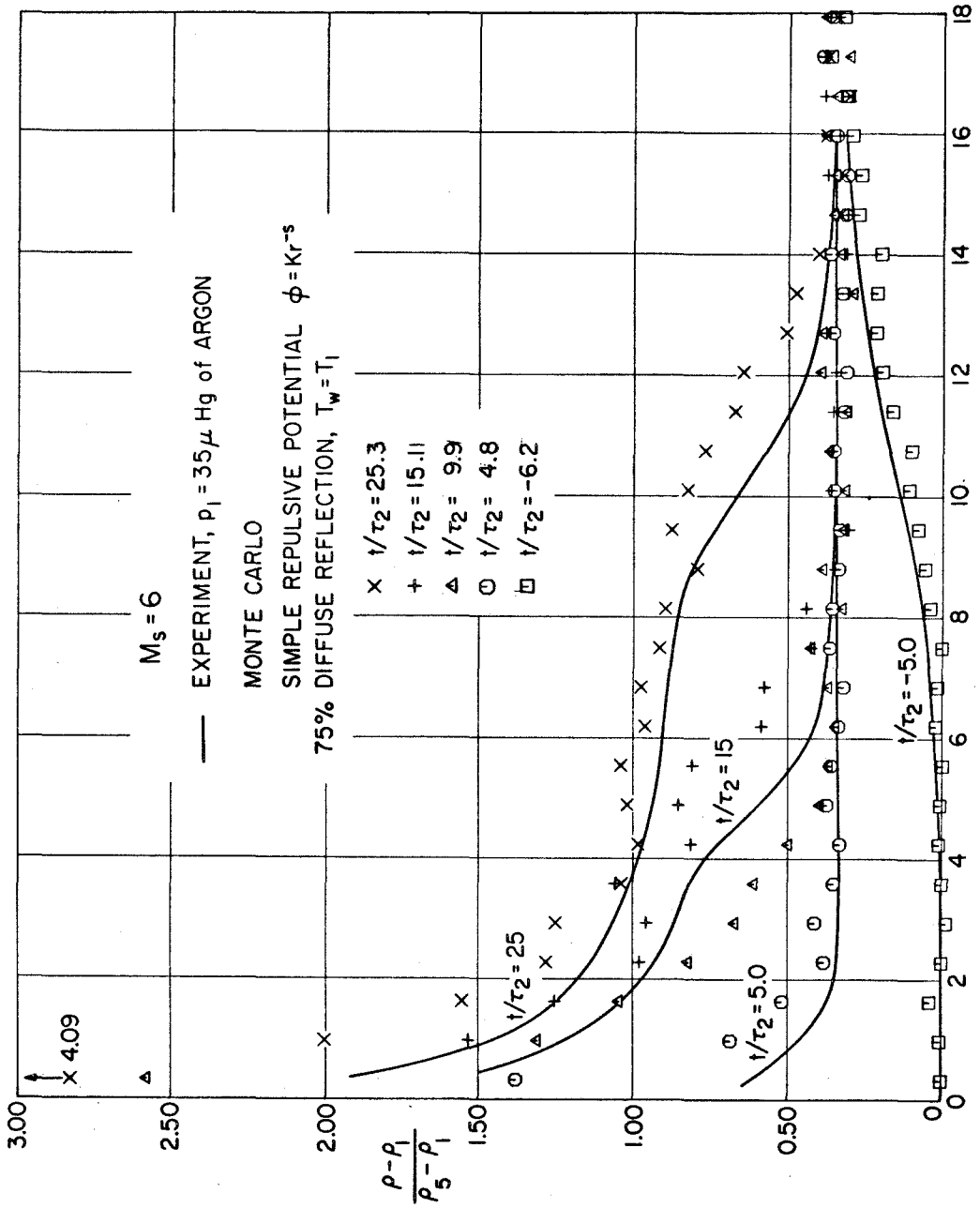

Figure 40. Comparison of Deiwert's Monte Carlo Results with Experimental Density Profiles in Argon

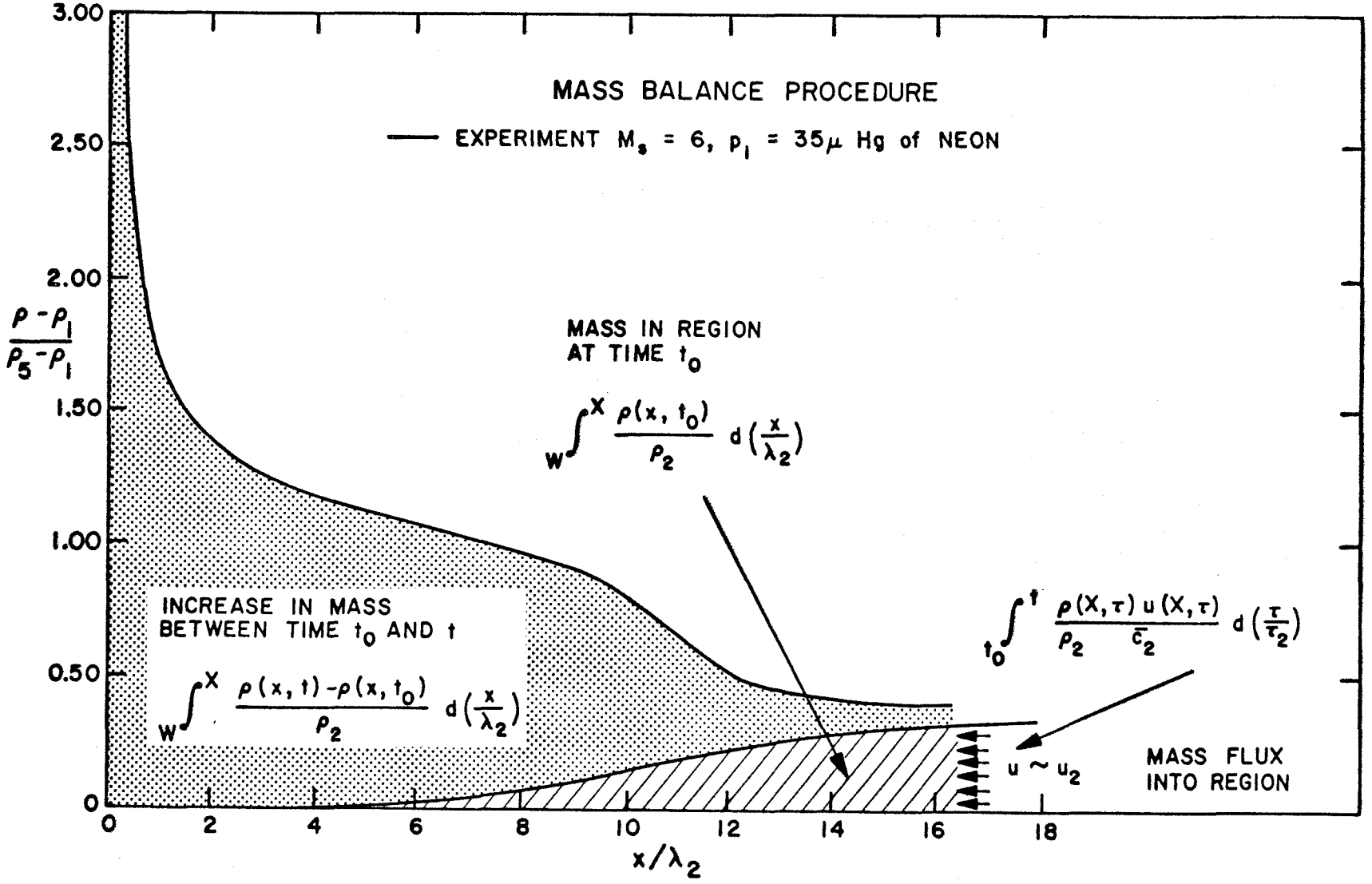

Figure 41. Mass Balance Calculation of Equation 2.4-3

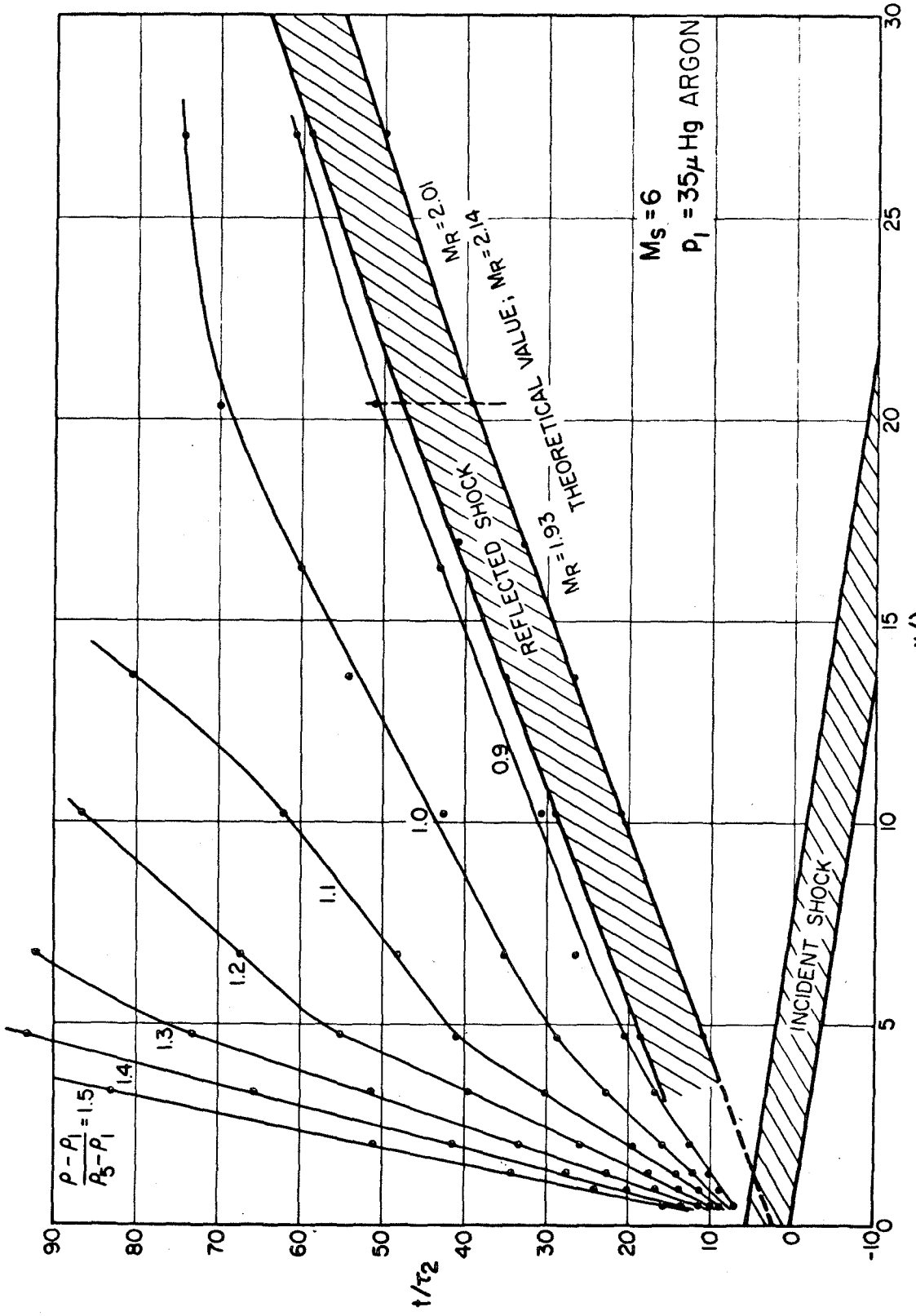

Figure 42. An x-t Diagram of Density as a Shock Wave Reflects

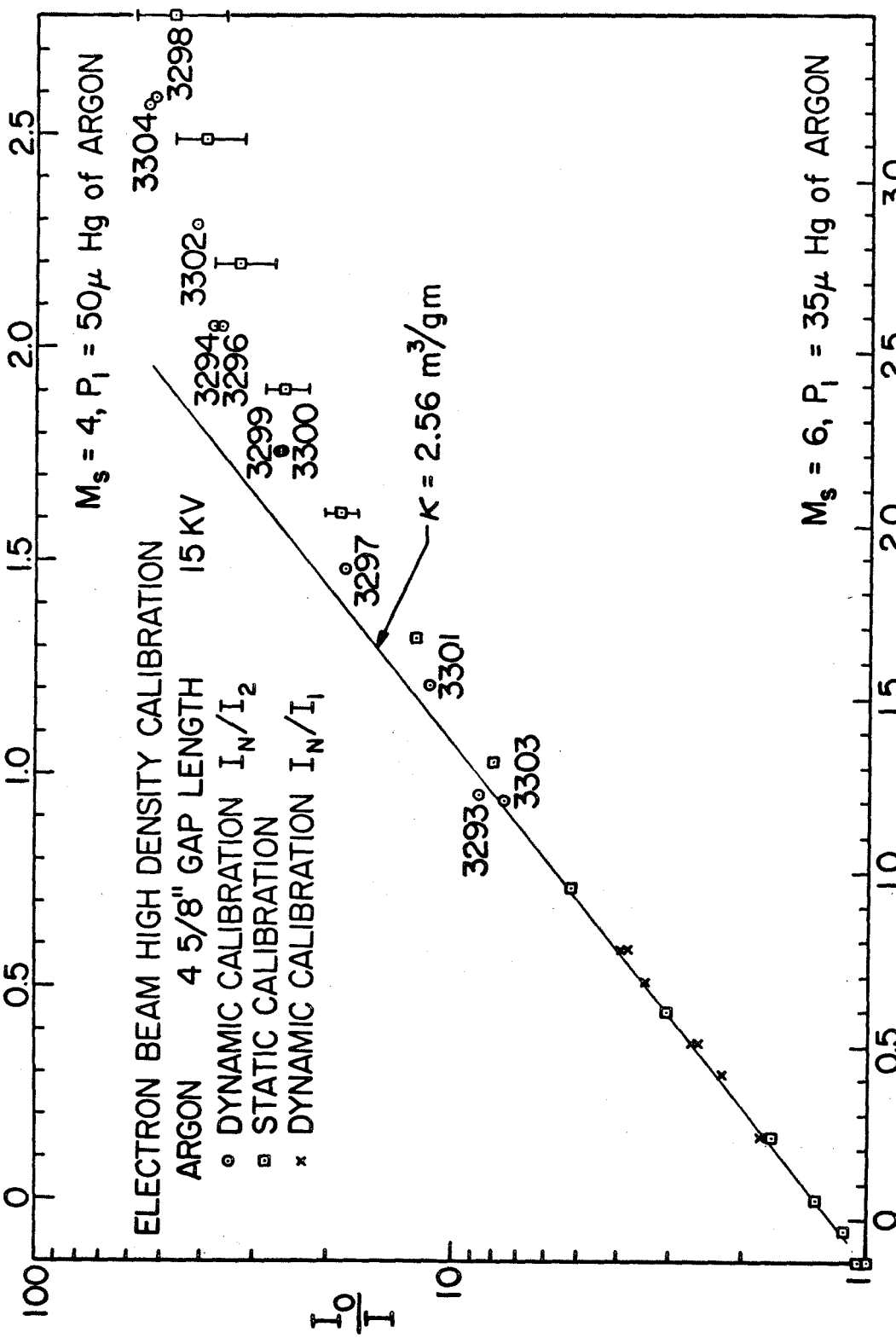

Figure 43. High Density Calibration Far from the End Wall

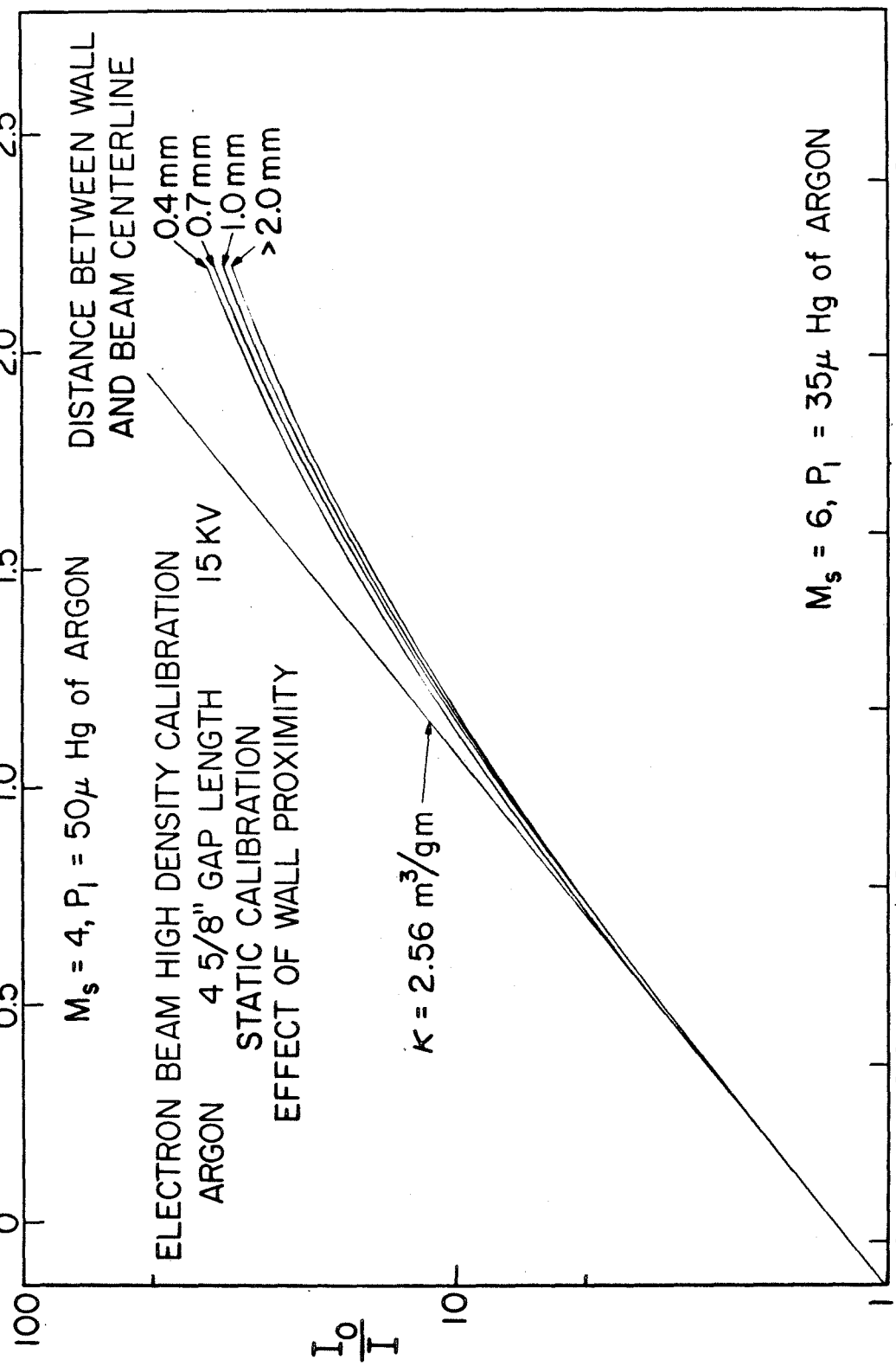

Figure 44. High Density Calibration Close to the End Wall

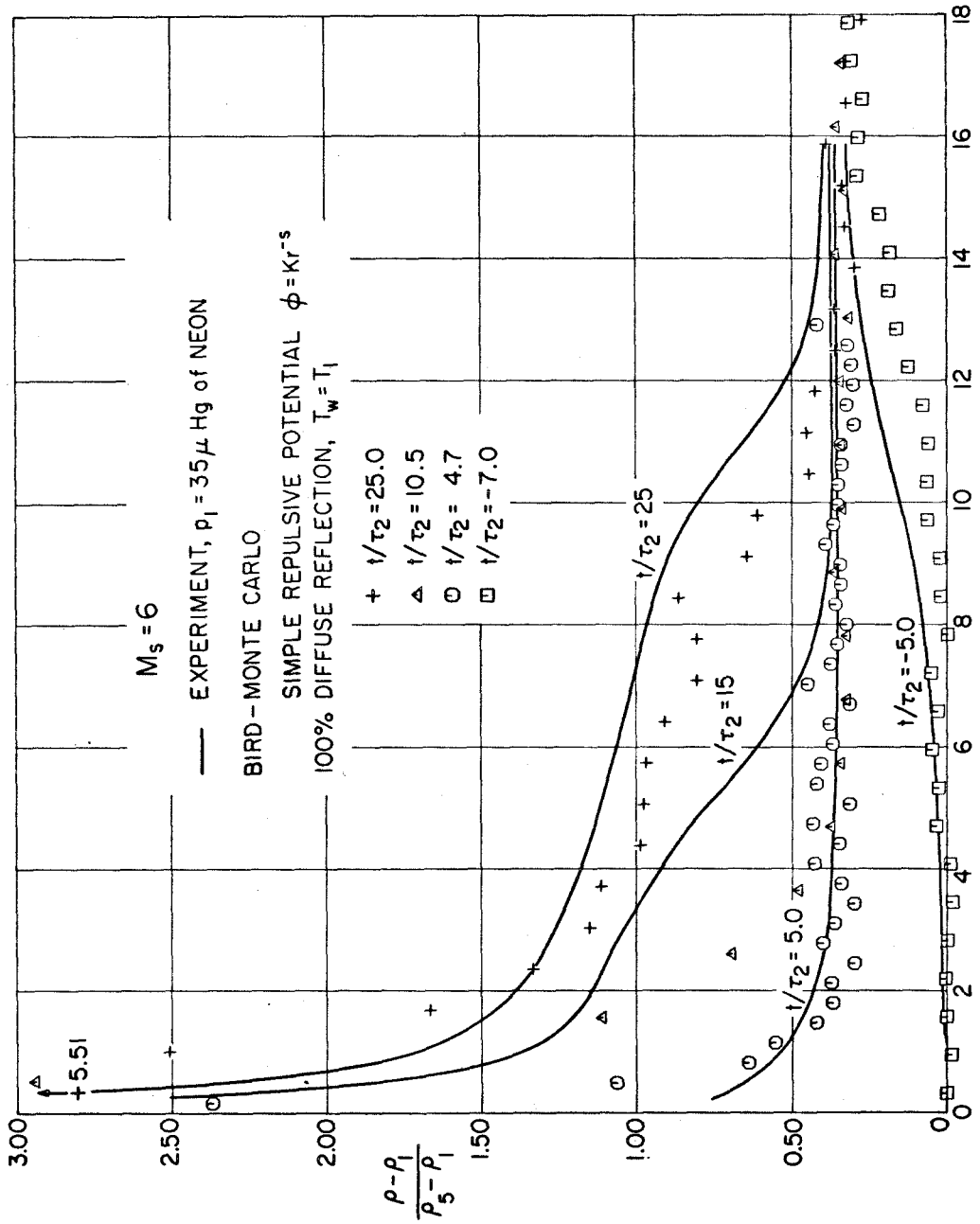

Figure 45. Comparison of Bird Monte Carlo Method with Experimental Density Profiles in Neon

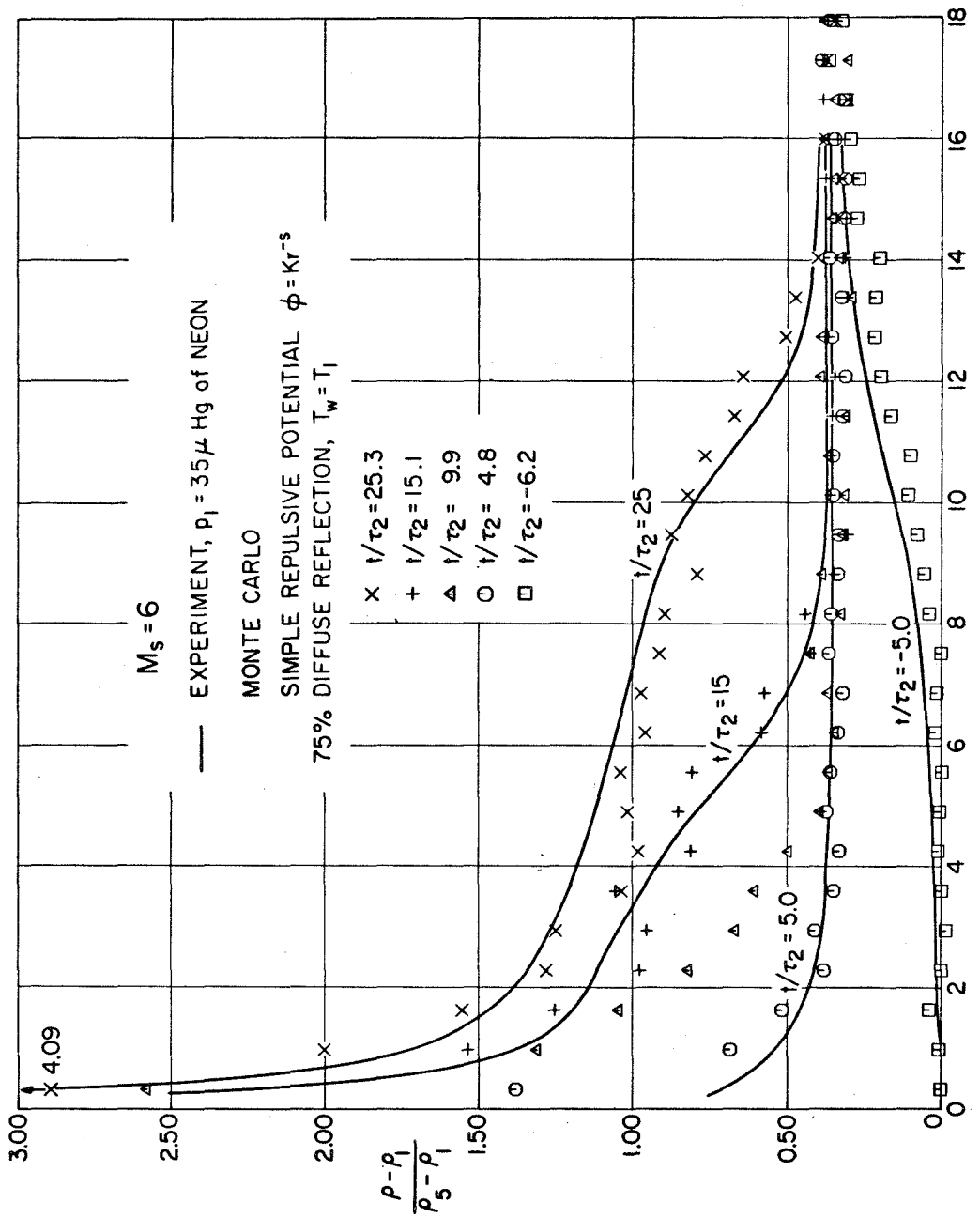

Figure 46. Comparison of Deiwert's Monte Carlo Results with Experimental Density Profiles in Neon

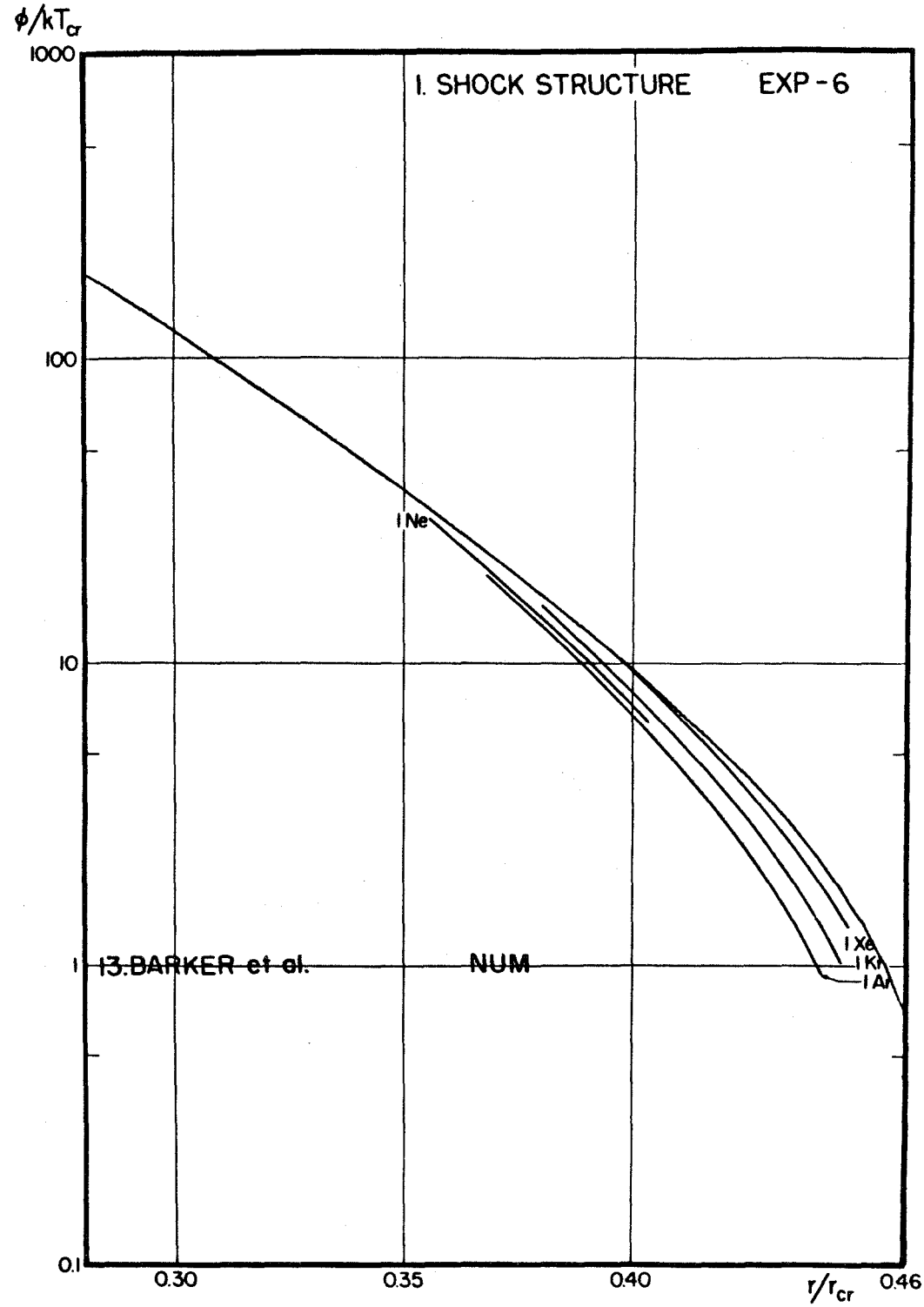

Figure 47. Corresponding States Plot of Potentials Obtained from Several Properties.[50]